

THEORY OF GAP SYMMETRY AND STRUCTURE IN FE-BASED  
SUPERCONDUCTORS

By

YAN WANG

A DISSERTATION PRESENTED TO THE GRADUATE SCHOOL  
OF THE UNIVERSITY OF FLORIDA IN PARTIAL FULFILLMENT  
OF THE REQUIREMENTS FOR THE DEGREE OF  
DOCTOR OF PHILOSOPHY

UNIVERSITY OF FLORIDA

2014

© 2014 Yan Wang

To my parents

## ACKNOWLEDGMENTS

I would like to express my greatest thanks to my adviser Prof. Peter J. Hirschfeld for his mentoring and support in my doctoral study. He has guided me closely at every stage of my research through countless inspiring and patient discussions, and provided enormous suggestions and encouragements as a mentor and a friend. I would like further to thank Drs. Tom Berlijn, Siegfried Graser, Andreas Kreisel, Chia-Hui Lin, Thomas Maier, Vivek Mishra, Douglas Scalapino, Gregory Stewart, Ilya Vekhter and Limin Wang for valuable discussions and dedicated collaborations in various projects. I'm also grateful to my committee members Drs. Kevin Ingersent, Dmitrii Maslov, David Tanner, Simon Phillpot and Gregory Stewart for their time and expertise devoted to scrutinizing my dissertation.

I acknowledge the hospitality of Dr. Wei Ku at Brookhaven National Laboratory, Dr. Thomas Maier at Oak Ridge National Laboratory and Dr. Roser Valenti at Goethe University Frankfurt for inviting me to their laboratories or university.

I acknowledge the partial financial support from Institute for Fundamental Theory at University of Florida.

I am deeply thankful to my former and current group colleagues Maxim Korshunov, Greg Boyd, Lex Kemper, Peayush Choubey, and Wen-Ya Rowe, to my fellow graduate students Pan Zheng, Jue Zhang, Iek-Heng Chu, Xiangguo Li, Lili Deng and Xiaochang Miao, and to Physics Department staff for their professional assistance.

Finally I would like to thank my parents for their unconditional support, understanding and love that cheer me up anytime and anywhere.

# TABLE OF CONTENTS

|   | <u>page</u> |
|---|-------------|
| ACKNOWLEDGMENTS . . . . .   | 4           |
| LIST OF TABLES . . . . .  | 7           |
| LIST OF FIGURES . . . . .   | 8           |
| ABSTRACT . . . . .  | 10          |
| CHAPTER   |             |
| 1 INTRODUCTION . . . . .  | 13          |
| 1.1 The Chronicle of Superconductivity: Early History . . . . .   | 14          |
| 1.2 The Chronicle of Superconductivity: After BCS . . . . .   | 18          |
| 1.3 The Symmetry Properties of Fe-Based Superconductors . . . . .   | 25          |
| 1.3.1 Crystal Structure and Crystal Symmetry . . . . .  | 25          |
| 1.3.2 Gap Symmetry and Gap Structure . . . . .  | 26          |
| 2 INHOMOGENEOUS SUPERCONDUCTIVITY . . . . .   | 29          |
| 2.1 Quasiclassical Approximation . . . . .  | 30          |
| 2.2 Volovik Effect in Multiband Superconductor $\text{BaFe}_2(\text{As}_{0.7}\text{P}_{0.3})_2$ . . . . . | 34          |
| 2.2.1 Motivation . . . . .  | 34          |
| 2.2.2 Experiment Results . . . . .  | 36          |
| 2.2.3 Two-Band Model . . . . .  | 38          |
| 2.2.4 Results . . . . .   | 43          |
| 2.2.5 Conclusions . . . . .   | 47          |
| 2.3 Quasiparticle Vortex Bound States in FeBS: Application to LiFeAs . . . . .                            | 49          |
| 2.3.1 Motivation . . . . .  | 49          |
| 2.3.2 Model . . . . .   | 54          |
| 2.3.3 Results . . . . .   | 56          |
| 2.3.4 Conclusions . . . . .   | 59          |
| 3 DISORDER IN SUPERCONDUCTORS . . . . .   | 61          |
| 3.1 Motivation . . . . .  | 61          |
| 3.2 Model . . . . .   | 63          |
| 3.3 $T_c$ Suppression . . . . .   | 65          |
| 3.4 Residual Resistivity . . . . .  | 66          |
| 3.5 Results . . . . .   | 66          |
| 3.5.1 $T_c$ Suppression vs Resistivity . . . . .  | 66          |
| 3.5.2 Density of States . . . . .   | 70          |
| 3.5.3 Nonmonotonic Dependence of Residual DOS on Disorder . . . . .                                       | 71          |
| 3.5.4 Realistic Impurity Potentials . . . . .   | 73          |
| 3.6 Conclusions . . . . .   | 73          |

|                               |   |     |
|-------------------------------|---|-----|
| 4                             | SPIN-FLUCTUATION PAIRING IN FE-BASED SUPERCONDUCTORS . . . . .              | 75  |
| 4.1                           | Motivation . . . . .  | 75  |
| 4.2                           | Ten-Orbital Tight-Binding Fits and Fermi Surfaces . . . . .                 | 78  |
| 4.3                           | Fluctuation Exchange Pairing Model . . . . .                                | 80  |
| 4.4                           | Results for the Pairing State . . . . .                                     | 83  |
| 4.4.1                         | Results for the ARPES-Derived Fermi Surface . . . . .                       | 83  |
| 4.4.2                         | Analysis of Gap Sizes in Terms of Pairing Vertex . . . . .                  | 85  |
| 4.4.3                         | Discussion: Toy Model for Gap Sizes . . . . .                               | 89  |
| 4.5                           | Conclusions . . . . .   | 90  |
| 5                             | FINAL CONCLUSIONS . . . . .   | 99  |
| APPENDIX                      |   |     |
| A                             | SPIN-FLUCTUATION CALCULATION FOR DFT-DERIVED FERMI SURFACE .                | 102 |
| A.1                           | Electronic Structure of LiFeAs from Density Functional Theory . . . . .     | 102 |
| A.2                           | Pairing State for DFT-Derived Fermi Surface . . . . .                       | 102 |
| B                             | FITTING PARAMETERS FOR TEN-ORBITAL TIGHT-BINDING MODEL $H_0^{\text{ARPES}}$ | 106 |
| REFERENCES . . . . .          |   | 111 |
| BIOGRAPHICAL SKETCH . . . . . |   | 120 |

## LIST OF TABLES

| <u>Table</u>  | <u>page</u> |
|---|-------------|
| 1-1 Irreducible representations and gap functions for tetragonal symmetry . . . . . | 28          |
| 2-1 Different models for the coupling matrix and gap anisotropy on electron pockets | 44          |
| A-1 LiFeAs DOS at the Fermi level from ten-orbital DFT and ARPES based models       | 103         |

## LIST OF FIGURES

| <u>Figure</u>   | <u>page</u> |
|---|-------------|
| 1-1 Meissner effect demonstration . . . . .   | 15          |
| 1-2 Critical field and magnetization of type I and type II superconductors . . . . .                                    | 16          |
| 1-3 Schematic phase diagrams and active layers of cuprates and FeBS . . . . .   | 21          |
| 1-4 Fermi surface of FeBS . . . . .   | 25          |
| 1-5 Crystal structures of FeBS . . . . .  | 27          |
| 2-1 Specific heat coefficient $\gamma$ vs high field $H$ on $\text{BaFe}_2(\text{As}_{0.7}\text{P}_{0.3})_2$ . . . . .  | 37          |
| 2-2 Specific heat coefficient $\gamma$ vs low field $H$ on $\text{BaFe}_2(\text{As}_{0.7}\text{P}_{0.3})_2$ . . . . .   | 38          |
| 2-3 Spatially averaged ZDOS for nodeless and nodal superconductors . . . . .  | 40          |
| 2-4 Gap field dependence and spatially averaged ZDOS . . . . .  | 43          |
| 2-5 Measured normalized specific heat coefficient and the two-band calculations . . . . .                               | 45          |
| 2-6 Specific heat coefficient from gaps with deep minima and accidental nodes . . . . .                                 | 48          |
| 2-7 Conductance map and ZDOS around a vortex core for a $d_{x^2-y^2}$ -wave gap . . . . .                               | 51          |
| 2-8 Fermi surface of LiFeAs at $k_z = 0$ and the Fermi velocities . . . . .   | 52          |
| 2-9 Sketch of ARPES measured gaps and STS conductance map of LiFeAs . . . . .   | 54          |
| 2-10 ZDOS for different models with circular Fermi surface or LiFeAs $\gamma$ pocket . . . . .                          | 57          |
| 2-11 LDOS $N(\mathbf{r}, \omega)/N_0$ vs energy $\omega$ for different gap models and Fermi surfaces . . . . .          | 60          |
| 3-1 Sketch of the two-band model with constant impurity scattering . . . . .  | 63          |
| 3-2 $T_c/T_{c0}$ vs disorder-induced resistivity change $\Delta\rho_0$ for isotropic $s_{\pm}$ -wave pairing . . . . .  | 68          |
| 3-3 $T_c/T_{c0}$ vs $\Delta\rho_0$ for various values of the inter- to intraband scattering ratio $\alpha$ . . . . .    | 70          |
| 3-4 The resistivity at half suppression $\Delta\rho_{1/2}$ as a function of the ratio $\alpha = u/v$ . . . . .          | 71          |
| 3-5 Schematic evolution of gaps and DOS with increasing disorder; DOS vs $\Delta\rho_0$ . . . . .                       | 72          |
| 4-1 Comparison of the tight-binding bands and ARPES data . . . . .  | 92          |
| 4-2 Sketch of the gap $ \Delta(\theta) $ as seen in recent ARPES experiments . . . . .                                  | 93          |
| 4-3 Fermi surface of LiFeAs from $H_0^{\text{ARPES}}$ , gap functions $g(\mathbf{k})$ and spin susceptibility . . . . . | 95          |
| 4-4 Band structures for ARPES-derived model with and without spin-orbit coupling . . . . .                              | 96          |

|     |   |     |
|-----|---|-----|
| 4-5 | Comparison between gap $ \Delta(\theta) $ by calculation and ARPES experiment . . . .                             | 97  |
| 4-6 | Components of pairing vertex $\Gamma_{ij}(\mathbf{k}, \mathbf{k}')$ matrix at filling $n = 6.00$ and $n = 5.90$ . | 98  |
| A-1 | Fermi surface of LiFeAs from $H_0^{\text{DFT}}$ , gap functions $g(\mathbf{k})$ and spin susceptibility .         | 105 |

Abstract of Dissertation Presented to the Graduate School  
of the University of Florida in Partial Fulfillment of the  
Requirements for the Degree of Doctor of Philosophy

THEORY OF GAP SYMMETRY AND STRUCTURE IN FE-BASED  
SUPERCONDUCTORS

By

Yan Wang

May 2014

Chair: Peter J. Hirschfeld

Major: Physics

We consider a series of problems related to determining the origin of superconductivity in the recently discovered iron pnictide and chalcogenide materials, where the common layer in the crystal structure with Fe atom at the square lattice site and with pnictogen or chalcogen atoms buckling above or below is believed to be responsible for the high  $T_c$ . In many experiments, these Fe-based superconductors also share similar physical properties such as multiple superconducting gaps exhibiting nontrivial structure with anisotropy and nodes that evolve with doping, a generic phase diagram with antiferromagnetic metal phase at zero doping, and the superconducting dome (or domes) with electron or hole doping or with pressure. A sign-changing “ $s_{\pm}$ ” superconducting state (that is, in an oversimplified term, two order parameters with the opposite sign) is proposed based on the electronic structure, Fermi surface and magnetic properties as measured by experiments and predicted by spin-fluctuation calculations.

In the first few chapters, we phenomenologically explain the experimental observations and their interpretations on the symmetry of pairing state and claim a consistency with  $s_{\pm}$  state after the subtle features of the superconducting state are considered in theory. We first discuss the Volovik effect in a highly anisotropic  $s_{\pm}$ -wave multiband superconductor, specifically the optimally doped  $\text{BaFe}_2(\text{As}_{1-x}\text{P}_x)_2$ . The square-root magnetic field dependence for the specific heat coefficient at a low field

(so-called Volovik effect) and the linear dependence at high field can be understood from a multiband calculation in the quasiclassical approximation assuming gaps with different momentum dependence on the hole- and electron-like Fermi surface sheets. Next, we examine the quasiparticle vortex bound states in LiFeAs. The “unexpected” (assuming an anisotropic  $s_{\pm}$ -wave pairing) tails of low energy density of states measured by scanning tunneling spectroscopy are reconciled by taking account of anisotropy of the Fermi surface and a cautionary message for the analysis of scanning tunneling spectroscopy data on the vortex state on Fe-based superconductors is sent to the experimentalists. In the next chapter, we have investigated the  $T_c$  suppression rate for  $s_{\pm}$  and  $s_{++}$  gap structure for Fe-based superconductors. The rate of  $T_c$  suppression is shown to vary dramatically according to details of the impurity model considered. A two-band model calculation with realistic parameters for  $\text{BaFe}_2\text{As}_2$  with nonmagnetic impurities suggests a probable  $s_{\pm}$ -wave state with small inter- to intra-band scattering rate ratio. We thus propose that observation of particular evolution of the penetration depth, nuclear magnetic resonance (NMR) relaxation rate, or thermal conductivity temperature dependence with disorder would suffice to differentiate  $s_{\pm}$  and  $s_{++}$  gap in experiments.

In the Chapter 4, we use the multiband Hubbard-Hund Hamiltonian generalized to microscopically investigate the symmetry of superconductivity in Fe-based superconductors (FeBS) by spin-fluctuation theory. The spin-fluctuation calculation of the superconducting instability is done for LiFeAs with three-dimensional Fermi surface. The pairing instabilities explored with full 10-orbital model suggest important three-dimensional effects that can be verified by experiments, such as angle-resolved photoemission spectroscopy (ARPES) and NMR. In the LiFeAs system, a comparison of density functional theory (DFT) derived model and ARPES derived model shows a strikingly good agreement between calculated results and principal ARPES measured gaps. We explain the only discrepancy of gaps on the small inner hole-like pockets.

Finally, we close with brief discussion on recent experiments and theoretical work on  $\text{AFe}_2\text{Se}_2$  and monolayer  $\text{FeSe}$ , two exciting families that challenge standard arguments in favor of the  $s_{\pm}$  pairing state with their unique electronic structure and magnetic properties.

## CHAPTER 1 INTRODUCTION

Nearly a decade ago I heard of *Woodstock of physics* in my Solid State Physics class. At that time I was deeply impressed and awed by the enthusiasm and excitement, as described by my professor, of those physicists attending the marathon session of the American Physics Society's March meeting in 1987, which featured presentations on then-newly discovered ceramic superconductors, now known as cuprates, from K. Alex Müller, Paul Chu, and many others. That K. Alex Müller and J. Georg Bednorz discovered 35 K superconductor lanthanum barium copper oxide  $[(\text{La}_{1-x}\text{Ba}_x)_2\text{CuO}_4$  or Ba-doped La214] in 1986 and later Paul Chu and colleagues discovered 93 K superconductor yttrium barium copper oxide ( $\text{YBa}_2\text{Cu}_3\text{O}_{7-\delta}$ , Y123 or YBCO) in 1987 was so earthshaking that about 2000 participants packed the aforementioned "Woodstock" session beginning at 7:30 PM and many of them didn't leave until 3:00 AM in the next morning. This discovery of cuprate system is one of the most notable milestones in the history of the superconductivity and probably the most dramatic one among others such as the discovery of superconductivity in 1911, the BCS theory in 1957, and the discovery of iron pnictide and chalcogenide superconductors in 2008. For physicists, the experimental and theoretical challenges of superconductivity since its discovery have been much more essential and motivating than the attention and popularity gradually gained in the general public or mass media. In this chapter, I will first briefly list the cornerstones of superconductivity, including the experimental discoveries of various superconductor classes and the prestigious BCS theory, next introduce the developments of BCS theory and new theories that account for unconventional and nontrivial superconductivity found in new classes of superconductors, and last focus on the basic experimental and theoretical aspects of iron pnictide and chalcogenide superconductors (Fe-based superconductors or FeBS), which

sets the stage for the remaining chapters. Recent historical reviews can be found in Refs. [1–3]; general reviews on FeBS can be found, for example, in Refs. [4–10].

### 1.1 The Chronicle of Superconductivity: Early History

In 1911, using the helium refrigeration technique he invented, Dutch physicist Heike Kamerlingh Onnes discovered in mercury (Hg,  $T_c = 4.2$  K) superconductivity, a phenomenon where the resistivity to the electrical current suddenly vanishes when the material is cooled below a critical temperature ( $T_c$ ). After having a close look at Kamerlingh-Onnes's lab notebooks, van Delft and Kes [11] pieced together the fascinating true story about the discovery of superconductivity, including the actual experiment procedures and the overlooked observation of superfluid transition (Bose-Einstein condensation) of helium ( $^4\text{He}$ ) at  $T_c = 2.2$  K.

In 1933, as the third research group who had managed to liquify helium in that time (J. C. McLennan from Toronto was the second in 1923), Walther Meissner and Robert Ochsenfeld from Berlin observed the diamagnetic behavior of superconductors, i.e., the complete expulsion of magnetic field from the superconductor [12]. Perfect diamagnetism and perfect conductivity are two hallmarks of a superconductor. However, perfect diamagnetism is not equivalent to perfect conductivity because if it were merely a material undergoing a perfect-conductivity transition, the magnetic flux originally inside the material would be trapped in due to Lenz's law as expected by classical electrodynamics. The reversible *Meissner effect* manifests that the superconductivity is a quantum effect on a macroscopic scale. If the external field is smaller than a temperature dependent critical value  $H_c(T)$ , the system can lower its free energy by going into the superconducting state at the cost of expelling the magnetic field from the bulk. Diamagnetism is suitable for magnetic levitation [13], and an often-seen demonstration of the diamagnetism of a superconductor is to levitate a permanent magnet by a superconductor, as shown in Fig. 1-1. In contrast to the “flying frog” [13] or the like, the demonstration with superconductor is easier to accomplish because the so



Figure 1-1. A piece of permanent magnet levitating above the superconductor cooled by liquid nitrogen, demonstrating the Meissner effect. Photo taken by the author at the M2S conference, 2012.

called type II superconductor (usually with higher  $T_c$ ) is used, where the magnetic flux lines help to stabilize the levitation and even make the suspension of a superconductor below a permanent magnet possible [14]. In type II superconductor, the quantized magnetic flux, with the fluxoid quantum  $\Phi_0 = \frac{hc}{2e}$ , penetrates the superconductor at temperature below  $T_c$  in a magnetic field range between the lower critical field  $H_{c1}$  and upper critical field  $H_{c2}$ , being in the so called *vortex state*. Below  $H_{c1}$ , the Meissner effect follows. Fig. 1-2 shows the comparison between type I and II superconductor.

In 1935, the brothers F. and H. London suggested a theory [15] to explain the Meissner effect, a phenomenological theory describing the electrodynamic properties of the superconductor. Following an unpublished theorem of Bloch (ground state should have zero net momentum without external field), they showed that the current density  $\mathbf{J} = n_s e \langle \mathbf{v}_s \rangle = -\frac{n_s e^2}{mc} \mathbf{A} = -(c/4\pi\lambda_L^2) \mathbf{A}$ , where  $\lambda_L = (mc^2/4\pi e^2 n_s)^{1/2}$  is the penetration depth of the magnetic field at  $T = 0$  and  $\mathbf{A}$  is the vector potential. The Coulomb gauge  $\text{div } \mathbf{A} = 0$  is usually imposed as the particular gauge choice. Later Pippard introduced the coherence length  $\xi$  and non-local generalization of London theory to account for the actual experimentally measured penetration depth [16].

In 1950, the *isotope effect*,  $T_c \propto 1/\sqrt{M}$  ( $M$  is ion mass), was seen in experiments by Serin [17] and Maxwell [18], indicating the essential role played by lattice vibrations

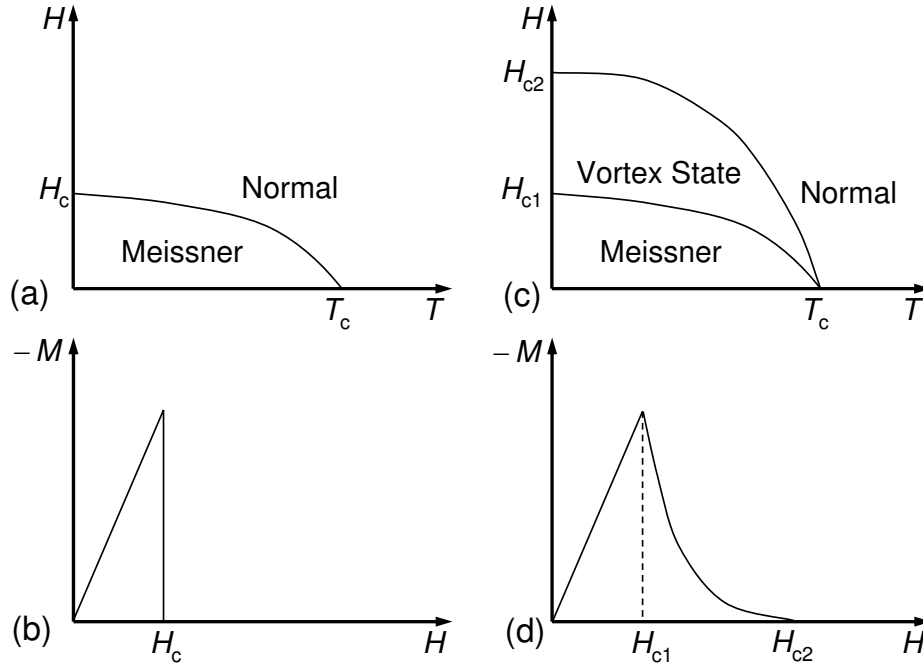


Figure 1-2. (a), (c) Critical field temperature dependence for type I (a) and type II (c) superconductor. (b), (d) Magnetization field dependence for type I (b) and type II (d) superconductor.

in superconductivity. In the same year, the Ginzburg–Landau theory based on Landau’s theory of second-order phase transitions further extended the London theory, where the order parameter  $\psi(\mathbf{x}, T)$  describing the superconducting transition was introduced [19].

The theoretical breakthrough in superconductivity came from Bardeen, Cooper and Schrieffer (BCS theory) in 1957 [20]. This elegant microscopic theory successfully explains the superconductivity in terms of *Cooper pairs*, that is, paired electrons with opposite momentum and spin ( $\mathbf{k} \uparrow, -\mathbf{k} \downarrow$ ), and the BCS pairing wave-function  $|\psi_G\rangle$ , the ground state for many-body system in the superconducting state, which is evidently related to the order parameter in Ginzburg–Landau theory [21] and is proportional to the energy gap  $\Delta$  seen in the exponential temperature dependence  $e^{-\Delta/k_B T}$  in physical quantities such as the specific heat at low temperatures  $T$ . The pivotal object in BCS theory is the “Cooper pair” of electrons, which surprisingly extends in real space over a distance  $\xi$  much larger than the inter-atom distance and therefore strongly overlaps

with other Cooper pairs. Cooper showed that two electrons added to the Fermi sea  $|F\rangle$  at zero temperature can form a bound state, lowering the total system energy, no matter how weak the effective attraction between them is. While the effective attraction can be thought of as the net effect of two electrons interacting with the lattice at same location but different times<sup>1</sup>, it took great imagination and intuition for Schrieffer to write down the form for the ground state wave-function

$$|\psi_G\rangle = \prod_k (u_k + v_k c_{k\uparrow}^\dagger c_{-k\downarrow}^\dagger) |0\rangle, \quad (1-1)$$

where the variational parameters  $u_k$  and  $v_k$  satisfy  $|u_k|^2 + |v_k|^2 = 1$  and  $|0\rangle$  is the vacuum state (zero particle). The form in Eq. (1-1) implies a probability  $|v_k|^2$  for the pair  $(\mathbf{k} \uparrow, -\mathbf{k} \downarrow)$  to be occupied. The final step is to determine these probability amplitudes by minimizing the ground state energy  $\langle \psi_G | \mathcal{H} | \psi_G \rangle$  where the *pairing Hamiltonian* or *reduced Hamiltonian* is

$$H = \sum_{k\sigma} (\epsilon_k - \mu) c_{k\sigma}^\dagger c_{k\sigma} + \sum_{kl} V_{kl} c_{k\uparrow}^\dagger c_{-k\downarrow}^\dagger c_{-l\downarrow} c_{l\uparrow}. \quad (1-2)$$

Here the chemical potential  $\mu$  is included as a Lagrange multiplier to fix the mean number of particles, and  $V_{kl}$  is the effective electron-electron interaction due to phonon exchange. Although we won't show the derivation, it is worthwhile to mention that by assuming an attractive interaction  $V_{kl} = -V$  ( $V > 0$ ) for only states  $\mathbf{k}, \mathbf{l}$  in a shell near the Fermi surface with energy  $(E_F \pm \hbar\omega_c)$ , otherwise 0, a bounded ground state with lower energy than that of the normal metal can be found [22]. Here  $\omega_c$  is the cut-off frequency and in BCS theory it approximately equals the Debye frequency. The superconducting gap,  $\Delta \equiv V \sum_k \langle c_{-k\downarrow} c_{k\uparrow} \rangle$  where  $|(\mathbf{k} - \mathbf{k}_F) \cdot \mathbf{v}_F| < \omega_c$ , is assumed in BCS theory to

---

<sup>1</sup> The first electron causes a dynamic distortion somewhere in the lattice and induces a distorted positive ion-background, and then the second electron coming in the opposite direction to the distorted region of the lattice feels the attractive interaction from the positive ion-background.

be a constant in momentum space, and hence we call it *s*-wave pairing. BCS found the *universal* ratio  $\Delta/k_B T_c = \pi e^{-\gamma} \approx 1.76$ , which matches experiment values in the elements, such as Cd, Al, and Sn, remarkably well.

## 1.2 The Chronicle of Superconductivity: After BCS

BCS theory immediately fit the experimental measurements of the energy gap, the Meissner effect, the critical field and many others in simple elemental superconductors found at that time and gained great acceptance through the formal improvements by Anderson, Bogoliubov, Gor'kov, Abrikosov, Nambu and Eliashberg using the quantum field theory approach [23, 24]. However, problems came when the experiments showed absence of isotope effect in some transition metal superconductors, such as Rh [25], where  $T_c \propto M^{0\pm 0.1}$ . This in fact stimulated the quantitative consideration of the phonon effect that was oversimplified in BCS theory and the strong electron-phonon coupling theory was formulated by Eliashberg in 1960 with the Migdal treatment of electron-phonon interactions [26]. The strong-coupling theory ascribes the net effective attraction between electrons in a Cooper pair to the sum of the attractive electron-phonon interaction (characterized by the dimensionless quantity  $\lambda$ ) and the repulsive screened Coulomb interaction (characterized by  $\mu$ ). This theory still inherits the paradigm of the pairing mechanism in BSC theory: two electrons bind into Cooper pair under the effective attraction<sup>2</sup> through the *dynamic screening* mechanism [27], that is, two electrons at the same site “attract” each other at different times. As a generalized form including the original BCS theory as the weak-coupling limit, to date the strong-coupling theory (dynamic screening) is, as commented by Anderson [27], “one of the best-attested truths of quantum materials theory.” It reveals the essential physics of all *conventional* superconductors, and successfully explains

---

<sup>2</sup> The interaction is repulsive for the time less than the order of  $\hbar/E_F$  and goes attractive from  $\hbar/E_F$  to  $1/\Omega$ , where  $\Omega$  is a typical phonon frequency. See Ref. [10].

experiments on these materials. Nevertheless the theory based on the electron-phonon mechanism gives a discouraging prediction of the highest  $T_c$  that could be achieved in conventional superconductors: around 40 K [28–30]. MgB<sub>2</sub> discovered by the group of Akimitsu [31, 32] in 2001 has  $T_c = 39$  K, which is closest to the predicted limit among all known conventional superconductors.

Back to the history: things started to change in 1972 when the group of David Lee, Douglas Osheroff and Robert Richardson discovered that the liquid <sup>3</sup>He become superfluid at 2.5 mK [33], a phenomenon analogous to superconductivity, that is, the absence of viscosity at  $T < T_c$ .<sup>3</sup> Since superfluidity of <sup>3</sup>He can be explained with a  $p$ -wave pairing state, which from many aspects is different from the BCS formulation, we call it *unconventional* pairing. Afterwards, a turning point for superconductivity research came when the heavy fermion superconductor class was discovered in 1979 [36]. This class now includes Ce-based compounds (for example, CeCu<sub>2</sub>Si<sub>2</sub>, CeCoIn<sub>5</sub>, CePt<sub>3</sub>Si), U-based compounds (for example, UBe<sub>13</sub>, UPt<sub>3</sub>, URu<sub>2</sub>Si<sub>2</sub>) and other actinide-based compounds (PuCoGa<sub>5</sub>, PuRhGa<sub>5</sub> and NpPd<sub>5</sub>Al<sub>2</sub>) [37]. Most of these materials exhibit electronic properties consistent with extremely large effective masses,  $m^*/m_e \sim 100$ – $1000$ , as shown by experiments such as specific heat at low temperature and quantum oscillations. The experiments indicate the heavy fermion class has  $d$ ,  $p$  or  $f$ -wave pairing. Soon the second class of unconventional superconductors, organic superconductors, was discovered in 1980. However, a real challenge was posed by

---

<sup>3</sup> Although <sup>3</sup>He is a neutral particle while the electron is a charged particle (hence the phenomenon in the former is called superfluidity and the latter superconductivity), both are fermions and can pair in momentum space. The startling part about superfluidity in <sup>3</sup>He is that the pairing wave-function is  $p$  wave [34], an anisotropic pairing wave-function, making it the first unconventional superfluidity and the prototype for *unconventional* superconductivity. In fact 12 years before the discovery and a couple years after BCS theory, theorists, including Lev Pitaevskii, Emery and Sessler, Anderson and Morel, Vdovin, and Balian and Werthamer ([35] and references therein), had predicted the anisotropic pairing state in liquid <sup>3</sup>He, instead of the isotropic  $s$ -wave state.

the sensational discovery of cuprate superconductor class in 1986, as mentioned at the beginning of this chapter. The phase diagram of  $T_c$  with respect to electron or hole doping, the antiferromagnetic Mott insulator state at half filling, the extremely high  $T_c$  (with current records of 134 K at ambient and 164 K under high pressure for cuprates) and many other experimental facts all defy the conventional mechanism for superconductivity. Finally, the fourth unconventional superconductor class, iron-based superconductors (FeBS), was announced in 2008 [38, 39]. The highest  $T_c$  now achieved in FeBS is around 56 K. Unlike the heavy fermion class with  $T_c$  less than or equal to 2.3 K (CeCoIn<sub>5</sub>), the cuprates and FeBS both have unusually high  $T_c$  and hence their unconventional superconductivity is very easy to recognize; thus they immediately attracted worldwide attention from superconductivity community. The further discussions on the property of FeBS will be deferred to next section. Nevertheless it is useful to show basics of the crystal structure and the phase diagram of FeBS in comparison with cuprates before we discuss the pairing mechanism and theoretical model for unconventional superconductivity. As shown in Fig. 1-3, the active layers of cuprates and FeBS are both two-dimensional square lattices, which are responsible for the superconductivity as believed by most researchers. Their phase diagrams are also similar—both displaying antiferromagnetic phases at zero doping and “superconducting domes” with hole and electron doping. The differences are as follows. (i) The cuprates have a pure planar active layer while the FeBS have the pnictogen or chalcogen atoms buckling above and below the Fe layer. Therefore, for cuprates an effective one-band ( $d_{x^2-y^2}$  band is dominant) 2D model can crudely describe the electronic structure, while for FeBS all three  $t_{2g}$  bands ( $d_{xy}$ ,  $d_{xz}$ ,  $d_{yz}$ ) contribute states near the Fermi level and in some cases,  $e_g$  bands have to be included as well to account for a 3D Fermi surface. (ii) The undoped cuprate compound is a Mott insulator indicating strong electronic correlation, while the undoped FeBS compound is usually a metal, whose accurate Fermi surface, band structure, and the one-particle Hamiltonian can be reasonably

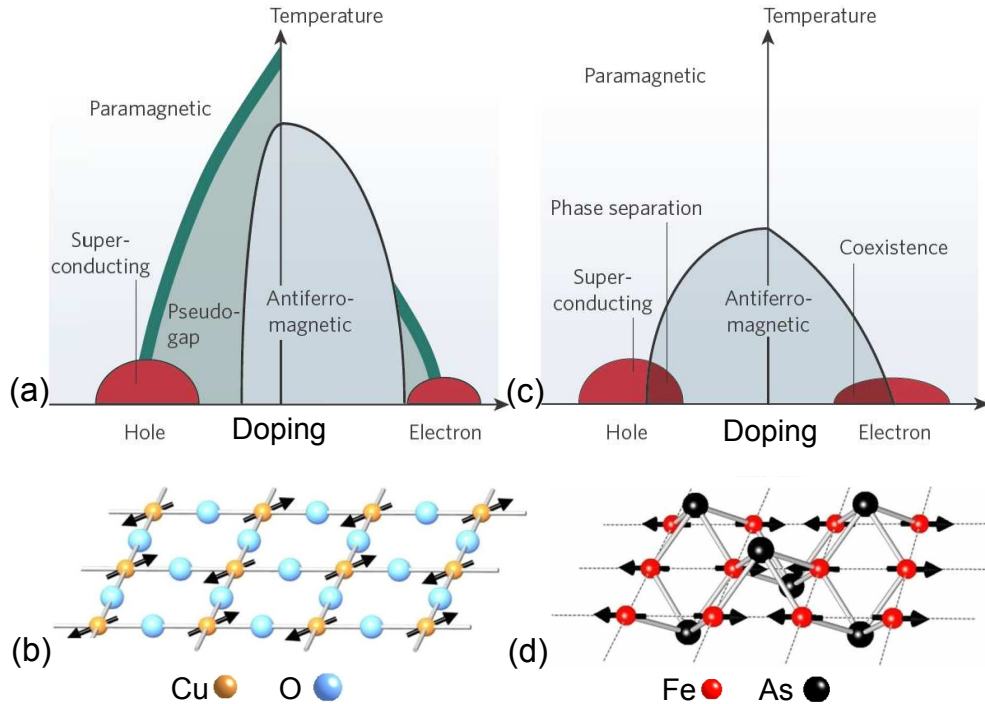


Figure 1-3. (a) Schematic phase diagrams of hole-doped (e.g.,  $\text{La}_{2-x}\text{Sr}_x\text{CuO}_4$ ) and electron-doped (e.g.,  $\text{Nd}_{2-x}\text{Ce}_x\text{CuO}_4$ ) cuprates. (c) Schematic phase diagrams of hole-doped (e.g.,  $\text{Ba}_{1-x}\text{K}_x\text{Fe}_2\text{As}_2$ ) and electron-doped (e.g.,  $\text{Ba}(\text{Fe}_{1-x}\text{Co}_x)_2\text{As}_2$ ) Fe-based superconductors. Both reprinted by permission from Macmillan Publishers Ltd: *Nature* [40], copyright 2010. (b), (d) The active layer of cuprates and Fe-based superconductors (reprinted with permission from [10], copyright 2012 by the American Physical Society).

well obtained from the density functional theory (DFT) calculation. (iii) The famous pseudogap phase is seen in cuprates, and may be related to charge/spin and other competing orders in the normal state while the FeBS do not evidently show such behavior. (iv) There are more diverse ways to dope the FeBS than the cuprates. In the latter, the dopant can either replace the spacer ions or be added as extra out-of-plane oxygen, while in the FeBS, the dopant can go into both the spacer ion plane and the active layer.

Now we discuss the probable pairing mechanism and pairing symmetry for the *unconventional superconductivity* in cuprates and FeBS, since their superconductivity can't be explained by the conventional BCS theory, where the Cooper pair evades the

“instantaneous”<sup>4</sup> Coulomb repulsion through the conventional dynamic-screening mechanism, that is, the paired electrons interact by exchanging the quanta of the lattice vibrations (the phonon) to avoid each other in time. To fully take advantage of the effective attraction, the pairing state takes a symmetric form—relative *s*-wave state. On the other hand, in unconventional superconductivity the electrons in the Cooper pair can avoid each other in space, resulting in an anisotropic pairing state. Physically this mechanism is unconventional but simpler than the first one in the sense that it doesn’t involve the phonon and thus is possible to explain the high  $T_c$  that is restricted by the lattice instability in conventional superconductivity; however, it is also complicated because in this purely electronic mechanism the electrons being paired and the bosons being exchanged are the same particles, and there is no clear separation of time scales. In addition, the induced effective attraction is itself a function of the pairing state, which makes the full pairing problem below  $T_c$  extremely difficult to solve. Consequentially a correct minimal model Hamiltonian is essential to solve such a complex problem as in high  $T_c$  of cuprates or FeBS. Anderson was the first one to propose that the deceptively simple 2D single band Hubbard model could account for the superconductivity of cuprates [41]. The famous single band Hubbard Hamiltonian [42] reads

$$H = \sum_{ij\sigma} t_{ij} c_{i\sigma}^\dagger c_{j\sigma} + U \sum_i n_{i\uparrow} n_{i\downarrow}, \quad (1-3)$$

where  $t_{ij}$  are tight-binding one-electron hopping parameters between sites  $i$  and  $j$ , which are adjusted to fit the band structure, and  $U$  is an on-site Coulomb interaction. The Hubbard Hamiltonian, Eq. (1-3), can produce a variety of phases seen in cuprates, despite having only one parameter  $t/U$  to tune. For example, when  $U$  is small, Eq. (1-3) describes a simple metal; when  $U$  is large, we have antiferromagnetic Mott insulator

---

<sup>4</sup> This is a legitimate approximation in condensed matter physics. Physically, Coulomb interaction is also retarded in nature due to the causality.

at half filling. However, there are no well-controlled analytical techniques to solve this model in the entire doping range in higher dimensions, although many semi-analytical methods, such as random phase approximations (RPA), renormalized mean-field theory, conserving fluctuation exchange (FLEX), and slave-boson approximations, have been applied (see Ref. [10] and references therein). In this situation, the numerical simulation might be the only approach feasible to justify whether this model characterizes cuprates and gives rise to the unconventional superconductivity at a proper doping, but unfortunately quantum Monte Carlo approaches are limited to higher temperatures due to the fermion sign problem [43]. Recently, in the  $U/t \rightarrow 0$  limit, this simple model was shown to have a transition to  $d_{x^2-y^2}$ -wave superconducting phase [44] in a rigorous weak-coupling approach.

In 1994, the extra broken symmetry of  $d_{x^2-y^2}$ -wave state (under  $90^\circ$  rotation about the principal axis of the lattice) in cuprates was definitively observed by the ingenious tricrystal tunneling experiment [45] and later confirmed in a wide doping range including electron doping. However, the pairing symmetry for FeBS is still highly debated since the inescapable multiband feature blends more subtleties into the problem and it is rather challenging to give a unified picture for the continuously expanding families of chemical compounds. Since the superconducting phase is often in close proximity to an antiferromagnetic semimetal phase at zero doping in the phase diagrams of FeBS, it is intuitive to propose an  $s_{\pm}$ -wave state [46] based on antiferromagnetic spin-fluctuation theory, where the gap changes sign between the portion of electron and hole Fermi sheets connected by the wave vector  $\mathbf{Q}$  (see Fig. 1-4). The essence of the argument for the  $s_{\pm}$ -wave state given by the spin-fluctuation theory is physically straightforward: if the repulsive pairing interaction  $V_{\mathbf{k}\mathbf{p}} = V(\mathbf{k} - \mathbf{p})$  in the spin singlet channel due to the spin fluctuations has a strong momentum dependence, the usual BCS gap equation  $\Delta_{\mathbf{k}} = -\sum_{\mathbf{p}} V(\mathbf{k} - \mathbf{p})\Delta_{\mathbf{p}}/E_{\mathbf{p}}$  requires the gap function  $\Delta_{\mathbf{k}}$  to change sign accordingly; in FeBS with multiple Fermi surface sheets (pockets), the peak of spin susceptibility at  $\mathbf{Q}$

dictates a sign-changing gap  $\Delta_{\mathbf{k}+\mathbf{Q}} = -\Delta_{\mathbf{k}}$  where  $\mathbf{Q}$  is the nesting vector between the hole and electron pockets, and furthermore the gap on each pocket is isotropic  $s$ -wave form or anisotropic extended  $s$ -wave form. (In cuprates, due to the relatively simple large Fermi surface, the gap function acquires a strongly angular dependence in the  $d$ -wave form [47].) This antiferromagnetic spin-fluctuation mediated  $s_{\pm}$ -wave pairing is consistent with a number of experiments; nevertheless, when orbital-fluctuations are strong, another theory [48] suggests an  $s_{++}$ -wave gap, where the gap (or gap averaged over each Fermi pocket) has the same sign everywhere. Furthermore, other symmetries, such as  $d$  wave and  $s + id$  wave, are also proposed for some compounds of FeBS. Ref. [8] includes a comprehensive review on gap symmetries in FeBS. Now it is generally believed that in both cuprates and FeBS the pairing state is unconventional, and the screened Coulomb interaction that actually causes the pairing is attractive at relative separations of order a lattice spacing or more [10].

To sum up, except for the agreement that an electronic mechanism is the major actor in the pairing, we are still far from reaching a consensus on the unconventional pairing mechanism after nearly two decades' research for cuprates and a half decade for FeBS, because formulating a complete pairing mechanism for unconventional superconductivity is a rather deep and hard problem. Only when it is solved, will the theorists be able to predict new high  $T_c$  superconductors, will the experimentalists design high  $T_c$  superconductors from a "blueprint", and will the scientists revolutionize the technology with the "Holy Grail" of high  $T_c$ . Completely solving this fundamental problem is beyond the scope of this dissertation. Instead, we will discuss the theory of gap symmetry and gap structure, a hint for understanding the high  $T_c$  in FeBS. In the following chapters, we phenomenologically explain the experimental observations and their interpretations on the symmetry of pairing order parameter. In the final chapter, we use the multiband Hubbard-Hund Hamiltonian generalized from Eq. (1–3) to microscopically investigate the pairing symmetry in FeBS by spin-fluctuation theory.

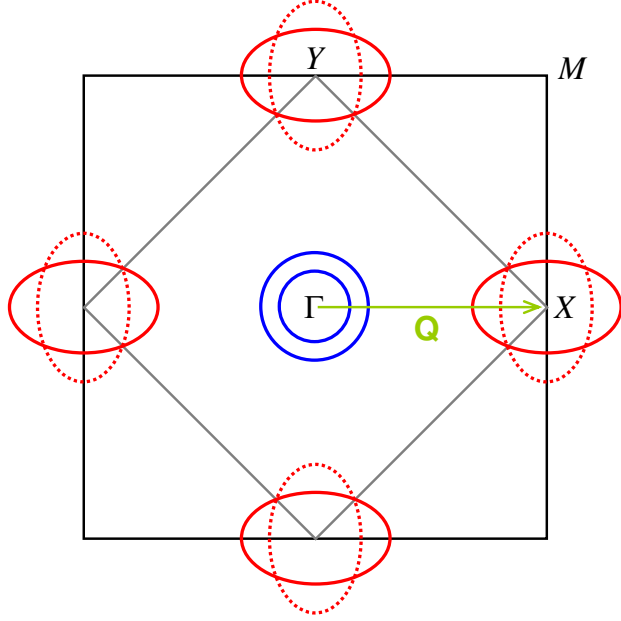


Figure 1-4. The generic Fermi surface of FeBS in the two-Fe Brillouin zone (gray square). The black square is one-Fe Brillouin zone. Two hole pockets at  $\Gamma$  and two electron pocket at  $X$  or  $Y$  are shown. The  $s_{\pm}$  gap is illustrated:  $\Delta(\mathbf{k}) = -\Delta_0$  for  $\mathbf{k}$  near  $\Gamma$  and  $\Delta(\mathbf{k} + \mathbf{Q}) = \Delta_0$  for  $\mathbf{k} + \mathbf{Q}$  near  $X$  or  $Y$  (red color for positive gap and blue color for negative gap). The gap changes sign between the pockets connected by  $\mathbf{Q} = (\pi, 0)$ .

### 1.3 The Symmetry Properties of Fe-Based Superconductors

#### 1.3.1 Crystal Structure and Crystal Symmetry

We investigate the crystal structure and crystal symmetry of FeBS since the pairing state (see next section), the superconducting ground state of the system Hamiltonian, must be a linear combination of the basis functions of an irreducible representation of the symmetry group of the system Hamiltonian. If we simply take the symmetry group to be the point group of the crystal, the pairing state can then be classified by different irreducible representations of the point group.<sup>5</sup> The FeBS include different families

<sup>5</sup> In fact the symmetry group  $\mathcal{G}$  of the system Hamiltonian consists of the permutation group (the exchange symmetry of fermions), the space group  $G$  of the crystal, the spin-rotation symmetry group  $SU(2)$ , the time-reversal symmetry group  $\mathcal{K}$ , and the gauge symmetry group  $U(1)$  [49]. Without spin-orbit coupling, the above individual groups can be treated independently and we will mostly consider this situation.

which are named according to the chemical formula of the parent compound (i.e. zero doping) as 1111, 122, 111, 11 for the major families, as shown in Fig. 1-5. The space group of a single Fe-As/Se layer is  $P4/nmm$ , a nonsymmorphic group. Nonsymmorphic groups are nonsimple space groups containing glide planes and screw axes. These are symmetry operations (group elements) combining a reflection or rotation with a non-integer translation. From Fig. 1-5, one can see that there are two ways to stack the Fe-As/Se layer, i.e., in-phase as in 1111, 111 and 11 and anti-phase as in 122. The space group of the crystal constructed in the first way is still  $P4/nmm$  while the space group of 122 is symmorphic space group  $I4/mmm$ . Both are space groups of tetragonal lattice and the corresponding point group can be derived from dihedral group  $D_2$  or  $D_4$  as in cuprates.

### 1.3.2 Gap Symmetry and Gap Structure

Mostly we consider a singlet pairing state, where the pairing gap  $\Delta_{\mathbf{k}}$  has even parity (under the change  $\mathbf{k} \rightarrow -\mathbf{k}$ ) since the total wave-function is antisymmetric for fermions. For the even parity part, the point group  $D_{4h}$  for the tetragonal system has four one-dimensional irreducible representations,  $A_{1g}$ ,  $A_{2g}$ ,  $B_{1g}$ , and  $B_{2g}$ , and one two-dimensional irreducible representation  $E_{2g}$  (here  $g$  denotes even parity). One can simply read a character table for the eigenvalues of irreducible representations under different symmetry operations. For simplicity we only list in Table 1-1 the irreducible representations, some basis functions, and the nomenclature of the gap

---

Furthermore, the space group  $G$  of the crystal can be factorized into the translation group and rotation group  $T \otimes R$  for symmorphic space groups while this is impossible for nonsymmorphic groups and instead the quotient group  $G/T$  is used. The rotation group  $R$  or the quotient group  $G/T$  is the group of wavevector  $\Gamma(0, 0, 0)$ ; the groups of other wavevectors  $\mathbf{k}$  are subgroups of  $R$  for symmorphic space groups but special treatment is necessary for nonsymmorphic groups [50, 51]. When classifying the symmetry of the pairing state, we refer to the group of wavevectors or, loosely speaking, the point group of the crystal.

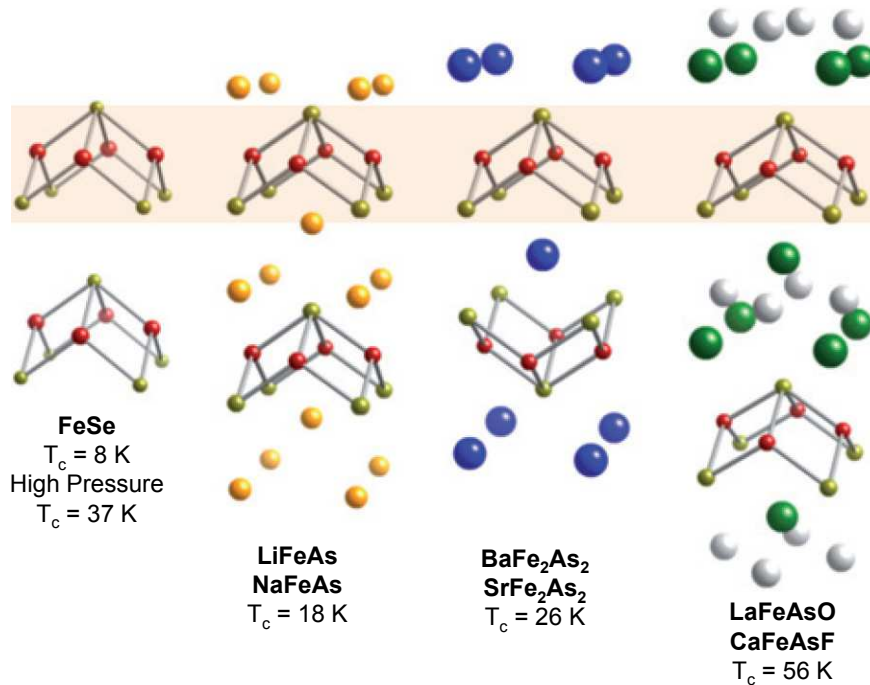


Figure 1-5. Crystal structures of FeBS for 11 (FeSe), 111 (LiFeAs), 122 (BaFe<sub>2</sub>As<sub>2</sub>), 1111 (LaFeAsO) families (reprinted by permission from Macmillan Publishers Ltd: *Nat. Phys.* [5], copyright 2010). Some of the labeled transition temperatures are achieved by doping or pressure.

functions analogous to eigenfunctions in the isotropic case. The discussion here applies to both cuprates and FeBS. However, in FeBS the Fermi surface includes electron and hole pockets, as shown in Fig. 1-4. The existence of separate pockets gives unique properties to FeBS under the restriction of the symmetry. The gap  $\Delta_k$  on different pockets can have different signs and values, making FeBS multigap superconductors. The zeros of the gap functions on the Fermi surface, i.e., the nodes, affect the experiments measuring the low energy excitations and change the exponential temperature dependence  $e^{-\Delta/T}$  to power law dependence  $T^\alpha$ . From the symmetry argument, a  $d$ -wave gap must have nodes on the hole pockets in the direction determined by the symmetry; while an  $s$ -wave gap can in principle also have “accidental” nodes at some directions not necessarily related to the symmetry.  $s_{\pm}$ - and  $s_{++}$ -wave pairing are suggested for the superconductivity in FeBS by antiferromagnetic spin-fluctuation theory and orbital fluctuation theory, respectively. Belonging to the

Table 1-1. Irreducible representations and gap functions for singlet pairing in the tetragonal symmetry

| irreducible representation | basis function                            | $\Delta_{\mathbf{k}}$ |
|----------------------------|---|-----------------------|
| $A_{1g}$                   | $1, \cos k_x + \cos k_y$                  | $s$ wave              |
| $A_{2g}$                   | $\sin k_x \sin k_y (\cos k_x - \cos k_y)$ |                       |
| $B_{1g}$                   | $\cos k_x - \cos k_y$                     | $d_{x^2-y^2}$ wave    |
| $B_{2g}$                   | $\sin k_x \sin k_y$                       | $d_{xy}$ wave         |
| $E_{2g}$                   | $\sin k_x \sin k_z, \sin k_y \sin k_z$    |                       |

same  $A_{1g}$  irreducible representation, they are predicted by different microscopic mechanisms, and it is crucial to distinguish them for understanding the superconductivity of FeBS. Currently, three experiments offer indirect evidence supporting the  $s_{\pm}$  pairing: the nearly ubiquitous observation of neutron spin resonance features in inelastic neutron spectroscopy (INS) [52–57], a quasiparticle interference scanning tunneling spectroscopy (STS) experiment in a magnetic field [58], and a phase-sensitive experiment on a polycrystalline sample which relies on significant statistical analysis [59]. Here, I will briefly discuss why neutron spin resonance experiments support  $s_{\pm}$  pairing. Neutron scattering measures the dynamical spin susceptibility  $\chi_s(\mathbf{q}, \omega)$  which can be calculated with RPA as  $\chi_s(\mathbf{q}, \omega) = [1 - U_s \chi_0(\mathbf{q}, \omega)]^{-1} \chi_0(\mathbf{q}, \omega)$ , where  $\chi_0(\mathbf{q}, \omega)$  is the bare electron-hole bubble. In the superconducting state, due to the presence of finite gap,  $\text{Im} \chi_0(\mathbf{q}, \omega)$  has a sudden jump from zero to a finite value proportional to the coherence factor  $\sum_{\mathbf{k}} \left[ 1 - \frac{\Delta_{\mathbf{k}} \Delta_{\mathbf{k}+\mathbf{q}}}{E_{\mathbf{k}} E_{\mathbf{k}+\mathbf{q}}} \right]$  at a threshold frequency  $\omega \sim \Omega_c$ . This leads to a subgap peak called the spin resonance peak in the RPA dynamical susceptibility at the antiferromagnetic wave vector. It is only visible in the neutron scattering spectrum when the coherence factor is nonzero, indicating  $\text{sgn} \Delta_{\mathbf{k}} \neq \text{sgn} \Delta_{\mathbf{k}+\mathbf{q}}$ , where  $\mathbf{q}$  is the scattering wave vector where  $\chi_s(\mathbf{q}, \omega)$  is peaked. Clearly, the  $s_{\pm}$  state satisfies this condition while the  $s_{++}$  doesn't.

## CHAPTER 2 INHOMOGENEOUS SUPERCONDUCTIVITY

Some parts of this chapter have been published as “Volovik effect in a highly anisotropic multiband superconductor: experiment and theory,” Yan Wang, J.-S. Kim, G. Stewart, P. J. Hirschfeld, Y. Matsuda, T. Shibauchi, S. Graser, and I. Vekhter, *Phys. Rev. B* **84**, 184524 (2011), and “Theory of quasiparticle vortex bound states in Fe-based superconductors: application to LiFeAs,” Yan Wang, P. J. Hirschfeld, and I. Vekhter, *Phys. Rev. B* **85**, 020506 (2012).

Inhomogeneous superconductivity is a quite broad topic since the inhomogeneity in the superconducting state arises from different aspects and various scenarios such as applied magnetic field, low dimensionality or size effect and the existence of surfaces, interfaces or defects. Accordingly, the homogeneous superconductor can undergo a transition to the mixed (or intermediate) state in Type I superconductors, to the vortex state in Type II superconductors, or to the Fulde-Ferrell-Larkin-Ovchinnikov (FFLO) state in, for instance, heavy-fermion and organic superconductors. The order parameter  $\Delta(\mathbf{x})$  of these inhomogeneous pairing states has variations in real space  $\mathbf{x}$ . The consequences and behaviors of pair breaking due to the magnetic field in these superconductors are more complicated than that due to disorder: The former results in new nontrivial pairing states with suppression of the magnitude of order parameter in the coherence length scale  $\xi$  or sign changing order parameter in the scale of  $1/k_F$ , while the latter, the pair breaking due to disorder (the focus of next chapter), suppresses the order parameter in real space uniformly in the sense of disorder average. (However, with experimental techniques in atomic or sub-atomic scale such as scanning tunneling spectroscopy, the inhomogeneous superconductivity due to disorder on short distance scales can be mapped out and used as further probes for the pairing interaction and pairing symmetry [60]). In dealing with such an extensive topic, we will concentrate on the superconductivity in the vortex state in this chapter. First, we present measurements

of the specific heat coefficient  $\gamma \equiv C/T$  in the low temperature limit as a function of an applied magnetic field for the Fe-based superconductor  $\text{BaFe}_2(\text{As}_{0.7}\text{P}_{0.3})_2$  by G. R. Stewart's group, where both a linear regime at higher fields and a limiting square root  $H$  behavior at very low fields are found. The crossover from a Volovik-like  $\sqrt{H}$  to a linear field dependence can be understood from a multiband calculation in the quasiclassical approximation assuming gaps with different momentum dependence on the hole- and electron-like Fermi surface sheets. Next, we consider the vortex bound states and show that the high intensity tails in the scanning tunneling spectroscopy (STS) on these low-energy states may indicate either the gap anisotropy or the Fermi surface anisotropy in the momentum space. If the Fermi surface anisotropy dominates, preventing direct observation of superconducting gap features, one must be cautious to analyze the STS data on Fe-based superconductors in the vortex state, in particular LiFeAs, which we treat explicitly.

## 2.1 Quasiclassical Approximation

The quasiclassical (Eilenberger) approximation [61–63] is a powerful tool to describe the electronic properties of the superconducting state on large scales compared to the lattice spacing, provided the quasiclassical condition  $k_F \xi \gg 1$  is satisfied. Here  $k_F$  is the Fermi momentum and  $\xi$  the coherence length. Since in this limit we can think of quasiparticles as propagating coherently along a well-defined trajectory in real space, this method is particularly well suited to address the inhomogeneous situations, such as the vortex state of type-II superconductors (SCs). An alternative and frequently used approach to the vortex state is to take into account the (classical) shift of the quasiparticle energy due to the local supercurrent flow. Such an approximation, often referred to as the Doppler-shift approach, is valid for nodal SCs with considerable weight of extended quasiparticle excitations outside the vortex cores. Using this method, Volovik showed that for superconductors with line nodes these extended quasiparticle excitations lead to a non-linear magnetic field dependence of the spatially

averaged residual density of states  $N(\omega = 0, H) \propto N_0 \sqrt{H/H_{c2}}$ , a result known as the *Volovik effect* [64]. This behavior was first confirmed by measurements of the specific heat [65, 66] and by subsequent calculations within the quasiclassical approximation for both a single vortex in a  $d$ -wave SC [67, 68] and for a vortex lattice [69, 70]. Both quasiclassical and Doppler-shift methods fail at the lowest temperatures due to quantum effects [71], but in known systems with  $T_c \ll E_F$  these effects are negligible in practice. Both methods have successfully explained at a semiquantitative level the magnetic field dependence of the specific heat and thermal conductivity in a wide variety of unconventional superconductors [72]. It was also shown that the accurately calculated quasiparticle excitation spectrum is consistent with STM studies of the electronic structure around a vortex core [69].

Many experimental techniques which are sensitive to the low-energy density of states, such as thermal conductivity, specific heat, and NMR relaxation rate, can be used to draw conclusions about the possible existence and the momentum dependence of quasiparticle excitations in the bulk of iron-based superconductors and thus about the structure of the superconducting gap and the distribution of gap nodes. The low  $T$  limit of the Sommerfeld coefficient in an applied magnetic field,  $\gamma(H)$ , is directly proportional to the spatially averaged local density of states (LDOS) at the Fermi level. The Doppler-shift method was used to calculate the LDOS for a two-band SC with two isotropic gaps of unequal size  $\Delta_S \neq \Delta_L$  and to give an interpretation of the experimental data available at that time [73]. However, the Doppler-shift approach cannot account properly for the contributions from the states in the vortex core that have a very large weight in the net DOS and hence gives a quantitatively and sometimes qualitatively inaccurate description of the electronic structure of the vortex. For example, in a simple  $d$ -wave superconductor the spatial tails of the low-energy density of states around the vortex are aligned in the wrong directions [74]. To obtain a quantitative fit to the specific heat data by G. R. Stewart's group and to allow for a more decisive conclusion

about the gap structure of  $\text{BaFe}_2(\text{As}_{0.7}\text{P}_{0.3})_2$ , we will therefore use the quasiclassical approximation, which we will briefly review in the following paragraphs.

In the quasiclassical method, the Gor'kov Green's functions are integrated with respect to the quasiparticle energy measured from the Fermi level. The normal and anomalous components  $g(\mathbf{r}, \theta, i\omega_n)$  and  $f(\mathbf{r}, \theta, i\omega_n)$  of the resulting propagator  $\hat{g}$  obey the coupled Eilenberger equations

$$\begin{aligned} \left[ 2 \left( i\omega_n + \frac{e}{c} \mathbf{v}_F \cdot \mathbf{A}(\mathbf{r}) \right) + i\hbar \mathbf{v}_F \cdot \nabla \right] f(\mathbf{r}, \theta, i\omega_n) &= 2ig(\mathbf{r}, \theta, i\omega_n)\Delta(\mathbf{r}, \theta), \\ \left[ 2 \left( i\omega_n + \frac{e}{c} \mathbf{v}_F \cdot \mathbf{A}(\mathbf{r}) \right) - i\hbar \mathbf{v}_F \cdot \nabla \right] \bar{f}(\mathbf{r}, \theta, i\omega_n) &= 2ig(\mathbf{r}, \theta, i\omega_n)\Delta^*(\mathbf{r}, \theta), \end{aligned} \quad (2-1)$$

that have to be complemented by the normalization condition  $\hat{g}^2 = \hat{1}$ , where

$$\hat{g} \equiv \begin{pmatrix} g & f \\ \bar{f} & -g \end{pmatrix}. \quad (2-2)$$

Here  $\Delta(\mathbf{r}, \theta)$  is the order parameter,  $\mathbf{A}(\mathbf{r})$  the vector potential,  $\mathbf{v}_F$  is the Fermi velocity at the location on the Fermi surface labeled by  $\theta$ , and  $\omega_n = (2n + 1)\pi k_B T$  are the fermionic Matsubara frequencies. For two-dimensional cylindrical Fermi surfaces such as considered below,  $\mathbf{v}_F = v_F \hat{\mathbf{k}}$  where  $\hat{\mathbf{k}} = (\cos \theta, \sin \theta)$  and  $\theta$  is the angle measured from the [100] direction. In that case it is natural to write the position vector in cylindrical coordinates,  $\mathbf{r} = (\rho, \phi, z)$ , where  $\phi$  is the winding angle around the vortex in real space.

Making use of the symmetries [75] of the quasiclassical propagator

$$\bar{f}(\mathbf{r}, \mathbf{k}_F, i\omega_n) = f^*(\mathbf{r}, \mathbf{k}_F, -i\omega_n), \quad (2-3)$$

$$f(\mathbf{r}, -\mathbf{k}_F, -i\omega_n) = f(\mathbf{r}, \mathbf{k}_F, i\omega_n), \quad (2-4)$$

$$g(\mathbf{r}, \mathbf{k}_F, i\omega_n) = g^*(\mathbf{r}, \mathbf{k}_F, -i\omega_n), \quad (2-5)$$

the diagonal part of the normalization condition can be written in a more explicit form as  $[g(\mathbf{r}, \theta, i\omega_n)]^2 + f(\mathbf{r}, \theta, i\omega_n)f^*(\mathbf{r}, \theta + \pi, i\omega_n) = 1$ . Note that our notation of  $g$ ,  $f$ , and  $\bar{f}$  differs from the one used in Ref. [75]. Under the transformation  $g \rightarrow -i\pi g$ ,

$f \rightarrow \pi f$ , and  $\bar{f} \rightarrow -\pi\bar{f}$  the notation in Ref. [75] passes into our notation. Instead of solving the complicated coupled Eilenberger equations everywhere in space, we follow Refs. [68, 75] and parameterize the quasiclassical propagator along real space trajectories  $\mathbf{r}(x) = \mathbf{r}_0 + x\hat{\mathbf{v}}_F$  by a set of scalar amplitudes  $a(x)$  and  $b(x)$ ,

$$\hat{g}(\mathbf{r}(x)) = \frac{1}{1 + a(x)b(x)} \begin{pmatrix} 1 - a(x)b(x) & 2a(x) \\ 2b(x) & -1 + a(x)b(x) \end{pmatrix}. \quad (2-6)$$

These amplitudes obey numerically stable Riccati equations which follow from substitution into Eq. (2-1),

$$\begin{aligned} v_F \partial_x a(x) + [2\tilde{\omega}_n + \Delta^*(x)a(x)]a(x) - \Delta(x) &= 0, \\ v_F \partial_x b(x) - [2\tilde{\omega}_n + \Delta(x)b(x)]b(x) + \Delta^*(x) &= 0. \end{aligned} \quad (2-7)$$

For the single vortex problem the spatial dependence vanishes far away from the vortex core, and hence we have the initial conditions

$$\begin{aligned} a(-\infty) &= \frac{\Delta(-\infty)}{\omega_n + \sqrt{\omega_n^2 + |\Delta(-\infty)|^2}}, \\ b(+\infty) &= \frac{\Delta^*(+\infty)}{\omega_n + \sqrt{\omega_n^2 + |\Delta(+\infty)|^2}}. \end{aligned} \quad (2-8)$$

Here we have set  $\hbar = 1$  and we have introduced the modified Matsubara frequencies  $i\tilde{\omega}_n(x) = i\omega_n + (e/c)\mathbf{v}_F \cdot \mathbf{A}(x)$ . Since the modification of the Matsubara frequencies due to the external field is of the order of  $1/\kappa^2$  where  $\kappa = \lambda_L/\xi$  is the ratio of the London penetration depth and the coherence length, the term proportional to  $\mathbf{A}(x)$  in Eq. (2-7) can be neglected for strong type-II superconductors with large  $\kappa$ .

After an analytic continuation of the Matsubara frequencies to the real axis,  $i\omega_n \rightarrow \omega + i\delta$ , the local density of states can be calculated as the Fermi surface average of the quasiclassical propagator

$$N(\mathbf{r}) = N_0 \int_0^{2\pi} \frac{d\theta}{2\pi} \text{Re} \left( \frac{1 - ab}{1 + ab} \right)_{i\omega_n \rightarrow \omega + i\delta}, \quad (2-9)$$

where  $N_0$  is the normal density of states at the Fermi energy. To obtain stable numerical solutions we use a small imaginary part  $\delta = 0.02 T_c$  in the analytical continuation, where  $T_c$  is the critical temperature of the superconductor.

## 2.2 Volovik Effect in Multiband Superconductor $\text{BaFe}_2(\text{As}_{0.7}\text{P}_{0.3})_2$

### 2.2.1 Motivation

The symmetry and detailed structure of the gap function in the recently discovered iron pnictide [39] and chalcogenide [76] high temperature superconductors is still under discussion. Across an increasingly numerous set of materials families, as well as within each family where superconductivity can be tuned by doping or pressure, experimental indications are that there is no universal gap structure [6, 7]. Instead, the superconducting gap appears to be remarkably sensitive to details of the normal state properties. This “intrinsic sensitivity” [77] may be due to the unusual Fermi surface topology, consisting of small hole and electron pockets, and to the probable  $A_{1g}$  symmetry of the superconducting gap which allows a continuous deformation of the order parameter structure from a fully gapped system to one with nodes (for a review see, e.g. Ref. [8]). It is important to keep in mind, though, that another possibility to account for the observed variability is that different experiments on the same material may probe selectively different Fermi surface regions and hence different gaps within the system.

The Ba-122 family of materials has been intensively studied because large high quality single crystals are relatively easy to produce [6, 78]. Within this family, the isovalently substituted system  $\text{BaFe}_2(\text{As}_{1-x}\text{P}_x)_2$  with a maximum  $T_c$  of 31 K is particularly intriguing because it exhibits a phase diagram and transport properties remarkably similar to the heterovalently doped system  $\text{Ba}(\text{Fe}_{1-x}\text{Co}_x)_2\text{As}_2$  and displays many signatures of apparent quantum critical behavior at optimal doping [78–80]. In the superconducting state, penetration depth [81], NMR spin-lattice relaxation [82], thermal conductivity temperature dependence [81], and thermal conductivity angular

field variation [83] show clear indications of nodal behavior. Surprisingly, a linear field dependence of the specific heat Sommerfeld coefficient  $\gamma$  was measured [84] on optimally doped samples from the same batch. Such a behavior is expected for a fully gapped single band superconductor since the fermionic excitations from the normal cores of vortices provide the only contribution to  $\gamma$  at low  $T$ , and the number of these vortices scales linearly with the field  $H$ . It was argued in Ref. [84] that the specific heat measurement might be consistent with the other experiments suggesting nodes if the heavy hole sheets in the material were fully gapped, while the gaps on the lighter electron sheets were nodal. In such a case the  $\gamma \sim \sqrt{H}$  behavior would be difficult to observe in experiment.

In Ref. [84], the G. R. Stewart group reported experimental data on the magnetic field dependence of the specific heat of optimally doped  $\text{BaFe}_2(\text{As}_{1-x}\text{P}_x)_2$  samples, up to 15 T. More precise measurements [85] at low fields revealed the presence of a Volovik-like  $\sqrt{H}$  term which persists roughly over a range of 4 T, crossing over to a linear behavior above this scale.<sup>1</sup> The observation of this term, consistent with nodes in the superconducting gap, therefore supported claims made in earlier work [81–83], without the need to assume an extremely large mass on the hole pockets.

Theoretical estimates using the Doppler shift method for isotropic gaps given in Ref. [73] were oversimplified, but did show the need for a more thorough analysis of anisotropic multiband systems. The theoretical difficulties can be seen easily by considering a simple two-band model with two distinct gaps  $\Delta_1$  and  $\Delta_2$ , where we assume for the moment that  $\Delta_2 > \Delta_1$ . If the two bands are uncoupled, the two gaps correspond to two independent coherence lengths  $\xi_i \simeq v_{F,i}/(\pi\Delta_i)$ , where  $i = 1, 2$ , and

---

<sup>1</sup> In contrast to  $\text{BaFe}_2(\text{As}_{1-x}\text{P}_x)_2$ , recent high field measurements on underdoped ( $x = 0.045$ ) and overdoped ( $x = 0.103$ )  $\text{Ba}(\text{Fe}_{1-x}\text{Co}_x)_2\text{As}_2$  have found that the specific heat coefficient varies approximately as  $H^{0.7}$  all the way up to  $H_{c2}(0)$  [86].

two independent “upper critical fields”  $H_{c2,i}$ . Vortex core states of the large gap  $\Delta_2$  are confined to cores of radius  $\sim \xi_2$ . For fields in the range  $H_{c2,1} \lesssim H \lesssim H_{c2,2}$ , the vortex cores of the small gap will overlap, while the large gap cores will still be well separated. Note that if  $\Delta_1$  is very small (these considerations also crudely describe nodal gaps), this field range can be wide and extend to quite low fields. On the other hand, methods of studying quasiparticle properties in superconductors are typically adapted to calculating near  $H_{c1}$  or  $H_{c2}$ , i.e. in the limit of widely separated or nearly overlapping vortices. The current problem apparently contains elements of both situations. In the absence of interband coupling, of course, one can use different methods, corresponding to the appropriate field regimes, for the distinct bands. For coupled Fermi surfaces, however, such an approach is not viable. In the immediate vicinity of the transition, where the Ginzburg-Landau expansion is valid, there is a single length scale controlling the vortex structure [87]. At low temperatures, where the measurements are carried out, however, the distinct length scales likely survive, although they are modified by the strength of the interband coupling, see below. Possible anisotropy of the gap on one or more Fermi surface sheets complicates the picture even further. We showed in Ref. [85] that judicious use of the quasiclassical approximation even with simplifying assumptions about the vortex structure can provide a general framework for the description of this problem, and a semiquantitative understanding of the new data on the  $\text{BaFe}_2(\text{As}_{1-x}\text{P}_x)_2$  system.

In the following, we first present experimental results on the  $\text{BaFe}_2(\text{As}_{1-x}\text{P}_x)_2$  system in Sec. 2.2.2 obtained by the G. R. Stewart group. In Sec. 2.2.3 we discuss the two-band quasiclassical model we use to study the system, and in Sec. 2.2.4 we give our theoretic results. Finally in Sec. 2.2.5 we present our conclusions.

## 2.2.2 Experiment Results

Preparation of the crystals and experimental setup for specific heat measurements was described in Ref. [85]. The specific heat coefficient  $\gamma \equiv C/T$  of  $\text{BaFe}_2(\text{As}_{0.7}\text{P}_{0.3})_2$

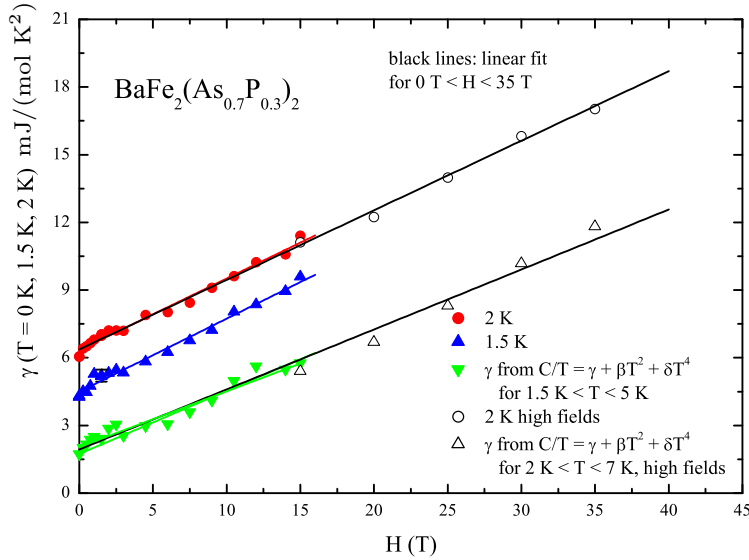


Figure 2-1. The original specific heat data [84] on  $\text{BaFe}_2(\text{As}_{0.7}\text{P}_{0.3})_2$  as a function of field up to 15 T (solid symbols) with data between 15 T and 35 T (open symbols). Note the agreement between the linear,  $C/T \propto H$ , extrapolation of the 15 T (colored lines [84]) and 35 T (black lines, present work) results. We extract  $\gamma$  from the data using two (equivalent) methods: (a) by making an extrapolation  $C/T = \gamma + \beta T^2 + \delta T^4$  from 2 K and above, or (b) by taking the smoothed value of  $C/T$  at 1.5 and 2 K found by fitting approximately 10 data points around these temperatures to obtain  $C/T$  (1.5 K) and  $C/T$  (2 K) with decreased scatter. The temperature restriction eliminates both the influence of the anomaly and the field-induced nuclear contribution, negligible for  $H \leq 4$  T above 1 K. The absolute accuracy of these data is  $\pm 5\%$  (error bars are not shown at low fields since they are approximately the same size as a data point) while the precision of the data is approximately  $\pm 2\%$ . In addition, additional data with finer gradations in the measured fields up to 4 T were taken to explore the low field non-linear behavior. These data are shown on an expanded scale in Fig. 2-2.

for  $0 \leq H \leq 35$  T is shown by the open triangles in Fig. 2-1. There is a small low temperature anomaly in the specific heat data below about 1.4 K (discussed in detail in Ref. [84]). Such anomalies have been observed in other Fe/Pn samples [88], and in some cases, e.g., in  $\text{Ba}(\text{Fe}_{1-x}\text{Co}_x)_2\text{As}_2$ , they show a rather strong magnetic field dependence [88]. However, as discussed in Ref. [84] for the data up to 15 T, the anomaly in  $\text{BaFe}_2(\text{As}_{0.7}\text{P}_{0.3})_2$  is approximately field independent. Note that the small

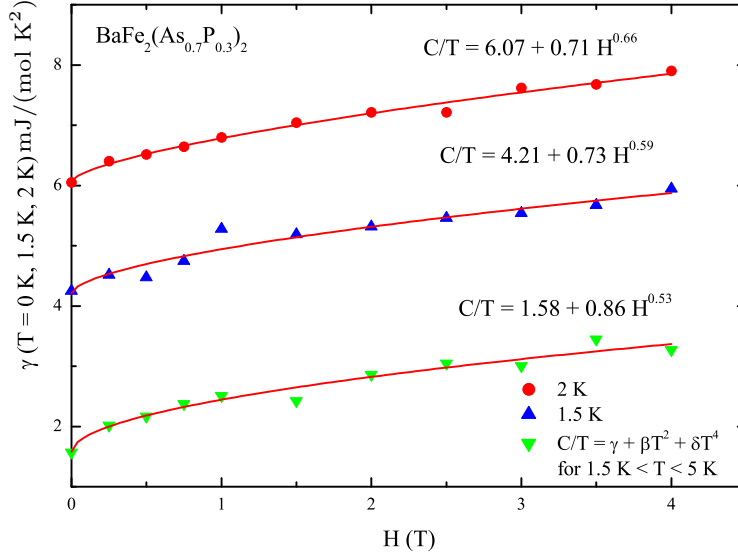


Figure 2-2. Low field  $\gamma$  data up to 4 T from Fig. 2-1 on an expanded scale for  $T = 2$  K (blue), 1.75 K (red) and 1.5 K (black symbols). Green symbols are asymptotic  $\lim_{T \rightarrow 0} C/T$  determined over the range  $1.5 \text{ K} < T < 5 \text{ K}$ . The fitting functions of the data are labeled beside the curves. Best power law fits to field dependence are shown in each case.

anomaly in the specific heat appears to vanish above 1.4 K, i.e., does not affect the estimate for  $\gamma$  shown in Figs. 2-1 and 2-2 using data from 1.5 K and above.

In order to have a closer look at the low field dependence of the specific heat, these data are shown on an expanded scale in Fig. 2-2. In our analysis below, we focus on the asymptotic  $T \rightarrow 0$  behavior since it is directly related to the density of states at the Fermi level, which is easy to calculate reliably, and since it gives essentially the same field dependence as the nonzero  $T$  data.

### 2.2.3 Two-Band Model

The Fermi surface of the optimally doped  $\text{BaFe}_2(\text{As}_{0.7}\text{P}_{0.3})_2$  consists of multiple Fermi surface sheets. DFT calculations showed that there are three concentric hole cylinders in the center of the Brillouin zone ( $\Gamma$  point) and two electron pockets at the zone corner ( $X$  point) [89]. Laser ARPES measurements [90] found a superconducting order parameter that is fully gapped with comparably sized gaps on each hole pocket of the order of  $\Delta_h/k_B T_c \sim 1.7$ . Taking into account the results from thermal

conductivity [81, 83] and NMR measurements [82] as well as the measurements of the specific heat coefficient in low fields presented above, that all consistently report evidence for low-energy quasiparticles, this ARPES result is consistent with a nodal gap on the electron pockets.

For numerical convenience, we adopt below a two-band model, distinguishing only between electron and hole pockets. Inclusion of all Fermi surface sheets then only enters as a weighting factor for the electron and hole pocket contributions, as we discuss in the following section. We take the gaps on the electron and hole pockets in the form  $\Delta_{1,2}(\theta) = \Delta_0^{e,h} \Phi_{1,2}(\theta)$ , where the angle  $\theta$  parameterizes the appropriate Fermi surface, assumed to be cylindrical. We assume an anisotropic gap on the electron pocket [91]  $\Phi_1(\theta) = (1 + r \cos 2\theta) / \sqrt{1 + r^2/2}$ , and an isotropic gap around the hole Fermi surface,  $\Phi_2(\theta) = 1$ . If the anisotropy factor  $r > 1$ , the superconducting gap in the electron band,  $\Delta_1(\theta)$ , has accidental nodes; if  $r = 0$ ,  $\Delta_1(\theta)$  is isotropic like  $\Delta_2(\theta)$ .

First we assume  $\Delta_0^e = \Delta_0^h$ , as is often found by ARPES. Since we consider well separated electron and hole bands, we can solve the Riccati equations, Eqs. (2–7), for the two propagators separately, and the only coupling of the pockets is via the self-consistency equations on the order parameter (see below). With this in mind we normalize the energy and length for the electron and hole bands by the gap amplitudes  $\Delta_0^e$  and  $\Delta_0^h$ , and the coherence lengths  $\xi_0^e = v_F^e / \Delta_0^e$  and  $\xi_0^h = v_F^h / \Delta_0^h$  respectively. Fermi velocities therefore appear as an input. DFT calculations for a comparable Ba-122 system [92] give  $v_F^h = 1.979 \times 10^5$  m/s and  $v_F^e = 3.023 \times 10^5$  m/s, i.e.,  $v_F^h / v_F^e = \xi_0^h / \xi_0^e = 0.65$ . In our analysis we keep this ratio but reduce the value of both Fermi velocities by a factor of 5 to approximately account for the mass renormalization of this system near optimal doping [80, 93]. This reduction also gives a roughly correct value of the  $c$ -axis upper critical field  $H_{c2} \sim 50$  T. In the limit of negligible coupling between the bands, the upper critical field  $H_{c2}$  is determined by the overlap of the

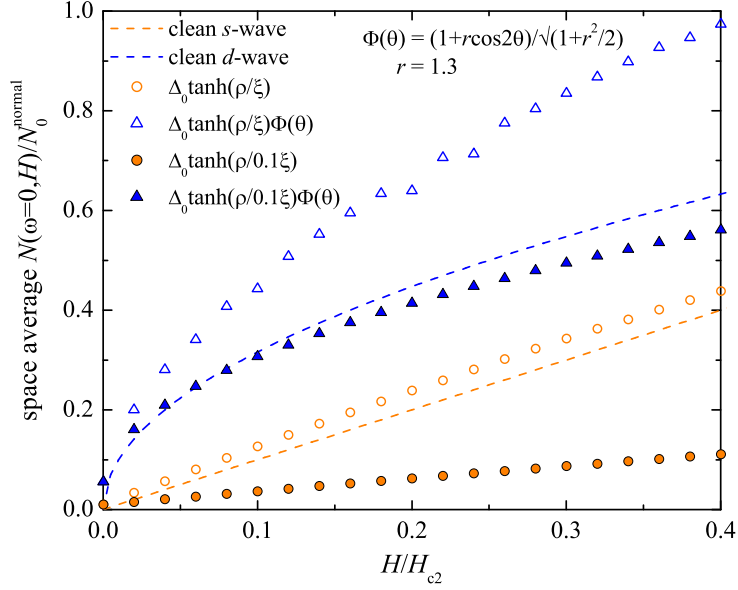


Figure 2-3. The spatially averaged zero energy density of states  $N(\omega = 0, H)$ , normalized to the normal state value  $N(\omega = 0)/N_0$  for a nodeless (orange) and a nodal (blue) single-band superconductor. The dashed lines show the idealized linear  $H$  and  $\sqrt{H}$  behavior for a clean  $s$ -wave and  $d$ -wave SC, respectively. The symbols are numerical results for a single band SC with an isotropic  $s$ -wave gap (circles) and a strongly anisotropic nodal gap (triangles). Additionally we compare results with (solid symbols) and without (open symbols) taking into account the vortex core reduction due to the Kramer-Pesch effect. Here we have ignored the field dependence of the superconducting gap, i.e.,  $\Delta(H) = \Delta_0$ .

vortices with smallest core size,

$$\frac{R}{\min\{\xi_0^e, \xi_0^h\}} = \frac{R}{\xi_0^h} = \sqrt{\frac{H_{c2}}{H}}, \quad (2-10)$$

where  $R$  is the single vortex radius under magnetic field  $H$ . Below we solve the Eilenberger equations and determine the density of states for an isolated vortex and for each band separately. In a two-band system the spatial profile of the quasiparticle states on the electron and hole bands is controlled by the respective coherence lengths, and therefore spatial averaging weighs the contributions of the bands differently compared to the DOS of a system with a single or two equal coherence lengths. This is the most significant difference compared to a single-band model.

The superconducting order parameters in the two bands are related by the interband component of the pairing interaction. We consider a general coupling matrix in the factorized form,  $\lambda_{\nu\mu}(\theta, \theta') = \lambda_{\nu\mu} \Phi_\nu(\theta) \Phi_\mu(\theta')$ , where  $\mu, \nu = 1, 2$  and  $\lambda_{\nu\mu} \equiv V_{\nu\mu} N_\mu$ . Here  $V_{11} = V_e$  and  $V_{22} = V_h$  are the intraband pairing interactions in the electron and the hole band, respectively, while  $V_{12} = V_{eh}$  is the interband interaction.  $N_\mu$  is the normal density of states at the Fermi level. Then the gap equation for an inhomogeneous superconductor is

$$\Delta_\nu(\mathbf{r}) = 2\pi T \sum_{\mu=1,2} \lambda_{\nu\mu} \sum_{\omega_n > 0}^{\omega_c} \langle \Phi_\mu(\theta) f_\mu(\mathbf{r}, \theta, i\omega_n) \rangle_\theta. \quad (2-11)$$

Here  $\Delta_\nu(\mathbf{r})$  is the momentum independent part of the gap function;  $\Delta_{1,2} = \Delta_0^{e,h}$  at  $T = 0$  and  $H = 0$ .

In the vortex state the self-consistent determination of the spatially dependent order parameter is a complex task. Since we are interested in relatively low fields, when the vortices are well separated, we solve the Eilenberger equations for the order parameter that is assumed to have a single vortex form,

$$\begin{aligned} \Delta^e(\vec{\rho}, H; \theta) &= \Delta_1(H) \tanh\left(\frac{\rho}{0.1\xi_0^e}\right) \frac{1 + r \cos 2\theta}{\sqrt{1 + r^2/2}}, \\ \Delta^h(\vec{\rho}, H) &= \Delta_2(H) \tanh\left(\frac{\rho}{0.1\xi_0^h}\right). \end{aligned} \quad (2-12)$$

Here  $\vec{\rho} = (\rho, \phi)$  is the two-dimensional projection of the radius vector in cylindrical coordinates, and a factor of 0.1 is introduced to approximate the shrinking of the core size in the self-consistent treatment at low temperatures (Kramer-Pesch effect [94, 95]). This single vortex ansatz provides a qualitatively correct description of the low-field state, close to what is found by full numerical solution [74]. To account for the suppression of the bulk order parameter by the magnetic field, we determine the coefficients  $\Delta_{1,2}(H)$  from the Brandt-Pesch-Tewordt approximation [96, 97], where in the presence of an Abrikosov lattice the diagonal components of the Green's function are

replaced by their averages over a vortex unit cell of the vortex lattice. This approximation has been proven to give reliable results over a considerable range of magnetic fields and is incorporated into our approach.

Note that our ansatz for the order parameter becomes quantitatively inaccurate for strong interband coupling in the regime of applicability of the Ginzburg-Landau theory since the core sizes of the two bands approach each other [98]. We verified in a fully self-consistent calculation that in the parameter range that we use, the corresponding effect on the specific heat is of order 1% or less and hence can be neglected. We therefore use Eq. (2-12) hereafter.

To proceed, we substitute Eq. (2-12) into the Riccati Eq. (2-7), solve for  $a(x)$  and  $b(x)$ , and use Eq. (2-9) to find the local density of states  $N(\vec{\rho}, H)$ . To approximate the specific heat coefficient, we evaluate the spatial average of the zero energy local density of states

$$\bar{N}(H) = \int_0^{2\pi} d\phi \int_0^R d\rho \rho \frac{N(\vec{\rho}, H)}{\pi R^2 N_0}, \quad (2-13)$$

where the intervortex distance  $R$  depends on  $H$  as described by Eq. (2-10). The total density of states is then given as

$$\bar{N}(H)_{\text{tot}} = \frac{w_e \bar{N}^e(H) + w_h \bar{N}^h(H)}{w_e + w_h}, \quad (2-14)$$

where  $w_e/w_h = 2N_0^e/N_0^h = 2\zeta$  if we consider, for example, two electron Fermi surface sheets in the folded Brillouin zone and denote  $\zeta \equiv N_0^e/N_0^h = v_F^h/v_F^e = 0.65 = \lambda_{21}/\lambda_{12}$ . The specific heat Sommerfeld coefficient  $\gamma(H)$  in the superconducting state is now obtained as  $\frac{\gamma(H) - \gamma_0}{\gamma_n - \gamma_0} = \bar{N}(H)_{\text{tot}}$ , where  $\gamma_n$  and  $\gamma_0$  are two constants from the experiment. Since the vortex density is controlled by the external field, integration up to the intervortex spacing  $R \sim \sqrt{\Phi_0/H}$  correctly accounts for the field effect within the single vortex approximation. The integration thus includes not only the contribution of extended quasiparticle states to the specific heat, but also the localized quasiparticles in the core.

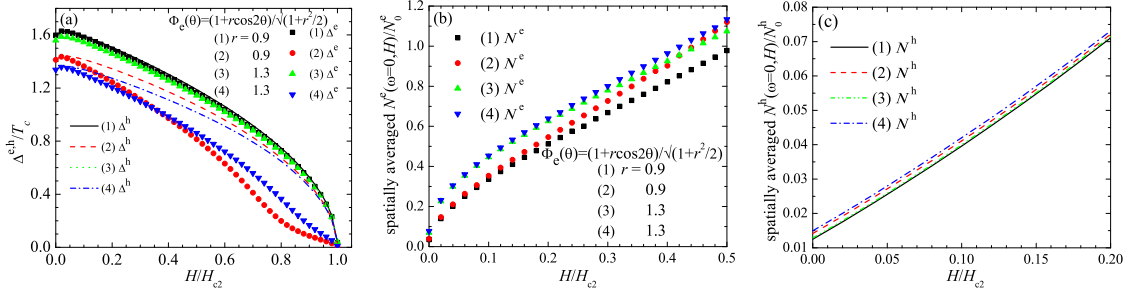


Figure 2-4. Results of quasiclassical calculations for the parameters in Table 2-1. (a) Magnetic field dependence of the gaps in the two-band model calculated within the Pesch approximation (Refs. [96, 97, 99]) for Case 1–4. We assume  $\Delta^e(H = 0) = \Delta^h(H = 0)$  here. The four sets of coupling constants  $\lambda_{ij}$  are listed in Table 2-1. (b) Field dependence of the space average ZDOS  $N^e(H)$  on the electron pocket for the four cases with anisotropic gap with angular variation  $\Phi_e(\theta) = (1 + r \cos 2\theta) / \sqrt{1 + r^2/2}$ . (c) Field dependence of the space average ZDOS  $N^h(H)$  for the four cases with isotropic gap along the hole pocket.

## 2.2.4 Results

To illustrate that the salient features of the vortex state DOS are captured in our approach, in Fig. 2-3 we show the field dependence of the spatially averaged zero energy local density of states (ZDOS) for a one-band SC with either an isotropic  $s$ -wave gap or a strongly anisotropic nodal gap ( $r = 1.3$ ). Note that, while the field dependences in both the nodal and fully gapped cases clearly fit the anticipated power laws at low fields,  $\sqrt{H}$  and  $H$ , respectively, there is a significant influence on the magnitude of the DOS caused by the size of the core, with the smaller core size yielding smaller ZDOS. In particular, in the absence of the Kramer-Pesch effect, for the nodal case the ZDOS would exceed the normal state value at fields far below  $H_{c2}$ , which is unphysical.

Below we consider  $r = 0.9$  and  $r = 1.3$  to mimic a gap with deep minima and accidental nodes, respectively. To show different types of behavior allowed within our microscopic model we chose four sets of coupling constants, two for each value of  $r$ , as shown in Table 2-1. In Cases 1 and 3, the interband pairing  $\lambda_{12}$  is strong and close to the intraband parameter  $\lambda_{11}$ , while in Cases 2 and 4,  $\lambda_{12} \ll \lambda_{11}, \lambda_{22}$ .

Table 2-1. The different models for the coupling matrix and the gap anisotropy on the electron pockets considered in this work.

|        | $\lambda_{11}$ | $\lambda_{12}$ | $\lambda_{21}$ | $\lambda_{22}$ | $r$ | $T_c/\text{K}$ | $H_{c2}/\text{T}$ |
|--------|----------------|----------------|----------------|----------------|-----|----------------|-------------------|
| case 1 | 0.51           | 0.51           | 0.33           | 0.65           | 0.9 | 31             | 54                |
| case 2 | 1.00           | 0.02           | 0.013          | 0.81           | 0.9 | 31             | 47                |
| case 3 | 0.51           | 0.51           | 0.34           | 0.64           | 1.3 | 31             | 54                |
| case 4 | 1.00           | 0.023          | 0.015          | 0.77           | 1.3 | 31             | 42                |

In Fig. 2-4(a) we show the self-consistently determined magnitudes of the bulk gaps in the vortex state  $\Delta_{1,2}(H)$  as defined in Eq. (2-11) and (2-12).  $H_{c2} \sim 40\text{--}50$  T. In the cases with only weak interband pairing, Cases 2 and 4, the gap on the electron Fermi surface deviates considerably from the phenomenological form  $\Delta(H) = \Delta_0 \sqrt{1 - H/H_{c2}}$ . Figs. 2-4(b) and (c) show the spatially averaged ZDOS corresponding to each band. For  $N^e(H)$  and for  $r = 1.3$  the  $\sqrt{H}$  behavior of the Volovik effect is clearly visible at lower fields up to  $H/H_{c2} = 0.2$ . Comparing Fig. 2-4(b) to Fig. 2-3 we find that within the two-band model the density of states of the electron band  $N^e(H)$  reaches a quasi-linear behavior already at smaller fields than the corresponding density of states for the one-band case. In Fig. 2-3 a linear behavior is never observed, and might only be fit over some intermediate field range for  $H/H_{c2} > 0.2$ , while in the multiband case  $N^e(H)$  displays a clear linear behavior already for  $H/H_{c2} > 0.1$ .

It is tempting to interpret the low-field crossover to a quasilinear field variation as evidence for a small energy scale  $\Delta_{sm} \equiv \Delta_0^e(1 - r)/\sqrt{1 + r^2/2}$  on the electron band; this, however, seems unlikely. Provided  $\Delta_{sm} \ll \Delta_0^e$ , the gap still increases linearly along the Fermi surface away from the nodal points above this energy scale, simply with a different slope. Then within the usual Volovik argumentation the contributions from extended states at these intermediate energies give rise to a  $\sqrt{H}$  contribution even if  $\Delta_{sm} \lesssim E_H \ll \Delta_{max}$ , where  $E_H \propto \sqrt{H}$  is the average Doppler shift and  $\Delta_{max} \equiv \Delta_0^e(1 + r)/\sqrt{1 + r^2/2}$  is the maximum gap. There is therefore no true linear- $H$  behavior arising from the electron band with gap nodes. Consequently, we interpret this crossover as the consequence of

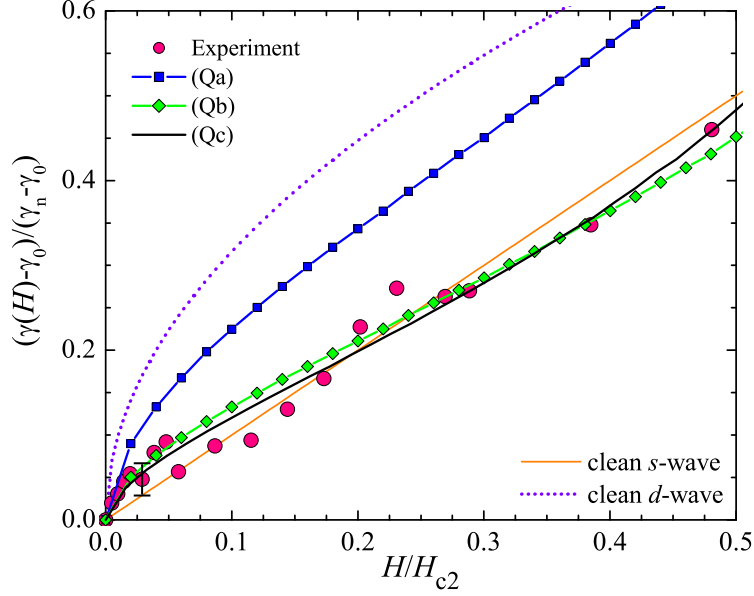


Figure 2-5. Comparison of the experimentally measured normalized specific heat coefficient (large pink dots, adapted from Fig. 2-1) to different theoretical results for the spatially averaged ZDOS. The dotted violet and solid orange curves are the predictions for the spatially averaged ZDOS for a clean  $s$ -wave and  $d$ -wave SC. The blue squares (Case Qa) and green diamonds (Case Qb) are the differently weighted sums of  $\bar{N}^e(H)$  and  $\bar{N}^h(H)$  evaluated for case (4) of Figs. 2-4(b) and (c). The black line (Case Qc) is obtained using the formula  $\gamma^{\text{tot}} = a_1 \bar{N}_e(H) + a_2 \bar{N}_h(H)$  where  $a_1 = 3.2 \text{ mJ}/(\text{mole K}^2)$ ,  $a_2 = 10.3 \text{ mJ}/(\text{mole K}^2)$  are determined with the least square fit to experimental data below 30 T. Note “ $d$ -wave” and “ $s$ -wave” curves represent simple extrapolations of the low-field  $\sqrt{H}$  and  $H$  terms up to  $H_{c2}$ . The error bar shown corresponds to the absolute accuracy of the data discussed above in Fig. 2-1.

the two-band behavior coupled with a gradually increasing contribution of core states which is nearly linear in field. Fig. 2-4(c) clearly shows that the density of states of the hole band  $N^h(H)$ , assumed here to be fully gapped, is always linear as a function of field and the results for the two different coupling matrices considered here are very similar. However, as mentioned before, the slope is smaller than the one predicted for an idealized  $s$ -wave SC.

Using Eq. (2-14), the spatially averaged ZDOS on the electron and the hole band are added with different weights. Using the results presented in Figs. 2-4(b) and (c) as Case 4, we investigate several scenarios. Since there are two electron pockets, and

assuming that only one hole pocket contributes significantly to the low energy density of states (or that a naive average over the hole pockets is sufficient), the net DOS and the field dependence of the Sommerfeld coefficient are only functions of the ratio of the densities of states of the electron and hole sheets. In the following we will study three scenarios derived from Case 4, which we will abbreviate with “Q” indicating the use of the quasiclassical, or Eilenberger, approach:

- Case Qa: we assume that only one hole pocket contributes considerably to the low energy DOS, and use the weights  $w_e/w_h = 2N_0^e/N_0^h$  taken from the DFT calculation,  $N_0^e/N_0^h = 0.65$ , see Ref. [92];
- Case Qb: We once again fix  $N_0^e/N_0^h = 0.65$ , but adopt a model for which the normal DOS for all three hole pockets of  $\text{Ba}_2\text{Fe}_2(\text{As}_{0.7}\text{P}_{0.3})_2$  are the same and for which all three pockets contribute equally to the low energy DOS, hence  $w_e/w_h = 2N_0^e/3N_0^h$ ;
- Case Qc: We do not hold the ratio  $N_0^e/N_0^h$  fixed, but instead calculate the weights for the electron pockets  $a_1$  and for the hole pockets  $a_2$  by a least squares fit to the experimental data using the formula  $\gamma^{\text{tot}} = a_1\bar{N}_e(H) + a_2\bar{N}_h(H)$ . If we normalize it to the presumed contribution of the superconducting fraction,  $\gamma_n - \gamma_0 \approx 14 \text{ mJ}/(\text{mole K}^2)$ , where  $\gamma_0$  is the extraneous term (see below), we find  $w_e/(w_e + w_h) = a_1/(\gamma_n - \gamma_0)$  and  $w_h/(w_e + w_h) = a_2/(\gamma_n - \gamma_0)$  and  $a_1/a_2 = w_e/w_h$ .

In Fig. 2-5 we compare the results for all three cases to the experimentally measured specific heat coefficient (pink dots). The experimental values are obtained by extrapolating the measured specific heat coefficient  $\gamma$  at various temperatures to  $T = 0$ . The upper critical field  $H_{c2}$  is taken to be 52 T, see Ref. [83]. The normal state  $\gamma_n = 16 \text{ mJ}/(\text{mole K}^2)$  can be obtained by extrapolating  $\gamma$  to  $H_{c2}$ . A substantial residual [84]  $\gamma_0 = 1.7 \text{ mJ}/(\text{mole K}^2)$  in the superconducting state, presumed due to disorder, is subtracted in the plots of the field dependence from the experimental data (pink dots) to compare with our quasiclassical calculation in the clean limit (blue squares and green diamonds). Note that subtracting of the residual  $C/T$  tends to enhance the scatter in the low-T data of Fig. 2-2.

From Fig. 2-5, we see that the results derived for model Qb with three equal mass hole pockets and two equal mass electron pockets are in good agreement with the

experimental data: both experiment and theory show a “Volovik effect” at the lowest fields and then a crossover to a linear  $H$  dependence at intermediate fields. While model Qa has the same qualitative behavior, the relative weights of hole and electron bands are apparently not consistent with the normalized experimental data, and the fit is much poorer. Compared to Qb, the least squares fit Qc to the experimental data (black line) is only marginally improved, and gives the ratio  $N_0^e/N_0^h = 0.47$  with two electron pockets/three hole pockets or 0.16 with two electron pockets/one hole pocket, the same order as obtained from DFT calculation.

As is usually the case with the measurements that probe the amplitude rather than the phase of the gap, it is difficult to distinguish the deep minima from the true nodes. In this case we find that with our current uncertainty in the band parameters, and the scatter in the data, it is impossible to assert the nodal behavior purely from the current data. Fig. 2-6 shows the comparison of Cases 1 and 4 of Table 2-1, corresponding to  $r = 1.3$  and 0.9, i.e., with and without true nodes, with the weights of Case Qb. Even though the nodal fit appears better at the lowest fields, higher  $H$  data are in between the two cases. Therefore the conclusion about the true node comes from the data on other experiments, such as penetration depth.

### 2.2.5 Conclusions

Among the various families of Fe-based superconductors,  $\text{BaFe}_2(\text{As}_{1-x}\text{P}_x)_2$  may be a key system for understanding the origins of superconductivity. In part this is because, alone among the materials thought to display nodes in the superconducting gap, it possesses a rather high  $T_c$  of 31 K, and hence the interplay of the pairing mechanism and Fermi surface shape and parameters in determining the gap anisotropy is under special scrutiny. The lack of an observable Volovik effect in earlier specific heat measurements was a cautionary note in an otherwise consistent array of measurements in support of gap nodes. We have presented experimental data at both lower and higher fields than previous measurements, and found that the initially reported linear- $H$

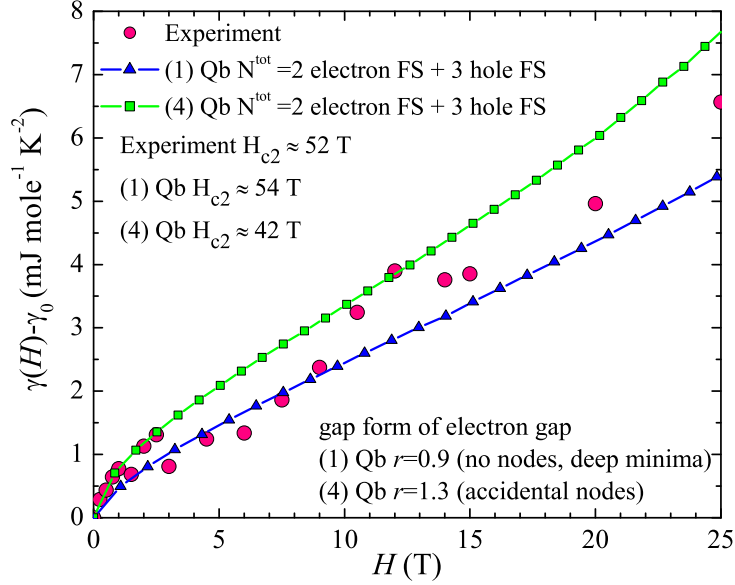


Figure 2-6. Experimentally measured specific heat coefficient (large pink dots, adapted from Fig. 2-1) compared to calculations with deep gap minima (Case 1,  $r = 0.9$ , blue triangles) and accidental nodes (Case 4,  $r = 1.3$ , green squares). In both cases the weight of electron and hole pocket contributions has been chosen in agreement with Case Qb.

behavior extends up to 35 T, but that at low fields ( $H \lesssim 4$  T) more precise measurements with smaller gradations in the change of field between data points are now clearly consistent with a Volovik-type effect. The residual  $T \rightarrow 0$  Sommerfeld coefficient  $\gamma(T \rightarrow 0)$  is about  $1.7 \text{ mJ}/(\text{mole K}^2)$ , consistent with possible nanoscale disorder in the sample. The low-field sublinear dependence of the Sommerfeld coefficient is a strong indication that nodes (or deep minima) are present, and provides the sought-after consistency with other probes without having to make extreme assumptions about the ratio of masses on electron pockets to those on hole pockets, as was proposed in Ref. [84].

It is nevertheless striking that indications of nodal behavior on the same samples is so much weaker in the specific heat measurements as compared to thermal conductivity and penetration depth. This is clearly indicating that the nodes are located on the pockets with smaller masses and/or longer lifetimes, as was pointed out in Ref. [84].

We have attempted to put this statement on a semiquantitative basis by presenting a quasiclassical (Eilenberger) calculation of the density of states and specific heat of a two-band anisotropic  $s_{\pm}$  superconductor. Comparison with the Doppler shift method allowed us to argue that the quasiclassical calculation is superior for semiquantitative purposes. We find that the unusually small range of Volovik-type behavior, followed by a large range of linear- $H$  behavior, is due to the small gap and weak nodes on the small mass (presumably electron) sheet [83, 84]. Good fits to the data are obtained for average hole and electron maximum gaps of approximately equal magnitude, in the weak interband coupling limit. The success of this fit should not, however, tempt one to draw definitive conclusions about the relative magnitudes of the pairing interactions. The proliferation of parameters in the theory due to the multiband nature of the system makes it difficult to determine gap magnitudes, density of states ratios, and nodal properties with any quantitative certainty. Equally good fits can be obtained, for example, with substantially smaller full gaps than anisotropic gaps; the nodes control the low-field behavior, and the small full gap gives rise to a large linear term. What is important is that we have shown that a fit can be obtained, with reasonable values of the parameters, that it can only be obtained if nodes (or deep minima) exist on one of the Fermi sheets, and that it requires going beyond the simple Doppler shift picture. It is our hope that the results of this calculation and fit will eventually lead to a more quantitative first-principles-based calculation.

## **2.3 Quasiparticle Vortex Bound States in FeBS: Application to LiFeAs**

### **2.3.1 Motivation**

Bulk experiments such as specific heat and thermal conductivity oscillations in an external magnetic field [100, 101] can also probe the orientations of gap nodes if they exist. Performed on the Fe(Te,Se) system [102] and P-doped 122 family [83] respectively, these experiments reported oscillation patterns consistent [83, 101, 103,

[104] with an anisotropic gap with minima along the  $\Gamma-X$  axis (in the unfolded Brillouin zone), as predicted by spin fluctuation theories (see, e.g., Ref. [8]).

Order parameter structure is also reflected in the local properties of inhomogeneous superconducting states. Inhomogeneities may arise due to impurities, and the resulting quasi-bound states in nodal superconductors have tails that “leak out” in the nodal directions [105], providing a signature of the amplitude modulation of the gap. The interpretation of these impurity states is complex: disorder potentials can be of the order of electron volts, and hence relatively high energy processes control the formation of such states, as well as their contribution to scanning tunneling spectroscopy (STS) images [106].

Under an applied magnetic field, inhomogeneous superconductivity also arises due to modulation of the order parameter in a vortex lattice, and bound states localized around the vortex cores appear. In this case, relevant energy scales are of the order of the gap or lower and the bound states properties are determined by the shape of the gap and the band features near the Fermi surface. The decay length of the core states is of order of  $\xi_{\text{BCS}} = v_F/\pi\Delta$ , where  $v_F$  is the Fermi velocity and  $\Delta$  is the gap amplitude. Consequently, variation of the gap with direction  $\hat{\mathbf{k}}$  at the FS,  $\Delta(\hat{\mathbf{k}}) \neq \text{const}$ , directly influences the shape of the core states in real space, leading to the “tails” extending along nodes or minima. Since the decay of these states is exponential in distance  $\rho$  from the center of the vortex (except along true nodes where it follows power laws in which case there exist no truly localized bound states [107]), these tails should be seen in local measurements, for instance, the conductance map by STS, and can be used to probe the gap shape such as the fourfold symmetric  $d_{x^2-y^2}$ -wave gap in cuprates. Theoretical calculations using Eilenberger formalism clearly showed these tails in the local density of states near the vortex core in a  $d$ -wave superconductor [67, 68] but the STS on the vortex core of  $\text{YBa}_2\text{Cu}_3\text{O}_{7-\delta}$  [108] and  $\text{Bi}_2\text{Sr}_2\text{CaCu}_2\text{O}_{8-\delta}$  [109] could only suggest the fourfold symmetry of the gap (see Fig. 2-7). Although difficulties of interpretation exist

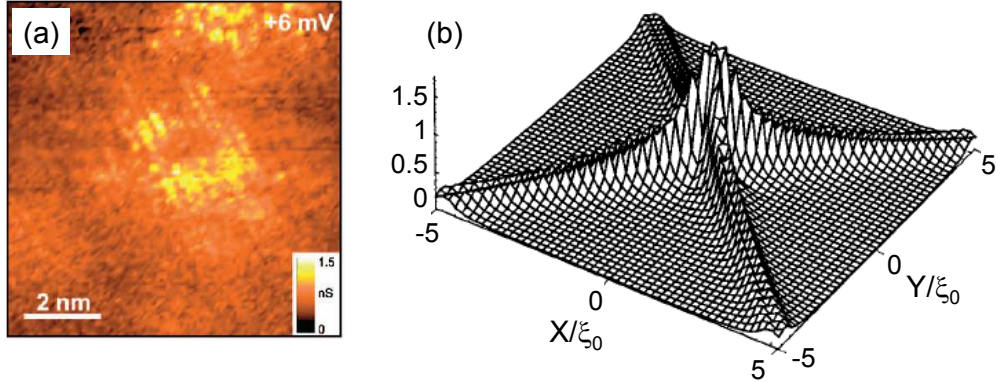


Figure 2-7. (a) Conductance map of a vortex core of  $\text{Bi}_2\text{Sr}_2\text{CaCu}_2\text{O}_{8-\delta}$  at 6 mV revealing a square pattern around the vortex center (reprinted with permission from [109], copyright 2005 by the American Physical Society). (b) Zero energy local density of states showing tails along  $y = \pm x$  directions for a  $d_{x^2-y^2}$ -wave gap (reprinted with permission from [67], copyright 1996 by the American Physical Society).

in cuprates [110], where the coherence length is short and the cores may nucleate competing order (see, e.g., Ref. [111]), in most Fe-based superconductors (FeBS) these complications are less severe or absent over a wide range of experimentally tunable parameters.

On the other hand, a complex aspect of FeBS arises due to their multiband nature. The directional dependence  $\mathbf{v}_F(\hat{\mathbf{k}})$  also affects the decay length of the core states, especially when combined with different gap amplitudes on different Fermi surface sheets. In FeBS, the Fermi surface typically consists of two or three hole pockets and two electron pockets, as represented in the Brillouin zone corresponding to one-Fe unit cell (see Fig. 2-8). The size and shape of these pockets varies considerably from family to family. A natural question is whether it is the normal state band structure and the Fermi surface, or the order parameter shape that determine the salient features of the vortex core states as seen in experiment, and whether one can draw reliable conclusions about the directions of the gap nodes or minima based on the real space structure of these states. We will address this question below in this chapter.

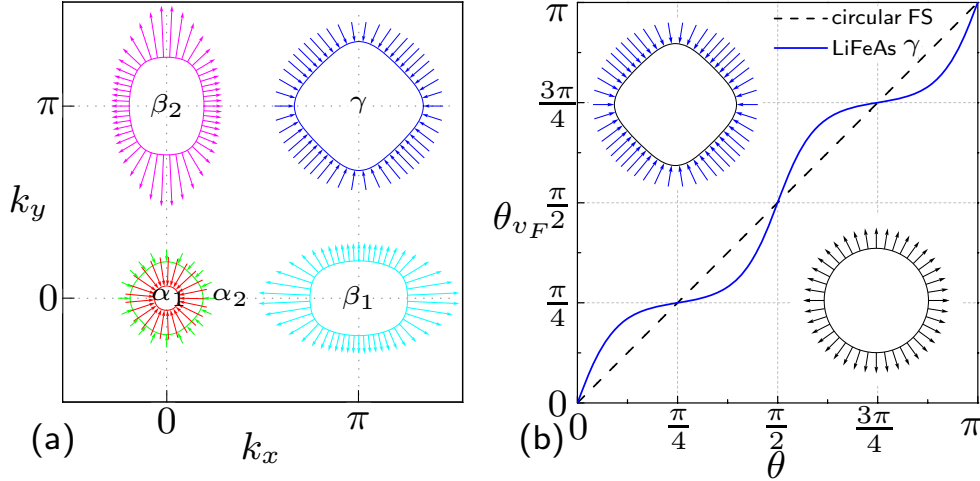


Figure 2-8. (a) Fermi surface of stoichiometric LiFeAs at  $k_z = 0$  in the unfolded one-Fe “effective” Brillouin zone from DFT. The Fermi velocities for different sheets are indicated by the arrows pointing to the higher  $E(\mathbf{k})$ . We label two inner hole pockets  $\alpha_1, \alpha_2$ , one outer hole pocket  $\gamma$  and two electron pockets  $\beta_1, \beta_2$ . (b) The Fermi velocity direction  $\theta_{v_F}$  vs the momentum  $\mathbf{k}$  azimuthal angle  $\theta$  for the LiFeAs  $\gamma$  pocket and the circular Fermi surface (shown as insets).

The competition between the two effects has been explored numerically in other contexts. For example, the sixfold pattern observed in 2H-NbSe<sub>2</sub> core states [112] can be explained either assuming a weak gap anisotropy or using the angle-dependent density of states around the Fermi surface [113]. In pnictides, it was argued both that the vortex core states are controlled by the order parameter shape [114], and that the location of the peak in the DOS is determined by the proximity to the band edge in the electron or hole bands [115]. To gain qualitative insight into this issue, we consider a simple model with both the order parameter and band anisotropy characteristic of the Fe-based superconductors, and find that in the absence of strong nodes the Fermi velocity anisotropy can dominate the real-space shape of the vortex core states. These states were observed in early STS experiments [116, 117], albeit without the spatial resolution necessary to analyze the order parameter structure.

We focus on the LiFeAs system, which is ideal for STS measurements due to its nonpolar surfaces. According to calculations [118] using density functional

theory (DFT), the Fermi surface of this material has three hole pockets and two electron pockets (see Fig. 2-8). The outer hole pocket is large and quite square, according to both DFT results and ARPES [119] and de Haas-van Alphen (dHvA) [120] measurements. Both  $\gamma$  and  $\alpha_2$  hole pockets have small Fermi velocities and therefore large normal state DOS. ARPES has identified superconducting leading edge gaps of order 1.5–2 meV for the hole pockets, and 3 meV for the electron pockets [119]. The London penetration depth data [121] and specific heat measurements [122] ruled out the existence of gap nodes and were fit to models with two isotropic gaps with  $(\Delta_1, \Delta_2) \simeq (3 \text{ meV}, 1.5 \text{ meV})$  and  $(2 \text{ meV}, 0.5 \text{ meV})$ , respectively. This suggests moderate gap anisotropy, which is not easily detected by the bulk measurements, but can substantially affect the real space structure of the core states. Borisenko *et al.* [123] indeed found substantial gap anisotropy around both electron and hole Fermi surfaces in angle-resolved photoemission (ARPES) experiment. Umezawa *et al.* reported similar but not quantitatively identical results for anisotropic gaps [124]. Spin-fluctuation theory [125] predicts similar gap anisotropy as these ARPES experiments. In Fig. 2-9(a) we sketch the experimental data in Ref. [123]. Since the gap on  $\gamma$  Fermi pocket with a relatively large density of states is the smallest and ARPES [123, 124] and STM [126] suggest that the minimum of the  $\gamma$  gap is along Fe-Fe direction, one would expect that the tails of low energy quasiparticles extend in this direction (the  $k_x, k_y$  directions in Fig. 2-8). On the contrary, these tails around a single vortex measured in zero energy conductance map with STS [127] are actually along As-As direction (the  $k_x = \pm k_y$  directions in Fig. 2-8); see Fig. 2-9(b).

For circular Fermi surfaces the low-energy core bound states extend furthest in the direction of the smallest gap, but for realistic bands the Fermi velocity anisotropy plays a significant role. Since the cross-sections of the  $\beta_1$  and  $\beta_2$  electron pockets rotate by a full  $180^\circ$  along the  $k_z$  direction, and since these gaps are larger, it is unlikely that these sheets contribute substantially to the spatial anisotropy. We therefore focus on the

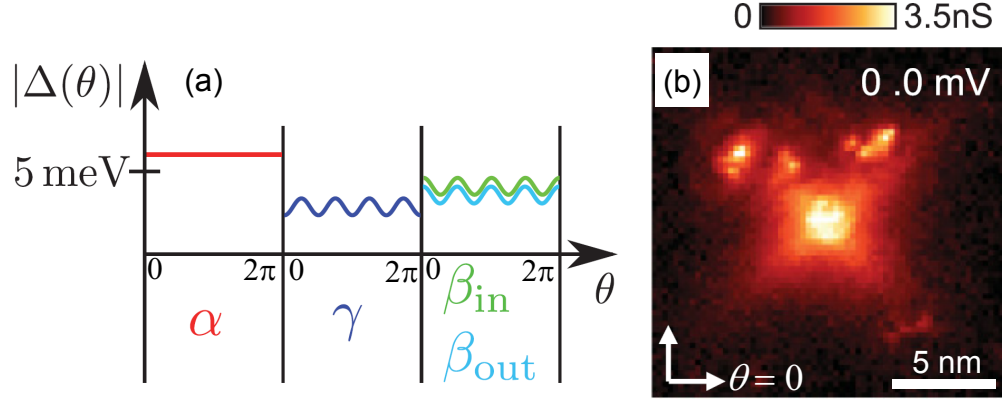


Figure 2-9. (a) Sketch of ARPES measured gaps of LiFeAs on electron and hole pockets [123]. (b) Zero energy STS conductance map around a single vortex of LiFeAs (reprinted with permission from [127], copyright 2012 by the American Physical Society).

possible anisotropy of the gap on the hole Fermi surfaces. The most likely candidate for the anisotropic gap that dominates the low-energy vortex bound states is the  $\gamma$  pocket. The orbital content of this pocket is exclusively  $d_{xy}$ , and it couples only weakly to the primarily  $d_{xz}$  and  $d_{yz}$  electron pockets which provide the main pairing weight in the conventional spin fluctuation approach [8]. It is also nearly square, with weakly dispersive parallel surfaces oriented along the [110] direction in the one-Fe zone, and with significant variations of the Fermi velocity between [100] and [110] directions. Hence we first neglect other Fermi surface sheets, and contrast the results obtained for the  $\gamma$  sheet alone with those for a single circular Fermi surface.

### 2.3.2 Model

We follow the the quasiclassical method introduced in Sec. 2.1. Specifically, in the Eilenberger Eqs. (2-1) the Fermi velocity,  $\mathbf{v}_F(\theta)$ , is along the 2D unit vector  $\hat{\mathbf{k}}$  for the circular Fermi surface, and is computed for the  $\gamma$ -band in LiFeAs using the Quantum ESPRESSO [128], as in Ref. [129]. In the low field regime, we consider the problem of an isolated vortex and assume a separable momentum and coordinate dependence of the order parameter  $\Delta(\rho, \hat{\mathbf{k}}) = \Delta_0 \Phi(\theta) \tanh(\rho/\eta_r \xi_0)$ , where  $\Delta_0$  is the bulk gap value in the absence of the field and  $\Phi(\theta)$  describes the gap shape on the Fermi surface,

$\Phi_s = 1$ ,  $\Phi_d = \sqrt{2} \cos 2\theta$ , and  $\Phi_{s,\text{ani}} = (1 - r \cos 4\theta) / \sqrt{1 + r^2/2}$  with  $r = 0.3$ , for the isotropic  $s$ -wave, nodal  $d$ -wave, and extended  $s$ -wave gaps respectively [130, 131]. The coherence length is  $\xi_0 = \hbar v_{F,\text{rms}} / \Delta_0$  where  $v_{F,\text{rms}} = \sqrt{\langle |\mathbf{v}_F(\hat{\mathbf{k}})|^2 \rangle_{\text{FS}}}$ , and the brackets denote the normalized average over the Fermi surface,

$$\langle \cdots \rangle_{\text{FS}} = \frac{1}{\mathcal{N}} \oint_{\text{FS}} \frac{dk_{\parallel}}{|\mathbf{v}_F(\hat{\mathbf{k}})|} \cdots = \int_0^{2\pi} \frac{d\theta}{2\pi} \tilde{\rho}(\theta) \cdots, \quad (2-15)$$

where  $\mathcal{N} \equiv \oint_{\text{FS}} \frac{dk_{\parallel}}{|\mathbf{v}_F(\hat{\mathbf{k}})|}$  and  $\tilde{\rho}(\theta)$  is the angle-dependent density of states. The factor  $\eta_r$  accounts for the shrinking of core size at low temperature (Kramer-Pesch effect [94, 95]), and we set  $\eta_r = 0.1$  corresponding to  $T \sim 0.1 T_c$ . In a fully self-consistent calculation, the gap anisotropy in momentum space will induce weak core anisotropy in real space [67], which we ignore here since the effect is small even for nodal systems [67].

We solve Eq. (2-1) using the Riccati parametrization [74] and integrating along classical trajectories,  $\mathbf{r}(x) = \mathbf{r}_0 + x \hat{\mathbf{v}}_F$  to obtain the functions  $g$  and  $f$  at Matsubara frequencies. The LDOS is found after analytic continuation from retarded propagators,  $N(\mathbf{r}, \omega) = N_0 \langle \text{Re } g^R(\mathbf{k}_F, \mathbf{r}, \omega + i\delta) \rangle_{\text{FS}}$ . At each point  $\mathbf{r} = (\rho, \phi)$  the LDOS is obtained by summation over the quasiclassical trajectories passing through  $\mathbf{r}$ . Each trajectory follows the direction of the Fermi velocity at a given point on the FS,  $\hat{\mathbf{v}}_F(\hat{\mathbf{k}})$ , and samples the gap  $\Delta(\mathbf{r}(x), \hat{\mathbf{k}})$ . Trajectories sampling regions of small order parameter contribute to the low energy LDOS. This occurs if the trajectory either passes in the vicinity of the core where the order parameter is suppressed in real space,  $\Delta(\rho) \ll \Delta_0$  (small impact parameter, dominant for isotropic gaps), or is along the direction where the gap has a node or a deep minimum in momentum space,  $\Delta(\hat{\mathbf{k}}) \ll \Delta_0$  (dominant for nodal superconductivity).

The influence of the FS shape is then clear: the number of trajectories with a given impact parameter depends on the band structure. Denote the angle between  $\hat{\mathbf{v}}_F$  and  $k_x$  axis as  $\theta_{v_F}$ . For a circular FS,  $\theta_{v_F} = \theta$ , and quasiclassical trajectories in different directions  $\theta_{v_F}$  are equally weighted in FS averaging. In contrast, for anisotropic cases,

such as the square  $\gamma$ -sheet in LiFeAs, large parts of the FS have the  $\mathbf{v}_F$  along the diagonals (see Fig. 2-8b), and therefore the average over the trajectories is heavily weighted towards that direction as well.

For an isotropic gap  $\Delta(\hat{\mathbf{k}}) = \text{const}$ , the largest contribution to the low energy LDOS at  $\mathbf{r} = (\rho, \phi)$  comes from the trajectories passing through the core,  $\theta_{v_F} = \phi$  or  $\phi + \pi$ . For a cylindrical FS parameterized by angle  $\theta$  this corresponds to two points since  $\theta_{v_F} = \theta$ . On an anisotropic FS, such as the  $\gamma$  pocket in LiFeAs, many different momentum angles  $\theta$  correspond to  $\theta_{v_F} \approx \pm \frac{\pi}{4}$ , and quasiparticles from a large portion of the FS travel along these directions. For real space direction  $\phi = \frac{\pi}{4}$ , all these trajectories sample the core region and contribute to the low energy LDOS. For  $\phi$  away from these directions these trajectories have a nonzero impact parameter and therefore small weight at low energies. For the extended  $s$ -wave gap model with  $r > 0$  in the form factor  $\Phi_{s,\text{ani}}$ , this implies that the regions of large gap will be emphasized due to preferential directions of  $\mathbf{v}_F$ , and therefore the FS effects compete with the gap shape in determining the spatial profile of the vortex core states. Simply assuming that the direction of the smallest gap in  $\mathbf{k}$  space yields the orientation of the tails of the bound state wave function need not be correct, and may be wrong with a strongly anisotropic Fermi surface.<sup>2</sup>

### 2.3.3 Results

Fig. 2-10 shows the zero energy density of states (ZDOS) of a circular Fermi surface [Figs. 2-10(a)–2-10(c)] and LiFeAs  $\gamma$  pocket [Figs. 2-10(d)–2-10(f)]. Comparing Figs. 2-10(a) and 2-10(d) for the isotropic gap, we see that the rotation symmetry of ZDOS in Fig. 2-10(a) is broken due to the anisotropy of  $\gamma$  pocket and Fermi velocity; at the same time the ZDOS still preserves the crystal four-fold symmetry. In the  $d$ -wave

---

<sup>2</sup> For a  $d$ -wave gap along a circular Fermi surface, near the nodal directions  $\theta \approx \frac{\pi}{4}$ , the energy spectrum is not strongly restricted to zero impact parameter. As long as  $\theta = \theta_{v_F} \approx \frac{\pi}{4}$ , the LDOS is enhanced and therefore this case has wider tails along directions  $\phi \approx \frac{\pi}{4}$ .

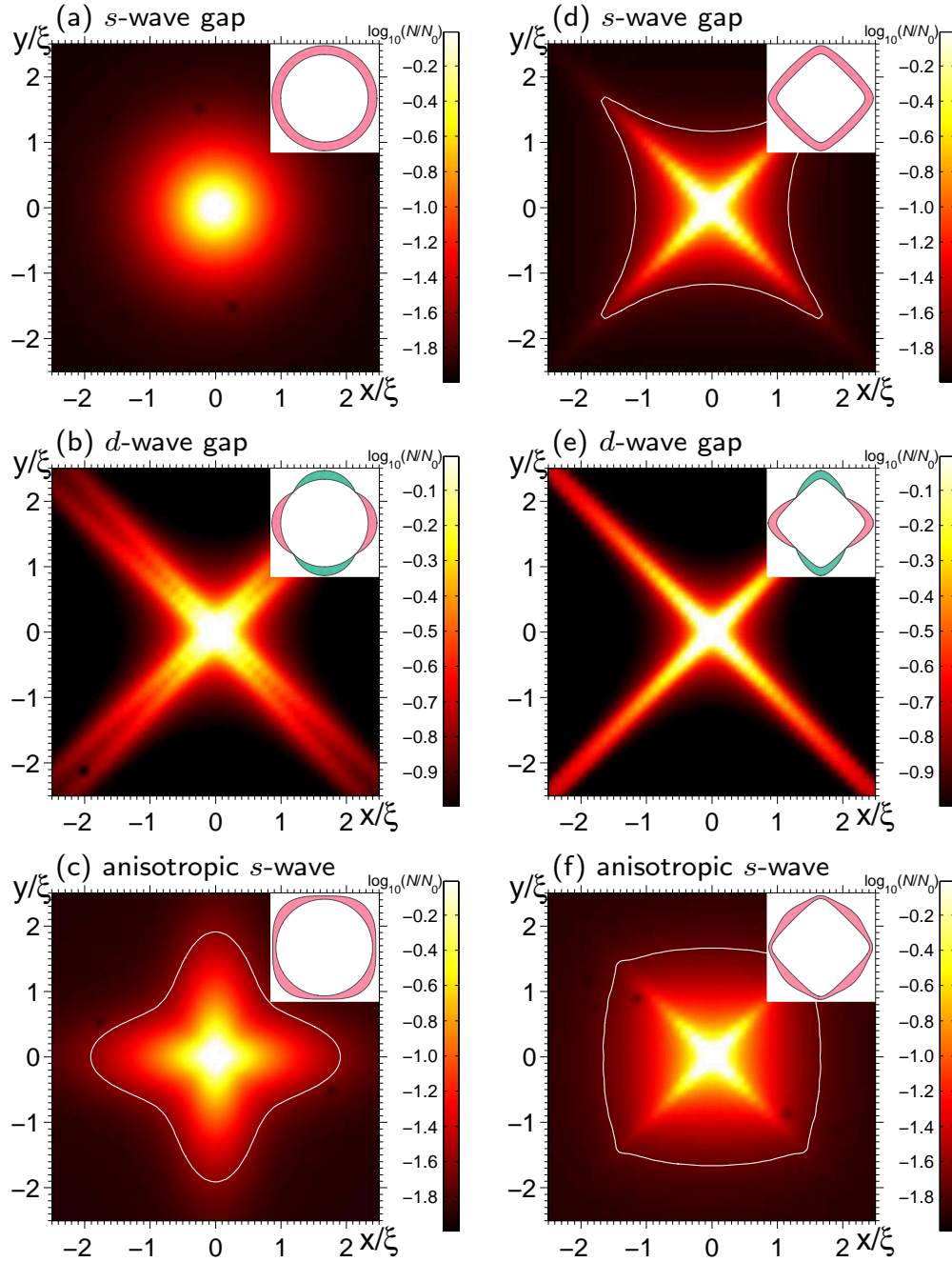


Figure 2-10. Normalized ZDOS in a  $2.5\xi_0 \times 2.5\xi_0$  region around the center of the single vortex for different gap models with a circular Fermi surface (a)–(c) and LiFeAs  $\gamma$  pocket (d)–(f): (a), (d) an isotropic *s*-wave gap  $\Delta_0$ ; (b), (e) a nodal *d*-wave gap  $\Delta_0\sqrt{2}\cos 2\theta$ ; (c), (f) extended *s*-wave gap  $\Delta_0(1 - r\cos 4\theta)/\sqrt{1 + r^2/2}$ ,  $r = 0.3$ . The gap bulk value is taken to be  $\Delta_0 = 1.76T_c$ . The inset on each panel represents a cartoon of the corresponding gap along the Fermi surface. White contour lines shown correspond to  $0.025N_0$ .

case, Fig. 2-10(b), for a circular Fermi surface, we recover well-known results for the ZDOS, including the double tails along the nodal directions forced by the vanishing of the bound state wavefunction exactly along the  $45^\circ$  directions in the quasiclassical theory [69]. While this feature remains, it becomes essentially invisible in the case of the square Fermi surface shown in Fig. 2-10(e), as the Fermi surface concentrates the quasiparticle trajectories even more in the nodal directions. Our primary results are now contained in Fig. 2-10(c) and Fig. 2-10(f). The extended- $s$  state  $\Phi_{s,\text{ani}}$  has been chosen deliberately to have gap minima along the  $0^\circ$  directions (along the Fe-Fe bond in the FeBS case). This is clearly visible in the case of an isotropic pocket, Fig. 2-10(c), as the tails, while not as well-defined as in the true nodal case, extend clearly along these directions in real space. These directions rotate by  $45^\circ$ , however, when the same gap exists on the square LiFeAs  $\gamma$  pocket, as in Fig. 2-10(f). In fact, the ZDOS in Fig. 2-10(f) strongly resembles the structure observed by Hanaguri *et al.* in recent STS measurements on LiFeAs [127].

The results in Fig. 2-10 strongly challenge the common interpretation of STS images of vortices, which assign gap minima to the directions of the extended intensity in real space. This is probably reasonable in the case of true nodes, as indicated by the  $d$ -wave examples shown, but fails if these minima are not sufficiently deep due to the competition with the Fermi surface effects. Now that the basic structure of this competition in the case of the ZDOS has been understood, it is interesting to ask what may happen in the case of finite energies  $\omega \neq 0$ . Fig. 2-11 shows the calculated LDOS  $N(\mathbf{r}, \omega)$  as a function of energy at the vortex core center [Fig. 2-11(a)–2-11(c)] and one coherence length away from the center in the  $0^\circ$  direction [Fig. 2-11(d)–2-11(f)] and  $45^\circ$  direction [Fig. 2-11(g)–2-11(i)]. The spectrum is quite insensitive to the Fermi surface shape at the vortex core center where the results for the circular FS and LiFeAs  $\gamma$  pocket are almost the same. Away from the vortex center, the direction-dependent LDOS  $N(\mathbf{r}, \omega = 0)$  reflects the competition between gap and Fermi surface anisotropy.

The higher/lower LDOS of the LiFeAs  $\gamma$  pocket/circular FS at zero energy in Fig. 2-11(i) than that in Fig. 2-11(f) is equivalent to our result shown in Fig. 2-10. The quasiclassical theory incorporates the FS properties solely via  $\mathbf{v}_F$ , and thus does not account for the possible changes in the shape of the constant energy surfaces for STS biases away from zero. Provided the band shape varies very slowly on the scale of  $T_c$ , this neglect should not significantly affect the shape of vortex bound states at nonzero energy, however. On the other hand, even within the current model, a more important effect may be included. In our analysis of LiFeAs, we have until now neglected all Fermi surface pockets except the outer ( $\gamma$ ) hole pocket, due to its square shape and because it seems likely to have the smallest gap. When the bias is increased, higher energy quasiparticle states, including those associated with larger gaps, will be probed. Within spin fluctuation theory [8], both the high density of states  $\alpha_2$  pocket, and the electron pockets, tend to have gap minima along the  $0^\circ$  directions. Thus as higher energies are probed, it is possible that *rotations* of the bound state shape may take place as the balance between gap structure and Fermi surface anisotropy is altered. Unfortunately even qualitative statements depend on the details of the sizes of gaps and gap anisotropies on each sheet, as well as on the various Fermi velocities for each band. The LiFeAs system is quite clean, however, and if the current controversy between ARPES [119] and dHvA [120] regarding the Fermi surface can be resolved, spectroscopies of bound states on this system should provide enough information to determine fairly detailed structure of the gap.

### 2.3.4 Conclusions

We have used quasiclassical methods to calculate the vortex bound states within a single vortex approximation, and highlighted the competition between gap and Fermi surface anisotropy in the determination of the shape of STS images of vortex bound states in LiFeAs. If the Fermi surface anisotropy is large enough, we have shown that the tails of vortex bound states at low energy need not correspond to the smallest gaps

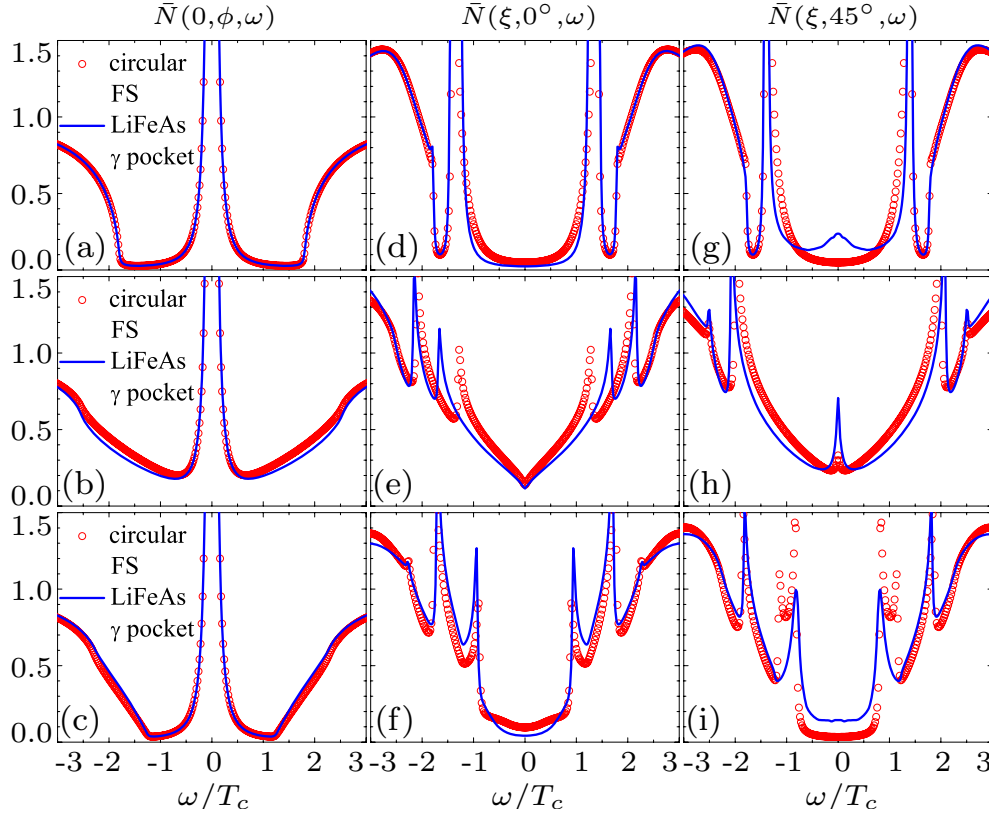


Figure 2-11. Normalized LDOS  $N(\mathbf{r}, \omega)/N_0 \equiv \bar{N}(\rho, \phi, \omega)$  vs energy for different gap models with a circular Fermi surface (red symbols) and LiFeAs  $\gamma$  pocket (blue line): (a), (d), (g) isotropic  $s$ -wave gap  $\Delta_0$ ; (b), (e), (h) nodal  $d$ -wave gap  $\Delta_0 \sqrt{2} \cos 2\theta$ ; (c), (f), (i) extended  $s$ -wave gap  $\Delta_0(1 - r \cos 4\theta)/\sqrt{1 + r^2/2}$ ,  $r = 0.3$ . The gap bulk value is taken to be  $\Delta_0 = 1.76 T_c$ .  $\mathbf{r} = (\rho, \phi) = (0, \phi)$  for (a)–(c);  $(\xi, 0^\circ)$  for (d)–(f);  $(\xi, 45^\circ)$  for (g)–(i).  $\xi$  is the coherence length.

in the system, if those gaps are not true nodes. The ZDOS shape measured by STS in experiments on the LiFeAs system with very clean surfaces is well reproduced by numerical calculation. Within our model, we attribute the tail-like spectrum to the effect of the non-uniformly distribution of Fermi velocity direction on the Fermi surface of the LiFeAs  $\gamma$  hole pocket. Further measurements of the energy dependence of bound state shape may further help identify the gap anisotropy.

## CHAPTER 3 DISORDER IN SUPERCONDUCTORS

Some parts of this chapter have been published as “Using controlled disorder to distinguish  $s_{\pm}$  and  $s_{++}$  gap structure in Fe-based superconductors,” Yan Wang, A. Kreisel, P. J. Hirschfeld, and V. Mishra, Phys. Rev. B **87**, 094504 (2013).

### 3.1 Motivation

Determining the symmetry and structure of the superconducting order parameter in Fe-based superconductors (FeBSs) is one of the main challenges in this new field [8, 9]. The sign-changing  $s_{\pm}$  and single sign  $s_{++}$  gap described in the Introduction chapter are two promising candidates for FeBS with a typical nested Fermi surface (FS) including two or three  $[\Gamma = (0, 0)]$ -centered hole pockets and two  $[M = (\pi, \pi)]$ -centered electron pockets in the two-Fe zone composed primarily of Fe  $3d$  states. Surprisingly, it has proven rather difficult to definitively distinguish these types of gap structures experimentally, in part because phase-sensitive experiments are challenging due to surface properties; because of the multiband nature of the electronic structure; and because the  $s_{\pm}$  and  $s_{++}$  “states” are symmetry equivalent, transforming both according to the  $A_{1g}$  representation of the crystal point group. As mentioned in the last part of Chapter 1, only a handful of experiments offer indirect evidence in favor of the  $s_{\pm}$  state [52–59].

On the other hand, alternative explanations have been offered for all these measurements; in particular, Kontani and Onari have provided an alternate explanation [48] for the neutron resonance features within an  $s_{++}$  scenario via a postulated energy dependence of the quasiparticle relaxation time. In addition, several references [132–136] have called attention to a “slow” decrease of  $T_c$  in chemical substitution experiments [135–139], which is then ascribed to the natural robustness against nonmagnetic disorder of an  $s_{++}$  superconductor. It is this issue which we study here.

It is important to understand what is meant by “slow” and “fast”  $T_c$  suppression in this context. At one extreme we have situations in which  $T_c$  is not suppressed by nonmagnetic disorder at all. According to Anderson's theorem [140], the critical temperature of an isotropic conventional  $s$ -wave superconductor with a single band of electrons is unaffected by nonmagnetic scatterers. From this statement it follows immediately that the same occurs for two bands in an isotropic  $s_{++}$  state (with equal gaps), but also in an  $s_{\pm}$  state with no interband scattering. At the other extreme, we know that magnetic scatterers in a conventional isotropic superconductor suppress  $T_c$  according to the Abrikosov-Gor'kov (AG) law [141]; it is well known that *nonmagnetic* scatterers suppress  $T_c$  at the same fast AG rate in a two-band  $s_{\pm}$  state, *provided* the two densities of states  $N_a = N_b$  and two gaps  $\Delta_a = -\Delta_b$  are equal in magnitude, and the scattering is purely *interband* in nature. Any deviation from these assumptions will *slow* the  $T_c$  suppression rate relative to the AG rate. Therefore between these two extremes lie many possibilities for  $T_c$  suppression behavior which depend on details of the electronic structure and the relative amplitudes of inter- and intraband scattering.

Several theoretical calculations of  $T_c$  suppression have discussed the pairbreaking effects of nonmagnetic scatterers on model multiband superconductors with generalized  $s$ -wave order [91, 132, 133, 142–152]. In fact the situation is generally even more complicated than discussed above or in these works, since chemical impurities may do more than simply provide a scattering potential: they may dope the system, or alter the pairing interaction itself locally. We therefore believe (see also Ref. [8, 9]) that measurements of  $T_c$  suppression relative to the amount of chemical disorder are not particularly useful to determine the gap structure in multiband systems. To improve the situation, one first needs to find a way to create pointlike potential scattering centers, so as to create disordered systems to which the above theoretical works apply. The closest approach to this ideal is achieved with low-energy electron irradiation, which is thought to create interstitial-vacancy pairs. Experiments of this type are being performed

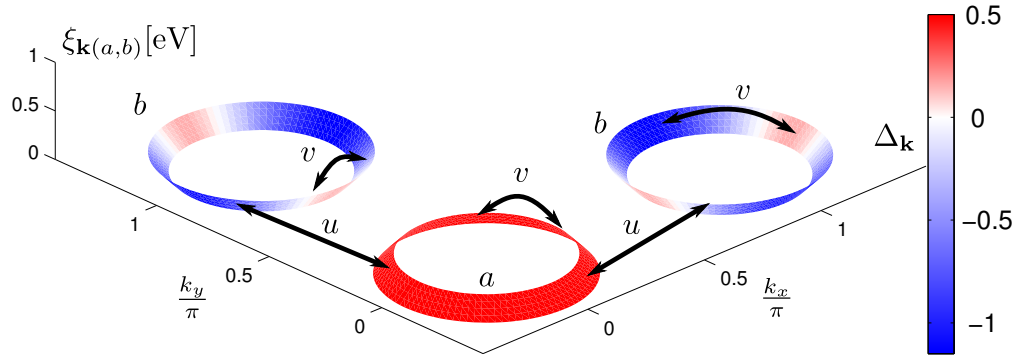


Figure 3-1. Sketch of the two-band model with linearized band dispersions on the Fermi sheets  $a$  and  $b$  and constant impurity scattering  $v$  (intraband) and  $u$  (interband), together with a possible nodal  $s$ -wave gap on the bands in the superconducting state.

currently, and it is one of the goals of this work to make predictions to guide the analysis of such data.

The other needed improvements are theoretical: first, the pairbreaking theory must be extended to relate  $T_c$  only to directly measurable quantities, like the change in residual ( $T \rightarrow 0$ ) resistivity caused by the disorder, rather than to any theoretically meaningful but empirically inaccessible scattering rate parameter. Second, since the theory involves many parameters, the robustness of any claimed fit must be tested by the simultaneous prediction of other quantities which depend on disorder, such as the low-temperature penetration depth, nuclear magnetic resonance (NMR) relaxation rate, or thermal conductivity. Finally, it would be useful to have *ab initio* calculations of vacancy and interstitial potentials to constrain the impurity parameters used. This has been attempted for chemical substituents [153–155] recently.

### 3.2 Model

We consider a system with two bands  $a$  and  $b$  with linearized dispersion close to the Fermi level that lead to densities of state  $N_a$  and  $N_b$  in the normal state; see Fig. 3-1.

The  $t$ -matrix equation in the two-band model has the form

$$\hat{\Sigma} = n_{\text{imp}} \hat{\mathbf{t}}, \quad (3-1)$$

$$\hat{\mathbf{t}} = \hat{\mathbf{u}} + \hat{\mathbf{u}} \hat{\mathbf{g}} \hat{\mathbf{t}}, \quad (3-2)$$

where  $n_{\text{imp}}$  is the concentration of impurities,  $\hat{\mathbf{t}}(n_{\text{imp}}) = \sum_{i=0}^3 \mathbf{t}^{(i)} \otimes \hat{\tau}_i$ ,  $\hat{\mathbf{g}}(n_{\text{imp}}) = \mathbf{g}_0 \otimes \hat{\tau}_0 + \mathbf{g}_1 \otimes \hat{\tau}_1$  and  $\otimes$  represents a product of band (bold) and Nambu (caret) matrices.  $\mathbf{g}_0 = \text{diag}(g_{0a}, g_{0b})$  and  $\mathbf{g}_1 = \text{diag}(g_{1a}, g_{1b})$  are local Green's functions in the  $\tau_0$  and  $\tau_1$  channels (we have assumed particle-hole symmetry in order to neglect  $\mathbf{g}_3$ ), where  $\hat{\tau}_i$  denote Pauli matrices in Nambu space. Due to the translational invariance of the disorder-averaged system,  $\hat{\mathbf{g}}$  is diagonal in band space. We now assume a simple model for impurity scattering whereby electrons scatter within each band with amplitude  $v$  and between bands with amplitude  $u$ ,

$$\hat{\mathbf{u}} = \begin{pmatrix} v & u \\ u & v \end{pmatrix} \otimes \hat{\tau}_3. \quad (3-3)$$

The  $t$ -matrix components are found from Eq. (3-2) to be

$$\begin{aligned} t_{aa}^{(0)} &= \frac{[g_{0b}u^2 + g_{0a}v^2 - g_{0a}(u^2 - v^2)^2 \delta g_b^2]}{\mathcal{D}}, \\ t_{aa}^{(1)} &= -\frac{[g_{1b}u^2 + g_{1a}v^2 - g_{1a}(u^2 - v^2)^2 \delta g_b^2]}{\mathcal{D}}, \end{aligned} \quad (3-4)$$

and  $t_{bb}^{(i)} = t_{aa}^{(i)} (a \leftrightarrow b)$ , where

$$\begin{aligned} \mathcal{D} &= 1 - (\delta g_a^2 + \delta g_b^2) v^2 + \delta g_a^2 \delta g_b^2 (u^2 - v^2)^2 - \\ &\quad - 2u^2 (g_{0a}g_{0b} - g_{1a}g_{1b}) \end{aligned} \quad (3-5)$$

with the abbreviation  $\delta g_\alpha^2 = g_{0\alpha}^2 - g_{1\alpha}^2$ .

### 3.3 $T_c$ Suppression

The linearized multiband gap equation near  $T_c$  is (see, e.g., Ref. [91])

$$\Delta_\alpha(\mathbf{k}) = 2T \sum_{\mathbf{k}', \beta, \omega_n > 0}^{\omega_n = \omega_c} V_{\mathbf{k}\mathbf{k}'}^{\alpha\beta} \frac{\tilde{\Delta}_\beta(\mathbf{k}')}{\tilde{\omega}_\beta^2 + \xi_\beta^2}, \quad (3-6)$$

where  $\xi_\beta$  is the linearized dispersion of band  $\beta$ , and we introduced the shifted gaps and frequencies,  $\tilde{\Delta}_\beta(\mathbf{k}') = \Delta_\beta(\mathbf{k}') + \Sigma_\beta^{(1)}$  and  $\tilde{\omega}_\beta = \omega_n + i\Sigma_\beta^{(0)}$ . We will simplify the model above further in that we adopt a gap structure similar to that obtained from spin fluctuation theories: The gap on the (hole) pocket  $a$  is isotropic,  $\Delta_a$ , and the gap on the (electron) pocket  $b$  may be anisotropic,  $\Delta_b = \Delta_b^0 + \Delta_b^1(\theta)$ , where  $\theta$  is the momentum angle around the  $b$  pocket and  $\int d\theta \Delta_b^1(\theta) = 0$ . The pairing potential is then taken as  $V_{\mathbf{k}\mathbf{k}'}^{\alpha\beta} = V_{\alpha\beta} \phi_\alpha(\mathbf{k}) \phi_\beta(\mathbf{k}')$ , with  $\phi_\alpha = 1 + r\delta_{\alpha,b} \cos 2\phi$ , and  $\phi$  is the angle around the electron pocket. The parameter  $r$  controls the degree of anisotropy, and creates nodes if  $r > 1$ .

This ansatz then gives three coupled gap equations for  $(\Delta_a, \Delta_b^0, \Delta_b^1)^T \equiv \underline{\Delta}$ . In the  $\underline{\Delta}$  basis we can write the gap equations in the compact form

$$\underline{\Delta} = \ln\left(1.13 \frac{\omega_c}{T_c}\right) \underline{\mathcal{M}} \underline{\Delta} \equiv \mathcal{L}_0 \underline{\mathcal{M}} \underline{\Delta}, \quad (3-7)$$

where the matrix  $\underline{\mathcal{M}} = (1 + \underline{\mathcal{V}} \underline{\mathcal{R}}^{-1} \underline{\mathcal{X}} \underline{\mathcal{R}})^{-1} \underline{\mathcal{V}}$  and the constant  $\mathcal{L}_0 = \ln(1.13 \frac{\omega_c}{T_c})$  were introduced. Here  $\underline{\mathcal{V}}$  is the interaction matrix in the above basis.  $\underline{\mathcal{R}}$  is the orthogonal matrix which diagonalizes the matrix  $\underline{\Delta}$ ,

$$\underline{\Delta} = \frac{\pi n_{\text{imp}}}{\mathcal{D}_N} \begin{bmatrix} N_b u^2 & -N_b u^2 & 0 \\ -N_a u^2 & N_a u^2 & 0 \\ 0 & 0 & N_b v^2 + N_a u^2 \end{bmatrix}, \quad (3-8)$$

where

$$\mathcal{D}_N = 1 + 2u^2 \pi^2 N_a N_b + (u^2 - v^2)^2 \pi^4 N_a^2 N_b^2 + v^2 \pi^2 (N_a^2 + N_b^2) \quad (3-9)$$

is Eq. (3–5) evaluated in the normal state where the limit  $\underline{\Delta} \rightarrow 0$  has been taken in the local Greens functions.  $\underline{\mathcal{X}}$  is a matrix with only diagonal elements,

$$\mathcal{X}_{ii} = \mathcal{L}_0 - \left[ \Psi\left(\frac{1}{2} + \frac{\omega_c}{2\pi T_c} + \frac{\lambda_i}{2\pi T_c}\right) - \Psi\left(\frac{1}{2} + \frac{\lambda_i}{2\pi T_c}\right) \right], \quad (3-10)$$

where  $\Psi$  is the digamma function and  $\lambda_i$  are the eigenvalues of the matrix  $\underline{\Delta}$ . The maximum eigenvalue  $[\lambda_{\max}(T_c)]$  of the matrix  $\underline{\mathcal{M}}$  determines  $T_c$  via  $T_c = 1.13\omega_c e^{-1/\lambda_{\max}}$ .

### 3.4 Residual Resistivity

The most direct observable measure of scattering in  $T_c$  suppression experiments is the residual resistivity change  $\Delta\rho_0$ , i.e., the change in the extrapolated  $T \rightarrow 0$  value of the resistivity with disorder. We will assume that interference effects between elastic and inelastic processes are negligible, i.e., that the effect on the  $\rho(T)$  curve when the system is disordered is essentially a  $T$ -independent shift upward. We therefore calculate  $\Delta\rho_0$  within the same framework as above, assuming that all defects are pointlike. In the zero frequency limit, there are no interband transitions, and the total conductivity in the  $x$  direction is the sum of the Drude conductivities of the two bands,  $\sigma = \sigma_a + \sigma_b$ , with  $\sigma_\alpha = 2e^2 N_\alpha \langle v_{\alpha,x}^2 \rangle \tau_\alpha$ , where  $v_{\alpha,x}$  is the component of the Fermi velocity in the  $x$  direction and  $\tau_\alpha$  the corresponding single particle relaxation time obtained from the self-energy in the  $t$ -matrix approximation,  $\tau_\alpha^{-1} = -2 \text{Im} \Sigma_\alpha^{(0)}$ . Note that  $\tau_\alpha^{-1}$  contains contributions from both the intraband and interband impurity scattering processes. The transport time and single-particle lifetime are identical within this model because of our assumption of pointlike  $s$ -wave scatterers, which implies that corrections to the current vertex vanish. A finite spatial range of the scattering potential will tend to steepen the  $T_c$  vs  $\Delta\rho_0$  curve [156, 157].

## 3.5 Results

### 3.5.1 $T_c$ Suppression vs Resistivity

We now solve Eqs. (3–7) for  $T_c$  and calculate simultaneously the change in resistivity  $\Delta\rho_0$  at  $T \rightarrow 0$ . Unlike  $T_c$  vs  $n_{\text{imp}}$  or various scattering rates,  $T_c$  vs  $\Delta\rho_0$  can then

be compared directly to experiment. Clearly, the results will be parameter dependent, however, so we here specify our precise assumptions regarding the electronic structure. For concreteness, we focus on the  $\text{BaFe}_2\text{As}_2$  (Ba122) system on which the largest number of measurements have been reported. We choose values for the Fermi velocities and densities of states at the Fermi level that are compatible with both density functional theory (DFT) calculations [4] and angle-resolved photoemission spectroscopy (ARPES) measurements [158, 159]. We assume a density of states on each Fermi surface sheet of  $N_a = 3.6$  and  $N_b = 2.7/\mathcal{V}_c/\text{eV}/\text{spin}$  ( $\mathcal{V}_c$  is the unit cell volume), for the “effective” hole and electron pockets, respectively, that approximately describes the imbalance in the densities of states that also has been seen with ARPES [158–160], and is consistent with the density of states of Ba122 arising from Fe  $d$ -orbitals according to DFT calculations [4] with an effective-mass renormalization of  $z = 3$ . We take the root-mean-square Fermi velocities as  $v_{F,a} = 2/3 \times 10^5 \text{ m/s}$  and  $v_{F,b} = 10^5 \text{ m/s}$  from  $v_{F,\perp}$  in Table I of Ref. [92], and renormalize them by the same factor of  $z = 3$  to approximately match the velocities found in ARPES experiments [158–160]. In the transport calculation, the component of the Fermi velocities in the direction of the current is taken to be  $\langle v_{F\alpha,x}^2 \rangle = 1/2 v_{F\alpha}^2$  due to the quasi-cylindrical Fermi surface. The pairing potentials chosen for the main text are  $V_{aa} = V_{bb} = 0.05$  and  $V_{ab} = V_{ba} = -0.04$ .

Using these parameters, we obtain for the isotropic case ( $r = 0$ ) the zero temperature gap values of  $\Delta_{a0}^0 = -1.79 T_{c0}$  and  $\Delta_{b0}^0 = 1.73 T_{c0}$ , whereas for the nodal case ( $r = 1.3$ ) these are  $\Delta_{a0}^0 = -1.22 T_{c0}$  and  $\Delta_{b0}^0 = 1.23 T_{c0}$  with the critical temperature chosen as  $T_{c0} = 30 \text{ K}$ . We have fixed the intraband scattering potential at an intermediate strength value of  $\nu = 0.25$ , but show results for other values in the Appendix. Potentials are given in eV and we set  $\hbar = k_B = 1$ .

In Fig. 3-2, we now exhibit  $T_c$  suppression vs the corresponding change in residual resistivity  $\Delta\rho_0$  as defined above, both for a fully isotropic  $s_{\pm}$  gap ( $r = 0$ ), and for a gap which has nodes on the electron pockets ( $r = 1.3$ ), for a range of ratios  $u/\nu$ . It is

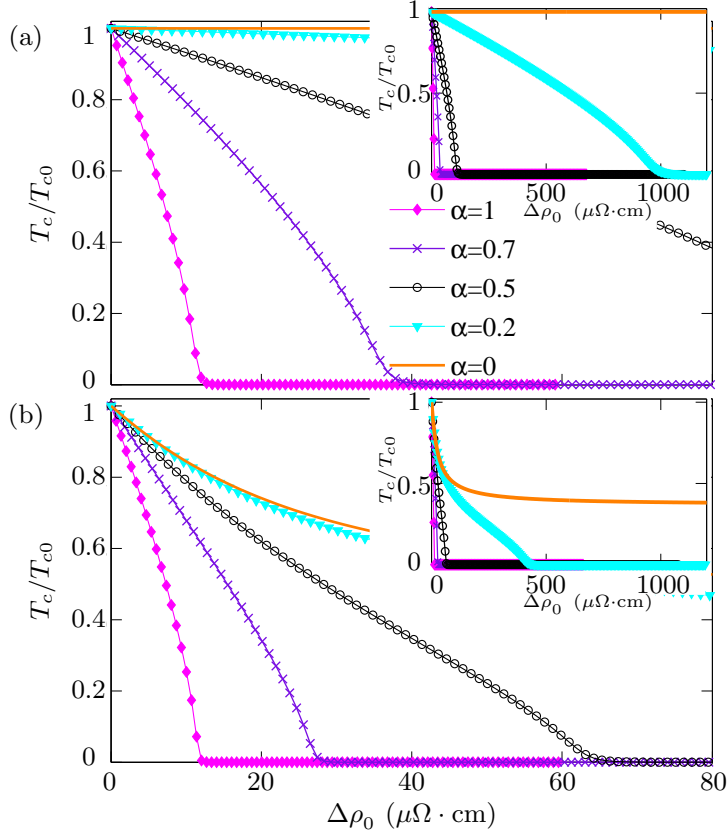


Figure 3-2. (a) Normalized critical temperature  $T_c/T_{c0}$  vs disorder-induced resistivity change  $\Delta\rho_0$  for isotropic  $s_{\pm}$ -wave pairing for various values of the inter- to intraband scattering ratio  $\alpha \equiv u/v$ . Inset: Same quantity plotted over a larger  $\Delta\rho_0$  scale. (b) As (a) but for an anisotropic (nodal) gap with anisotropy parameter  $r = 1.3$ .

clear that a wide variety of initial slopes and critical resistivities  $\Delta\rho_0^c$  for which  $T_c \rightarrow 0$  is possible, depending on the scattering character of the impurity. The variability of the suppression rate with the ratio of inter- to intraband scattering has been noted by various authors [91, 152] before this. In fact, Efremov *et al.* [152] have shown that the various  $T_c$  suppression curves of the isotropic  $s_{\pm}$  gap fall onto universal curves depending on whether the average pair coupling constant  $\langle\lambda\rangle <, =, > 0$  when plotted against the interband scattering rate (which is not directly measurable, however).

Here  $\langle\lambda\rangle = \frac{1}{N_a+N_b} \sum_{\alpha,\beta \in \{a,b\}} N_{\alpha} V_{\alpha\beta} N_{\beta}$ . We have used a value  $\langle\lambda\rangle = 0.037 \approx 0$  in our investigations. We have examined other parameter sets with negative  $\langle\lambda\rangle$ , and

found no essential difference in  $T_c$  when plotted against the residual resistivity  $\Delta\rho_0$ , which of course depends on both intra- and interband scattering. Other works have made comparisons with the resistivity changes (for example Refs. [135, 136]), but have typically presented results for  $s_{\pm}$  states only for a single set of impurity parameters corresponding to the fastest rate of  $T_c$  suppression. Such assumptions lead always to critical  $\Delta\rho_0$  values comparable to the smallest ones seen in Fig. 3-2, of order tens of  $\mu\Omega$  cm. Here we see that more general values of the parameters can easily lead to much slower  $T_c$  vs  $\Delta\rho_0$  suppression rates by disorder, with critical disorder  $\Delta\rho_0^c$  values of order  $m\Omega$  cm. As discussed by Li *et al.* [135], such values are typical of chemical substitutions on various different lattice sites; here we see that such slow  $T_c$  suppression does not rule out the  $s_{\pm}$  state, even within the assumptions of our potential-scattering-only model.

To check how robust our conclusions are, we take different values for the impurity parameters and pair potential parameters: when we increase the intraband scattering potential  $v$  to  $v = 1.25 \text{ eV } \mathcal{V}_c$  keeping all other parameters identical to those of Fig. 3-2, the  $T_c$  suppression significantly slows, as seen in Fig. 3-3, with the exception of the value  $\alpha = 1$ , which plays a special role in the theory of two-band  $s_{\pm}$  superconductivity, as can be easily checked analytically. While in Ref. [48] it was argued that the interband scattering potential  $u$  should be generically large for any chemical substituent, there is no reason to expect  $\alpha = 1$  to hold exactly, and therefore we see that large critical resistivities  $\Delta\rho_0^c$  are even more likely to be found for stronger impurities (the unitarity limit  $v \rightarrow \infty$  with fixed  $\alpha$  is pathological in this model [152] and we have not considered it here). The special role of the value  $\alpha = 1$  can be illustrated by plotting the resistivity  $\Delta\rho_{1/2}$  at which the critical temperature is suppressed by half,  $T_c = 0.5 T_{c0}$ , as shown in Fig. 3-4, which may be compared with experiments. Note that  $\alpha \simeq 1$  yields the fastest  $T_c$  suppression independent of the impurity potential in the physical regime  $v \gtrsim u$ .

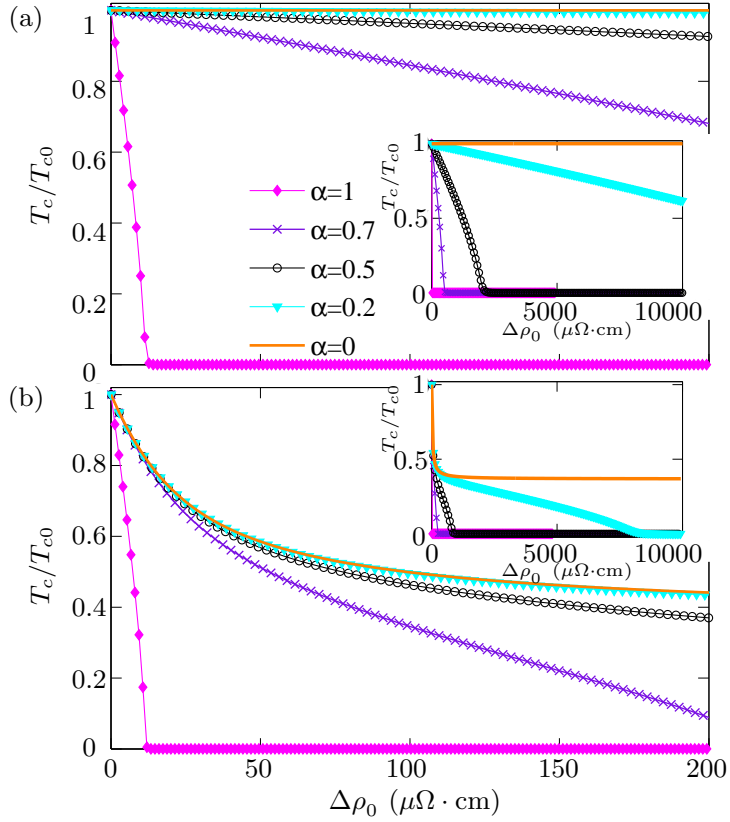


Figure 3-3.  $T_c/T_{c0}$  vs  $\Delta\rho_0$  for various values of the inter- to intraband scattering ratio  $\alpha \equiv u/v$  with  $v = 1.25 \text{ eV } \mathcal{V}_c$ . (a) for isotropic  $s_{\pm}$  wave pairing and (b) for an anisotropic (nodal) gap with anisotropy parameter  $r = 1.3$ .

### 3.5.2 Density of States

A real understanding of the effects of disorder in a given situation will probably depend on correlating the results of several experiments. Other quantities which are quite sensitive to disorder are the temperature dependence of the low- $T$  London penetration depth  $\Delta\lambda(T)$  and the nuclear magnetic spin-lattice relaxation time  $T_1^{-1}$ . Within BCS theory, these quantities are controlled by the low-energy density of states. In the pure system, the nodal structure then determines the power law of temperature, and one generically expects  $\Delta\lambda(T) \sim T$  for gap line nodes except in very special situations [161]. In the presence of a small amount of nonmagnetic disorder, a finite density of states is created [162, 163] which leads automatically to a  $T^2$  term in the

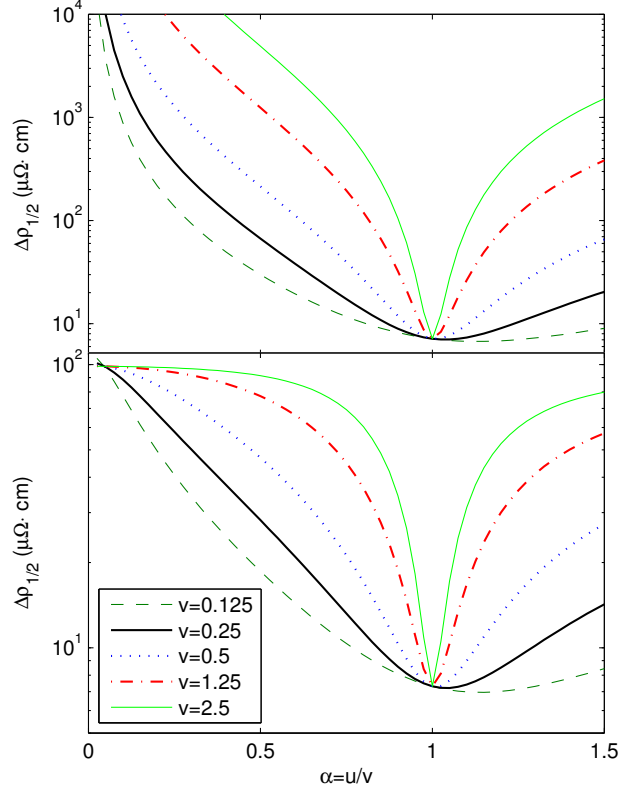


Figure 3-4. The resistivity at half suppression  $\Delta\rho_{1/2}$  as a function of the ratio  $\alpha = u/v$  for various intraband impurity potentials  $v$  (measured in  $\text{eV } \mathcal{V}_c$ ); the other parameters are taken as in the main text for the isotropic  $s_{\pm}$  wave pairing (top) and for an anisotropic (nodal) gap (bottom).

penetration depth [161, 164]. If the state is of  $s$  character, the gap nodes are not symmetry protected and can be lifted by further addition of disorder [91, 165].

### 3.5.3 Nonmonotonic Dependence of Residual DOS on Disorder

In this work we note a further possibility in the disorder evolution of the low-energy density of states (DOS) of a nodal multiband  $s_{\pm}$ -wave superconductor, namely, that a reentrant behavior of  $N(0)$  can occur after lifting of the nodes. The reason is that, in a situation dominated by intraband scattering but with nonzero interband scattering, anisotropy of the gaps on each individual sheet will quickly be averaged on introduction of intraband disorder. If the state is  $s_{\pm}$ , a midgap impurity state can then be created by interband scattering, and grow until it overlaps the Fermi level, as shown schematically in Fig. 3-5(a). Such midgap states are the analogs of the Yu-Shiba bound states

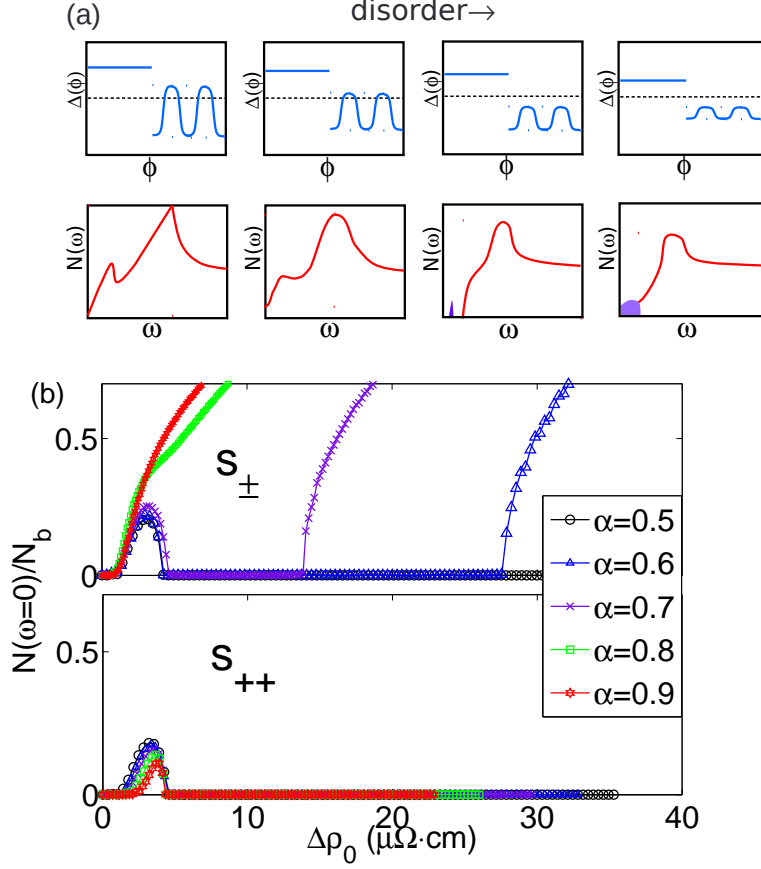


Figure 3-5. (a) Schematic evolution of the order parameter and density of states with increasing disorder for a system with intra- and interband scattering. (b) Top: Fermi level density of states  $N_b(0)$  (nodal band) as shown in Fig. 3-2(b) vs  $\Delta\rho_0$  for various values of scattering ratio  $u/v$  in an anisotropic  $s_{\pm}$  state. Bottom: Fermi-level density of states for anisotropic  $s_{++}$  state with  $V_{ab}$  identical in magnitude to the above panel, but positive. Anisotropy parameter  $r = 1.3$  in both cases.

created by magnetic impurities in conventional superconductors, and can appear for nonmagnetic impurities if the superconducting gap changes sign [106]. The residual density of states  $N(0) = -\text{Im} \sum_{\mathbf{k}} \text{Tr} \hat{G}(\mathbf{k}, \omega = 0)/(2\pi)$  ( $\hat{G}$  is the Nambu Green's function) effectively determines the low-energy thermodynamic behavior, so we have plotted it for the anisotropic band as a function of increasing disorder in Fig. 3-5, for both  $s_{\pm}$  and  $s_{++}$  states. In the former case the reentrant behavior is clearly seen.

The corresponding sequence with increasing disorder in the  $s_{\pm}$  penetration depth  $\Delta\lambda(T)$  would be  $T \rightarrow T^2 \rightarrow \exp(-\Omega_G/T) \rightarrow T^2$ , where  $\Omega_G$  is the minimum gap in the system. This sequence of low  $T$  penetration depths has recently been observed by the Kyoto group (T. Shibauchi, private communication). For the NMR spin-lattice relaxation rate  $T_1^{-1}$ , the analogous evolution should be  $T^3 \rightarrow T \rightarrow \exp(-\Omega_G/T) \rightarrow T$ . The residual linear  $T$  term in the thermal conductivity,  $\kappa(T \rightarrow 0)/T$ , should vanish and then reappear with increasing disorder. In the  $s_{++}$  case, the last step in each sequence is entirely absent, since interband scattering cannot give rise to low-energy bound state formation.

### 3.5.4 Realistic Impurity Potentials

It is clear from the above analysis that we have established that there is a wide range of possibilities for the behavior of  $T_c$  in an  $s_{\pm}$  superconductor, as well as for low-temperature properties like the penetration depth, when disorder is systematically increased. To make more precise statements, one needs to have some independent way to fix the scattering potential of a given impurity, and in particular the relative proportion of inter- to intraband scattering. Kemper *et al.* [153] found the ratio between inter- and intraband scattering to be of order  $\alpha = 0.3$  for Co in Ba122, which would lead according to Fig. 3-2 to a critical resistivity strength of about  $300\mu\Omega\text{ cm}$ , roughly in accord with experiment [135, 136]. Onari and Kontani [134] have made the important point that the “natural” formulation for a model impurity potential, i.e., diagonal in the basis of the five Fe  $d$  orbitals, automatically leads to significant interband scattering if one transforms back to the band basis. However, simple estimates show that depending on details  $\alpha$  for on-site Fe substituents can vary between 0.2 and 1, again leading as seen in Fig. 3-2 to a wide variety of possible  $T_c$  suppression scenarios.

## 3.6 Conclusions

We have argued that  $s_{\pm}$  pairing cannot be ruled out simply because the  $T_c$  suppression is slow according to some arbitrary criterion. The definitive experiments

along these lines will most probably involve electron irradiation, where one can be reasonably sure that the defects created act only as potential scatterers. In this case we find critical resistivities for the destruction of superconductivity which vary over two orders of magnitude according to the ratio of interband to intraband scattering. Results for the  $s_{\pm}$  state are then not inconsistent with experimental data, but proof of sign change of the order parameter relies on knowledge of the impurity potential, which requires further *ab initio* calculations for each defect in each host. As an alternative approach, we have proposed that systematic variation of disorder could give rise to a clear signature of  $s_{\pm}$  pairing in the low-energy Fermi level DOS  $N(0)$ . In an  $s_{\pm}$  state,  $N(0)$  could increase with disorder, vanish again due to node lifting, and increase again afterward due to impurity bound state formation. This “reentrant” behavior of the DOS will be reflected in the temperature dependence of low-temperature quasiparticle properties like the penetration depth, nuclear spin relaxation time, or thermal conductivity. For some materials (with gap nodes), this could be a “smoking gun” experiment for  $s_{\pm}$  pairing.

## CHAPTER 4 SPIN-FLUCTUATION PAIRING IN FE-BASED SUPERCONDUCTORS

Some parts of this chapter have been published as “Superconducting gap in LiFeAs from three-dimensional spin-fluctuation pairing calculations,” Yan Wang, A. Kreisel, V. B. Zabolotnyy, S. V. Borisenko, B. Büchner, T. A. Maier, P. J. Hirschfeld, and D. J. Scalapino, *Phys. Rev. B* **88**, 174516 (2013).

### 4.1 Motivation

The compound LiFeAs is an 18 K superconductor that presents several novel features relative to the other families of Fe pnictides [6]. High-quality crystals with atomically flat nonpolar surfaces are now straightforward to prepare, and the surface electronic structure has been shown to be the same as in the bulk [166], suggesting that this system and related 111 materials are ideal ones to apply surface spectroscopies like angle-resolved photoemission (ARPES) and scanning tunneling microscopy (STM) [127]. ARPES experiments [119, 124, 167] and electronic structure calculations within density functional theory (DFT) [166–168] reported early on a Fermi surface very different from the conventional set of hole and electron pockets predicted by DFT for the other Fe-based superconductors (Figs. 4-1 and 4-2). In particular, less clear nesting of hole and electron pockets was observed, leading to the suggestion that this was the reason for the absence of magnetism in this parent compound [119]. More recently, de Haas-van Alphen (dHvA) measurements [120] showed reasonable agreement with bulk DFT for orbits on the electron pockets.

One continuing puzzle has been the small to negligible size of the inner ( $\alpha_1$ ,  $\alpha_2$ ) hole pockets observed by ARPES compared to the relatively large sizes found in DFT. Recently, local-density approximation (LDA) + dynamical mean-field theory (DMFT) calculations have presented a picture which suggests that the 111 materials are considerably more correlated than, e.g., the well-studied 122 materials and have argued that stronger interactions lead to a shrinkage of the inner hole pockets but

maintenance of the electron pocket size and shape [169–171]. This picture would then account for both ARPES and dHvA results, including very recent dHvA measurements which detected very small holelike orbits [172]. However, the extent of the agreement of LDA + DMFT theory and experiment for the hole pockets is obscured somewhat by disagreements among the various calculations as to the size of the inner pockets, as well as by the challenges of resolving the near-grazing  $\Gamma$ -centered hole bands in ARPES.

Within the spin-fluctuation model for pairing in the Fe-based materials, the structure of the Fermi surface is crucial for superconductivity as well as magnetism. Since the usual arguments leading to  $s_{\pm}$  pairing [46] invoke interband pair scattering between electron and hole pockets enhanced by nesting, the absence of nesting in this material would seem to undercut the case for an  $s_{\pm}$  superconducting state. A second aspect of this discussion relates to the spin symmetry of the order parameter. While early NMR work reported a strongly temperature-dependent Knight shift and  $1/T_1$  below  $T_c$ , consistent with  $s$ -wave pairing [173], Baek *et al.* [174] reported a Knight shift in some magnetic field directions with no  $T$  dependence, suggestive of equal spin-triplet pairing, which would then be consistent with theoretical analysis proposing triplet pairing for this system [175]. Neutron experiments have thus far not provided conclusive evidence one way or another. A weak incommensurate spin resonance was observed in inelastic neutron scattering experiments [176] and associated with a probable  $s_{\pm}$  state, but it should be noted that the existence of a spin resonance does not definitively exclude triplet pairing [177].

More recently, some authors [123] reported detailed ARPES measurements of the superconducting gap in LiFeAs. These measurements were remarkable in the sense that while they showed that the system has a full gap, consistent with other low-temperature probes [119, 121, 127, 178, 179], they also exhibited substantial gap anisotropy around both electron and hole Fermi surfaces. Similar but not quantitatively

identical results for anisotropic gaps were reported by Umezawa *et al.* [124] The reports of strongly angle-dependent gaps are relatively rare among the many ARPES measurements on Fe-based superconductors (for exceptions see Refs. [180] and [181]), where isotropic gaps are often reported even for those systems where it is believed from low-temperature transport measurements that gap nodes exist (for a discussion of this so-called “ARPES paradox,” see Ref. [8]). The existence of anisotropy around some of the Fermi-surface pockets of LiFeAs was also reported by Allan *et al.* [126], who performed high-resolution, low-temperature STM measurements together with a quasiparticle interference (QPI) analysis which found a small gap nearly identical to ARPES on the large outer hole ( $\gamma$ ) pocket, with gap minima along the Fe-Fe bond direction (as suggested in Ref. [182]). A second, larger gap, also with moderate anisotropy, was reported and attributed to an inner  $\alpha_{1,2}$  hole pocket.

To illustrate the types of gaps found by the ARPES experiments, we present in Fig. 4-2 a schematic representation of these data to familiarize the reader with the qualitative features reported. One can see that several aspects stand out: (a) oscillatory gaps on the outer hole ( $\gamma$ ) and electron ( $\beta$ ) pockets, (b) smallest gap on the  $\gamma$  pocket, and (c) large gaps of roughly equal average size on inner hole ( $\alpha$ ) and electron ( $\beta$ ) pockets. The relative phases of the gap oscillations on the two  $\beta$  pockets are also striking. We note here that the measurement of the gap on the  $\alpha$  pocket is particularly delicate since this band barely crosses the Fermi level near the  $Z$  point, and may not cross near  $\Gamma$  at all.

It is essential to the understanding of superconductivity in Fe-based superconductors to decide whether LiFeAs fits into the usual framework, with pairing driven by spin fluctuations, or represents different physics. Testing to see if the various qualitative and quantitative features of the gaps reported in experiment can be reproduced is therefore an important challenge to theory. In this chapter we calculate the effective pairing vertex within the fluctuation exchange approximation for the full

three-dimensional (3D) Fermi surface of LiFeAs and compare our results for the superconducting states which become stable at the transition to previous theory and to experiment. To understand how robust these results are, we perform the calculation for a band structure fit to the ARPES results, which differ primarily from DFT due to the much larger size of the inner hole pocket in the latter, as discussed above, as well as large shifts in the orbital character of the Fermi surfaces. In addition, we compare our results to a slightly hole-doped system to simulate the effect of missing Li at the LiFeAs surface and to calculations with a “standard” DFT band structure. We find that most aspects of the superconducting gap are remarkably well reproduced by the theory using the ARPES-derived electronic structure model. Our conclusion is that the superconductivity in LiFeAs is very likely to be of the “conventional”  $s_{\pm}$  type, with significant anisotropy on both hole and electron pockets.

#### 4.2 Ten-Orbital Tight-Binding Fits and Fermi Surfaces

Our approach here to the pairing calculation differs somewhat from those performed for materials where DFT and ARPES were in qualitatively good agreement. Since the spin-fluctuation pairing theory involves states very close to the Fermi surface, the disagreement between DFT and ARPES suggests that strong electronic correlations must be accounted for at some level. The simplest modification of the usual approach is to adopt a band structure which fits experiment well, a procedure which is not uniquely defined due to the multiband nature of the system. We have chosen to begin with a ten-Fe orbital tight-binding Hamiltonian  $H_0^{\text{ARPES}}$ , fit to measured ARPES data on a high-quality LiFeAs sample [123] using the method of Ref. [183], which we refer to as the ARPES-derived band structure. The hopping parameters and the dispersions are given in the Appendix B, and the comparison of the tight binding bands and Fermi surface cuts are shown in Fig. 4-1. The full Fermi surface from this model is then shown in Figs. 4-3(a) and 4-3(e) for two different dopings,  $n = 6.00$  and  $n = 5.90$ . The latter results are presented to mimic the possible effects of Li deficiency which are known to

be present in the sample and because the Fermi-surface topology changes abruptly near  $n = 6.00$ . We find that these changes are potentially quite important for the superconductivity, as discussed below.

It is interesting to first compare the ARPES-derived Fermi surface in Fig. 4-3(a) to the DFT Fermi surface discussed in the Appendix A.1 since the DFT results are essentially those used in earlier two-dimensional (2D) spin-fluctuation calculations [184]. Both the DFT- and the ARPES-derived Fermi surfaces include similar large hole pockets ( $\gamma$ ) and inner and outer electron pockets ( $\beta_{\text{in}}, \beta_{\text{out}}$ ). The  $\gamma$  pockets are of comparable size and are similar in shape. In the DFT-derived model, the inner and outer  $\beta$  pockets cross each other along high symmetry directions equivalent to  $X$ - $Y$  in the one-Fe zone. They also approach each other closely at nonzero  $k_z$  values away from the high-symmetry directions due to the hybridization of the DFT electron bands, and this leads to some  $k_z$  distortions and abrupt changes in their orbital characters with  $k_z$ . By contrast, the  $k_z$ -dispersions of the ARPES-derived electron pockets are weak. The pockets only approach each other at the high symmetry directions (where they cross in the absence of spin-orbit coupling), and they retain their orbital characters along  $k_z$ , as measured by the ARPES experiment.<sup>1</sup> The main difference beyond these shifts of orbital characters and shape of the outer  $\beta$  Fermi sheets is the much smaller  $\alpha_{1,2}$  hole pockets and the closing of the  $\alpha_2$  hole pocket in the ARPES-derived inner-hole Fermi sheets. The density of states (DOS) at the Fermi level is shown in Table A-1 in Appendix A.1. Within a scaling factor  $r = 0.5$ , the total densities of states and partial density of states are quite consistent between these two models.

The calculated carrier concentration in the compensated ( $n = 6.00$ ) case (where number of electrons/Fe = number of holes/Fe) from  $H_0^{\text{ARPES}}$  is roughly consistent with 0.18 electrons/Fe and 0.2 holes/Fe from the ARPES experiment by Umezawa

---

<sup>1</sup> Borisenko (unpublished).

*et al.* [124]. It is interesting to note that the difference in hole and electron carriers in Ref. [124] is already a hint that the surface of the sample may contain some Li vacancies and therefore be slightly hole doped. For the  $n = 5.90$  case we have chosen here for illustration's sake corresponding electron and hole densities that are 0.16 and 0.26, respectively.

In general, the ARPES-derived tight-binding model is a close fit to the ARPES data in Ref. [123] and reproduces the orbital characters on all pockets. One apparently minor discrepancy (which may play a more important role than expected at first sight; see below) is that due to the crystal symmetry, the two hole bands dispersing near  $Z$  in the tight-binding Hamiltonian  $H_0^{\text{ARPES}}$  are degenerate at the  $Z$  point and therefore in a nonrelativistic calculation must both cross or neither cross the Fermi surface, as shown in Fig. 4-4 (top panel). Apart from the large  $\gamma$  pocket, ARPES observes only a single holelike band ( $\alpha_2$ ) crossing the Fermi surface near  $Z$ , while a second holelike band ( $\alpha_1$ ) is pushed below. This suggests that spin-orbit coupling, which will split the two hole bands as shown in Fig. 4-4 (bottom panel), may be relevant here. For the moment we neglect this distinction and focus on the nonrelativistic band structure, but we will return to it in the discussion below.

### 4.3 Fluctuation Exchange Pairing Model

With the tight-binding Hamiltonian  $H_0$  in the previous section, we include the local interaction via the ten-orbital Hubbard-Hund Hamiltonian

$$\begin{aligned}
 H = H_0 &+ \bar{U} \sum_{i,\ell} n_{i\ell\uparrow} n_{i\ell\downarrow} + \bar{U}' \sum_{i,\ell' < \ell} n_{i\ell} n_{i\ell'} \\
 &+ \bar{J} \sum_{i,\ell' < \ell} \sum_{\sigma,\sigma'} c_{i\ell\sigma}^\dagger c_{i\ell'\sigma'}^\dagger c_{i\ell\sigma'} c_{i\ell'\sigma} + \bar{J}' \sum_{i,\ell' \neq \ell} c_{i\ell\uparrow}^\dagger c_{i\ell\downarrow}^\dagger c_{i\ell'\downarrow} c_{i\ell'\uparrow}, \quad (4-1)
 \end{aligned}$$

where the interaction parameters  $\bar{U}$ ,  $\bar{U}'$ ,  $\bar{J}$ ,  $\bar{J}'$  are given in the notation of Kuroki *et al.* [185]. Here  $\ell$  is the orbital index corresponding to Fe  $3d$ -orbitals, and  $i$  is the Fe *atom*

site. The spectral representation of the one-particle Green's function is given as

$$G_{\ell_1\ell_2}(\mathbf{k}, i\omega_n) = \sum_{\mu} \frac{a_{\mu}^{\ell_1}(\mathbf{k})a_{\mu}^{\ell_2,*}(\mathbf{k})}{i\omega_n - E_{\mu}(\mathbf{k})}, \quad (4-2)$$

where the matrix elements  $a_{\mu}^{\ell}(\mathbf{k}) = \langle \ell | \mu \mathbf{k} \rangle$  are spectral weights of the Bloch state  $|\mu \mathbf{k}\rangle$  with band index  $\mu$  and wave vector  $\mathbf{k}$  in the orbital basis and  $\omega_n$  are the fermionic Matsubara frequencies. In terms of the Green's function, the orbitally resolved noninteracting susceptibility is

$$\chi_{\ell_1\ell_2\ell_3\ell_4}^0(\mathbf{q}, i\omega_m) = -\frac{1}{N\beta} \sum_{\mathbf{k}, i\omega_n} G_{\ell_4\ell_2}(\mathbf{k}, i\omega_n) G_{\ell_1\ell_3}(\mathbf{k} + \mathbf{q}, i\omega_n + i\omega_m), \quad (4-3)$$

where  $N$  is the number of Fe atom sites,  $\beta = 1/T$  is the inverse temperature and  $\omega_m$  are the bosonic Matsubara frequencies. After summing the fermionic Matsubara frequencies following the analytic continuation to the real axis of bosonic Matsubara frequencies, we obtain the retarded susceptibility

$$\chi_{\ell_1\ell_2\ell_3\ell_4}^0(\mathbf{q}, \omega) = -\frac{1}{N} \sum_{\mathbf{k}, \mu\nu} \frac{a_{\mu}^{\ell_4}(\mathbf{k})a_{\mu}^{\ell_2,*}(\mathbf{k})a_{\nu}^{\ell_1}(\mathbf{k} + \mathbf{q})a_{\nu}^{\ell_3,*}(\mathbf{k} + \mathbf{q})}{\omega + E_{\mu}(\mathbf{k}) - E_{\nu}(\mathbf{k} + \mathbf{q}) + i0^+} \times \{f[E_{\mu}(\mathbf{k})] - f[E_{\nu}(\mathbf{k} + \mathbf{q})]\}. \quad (4-4)$$

For the 3D  $\mathbf{k}$ -sum we use a  $(47 \times 47 \times 31)$ -point  $\mathbf{k}$  mesh for the ARPES-derived model in the one-Fe Brillouin zone (1Fe-BZ); we interpolate the static noninteracting susceptibility  $\chi_{\ell_1\ell_2\ell_3\ell_4}^0(\mathbf{q}, \omega = 0)$  from directly calculated susceptibility values on a  $(20 \times 20 \times 8)$ -point  $\mathbf{q}$  mesh in the 1Fe-BZ to perform the expensive numerical calculation with a fine patched Fermi surface in solving the pairing eigenvalue problem. Within the random-phase approximation (RPA) we define the spin-fluctuation ( $\chi_1^{\text{RPA}}$ ) and orbital-fluctuation ( $\chi_0^{\text{RPA}}$ ) parts of the RPA susceptibility as

$$\chi_{1,\ell_1\ell_2\ell_3\ell_4}^{\text{RPA}}(\mathbf{q}, \omega) = \{\chi^0(\mathbf{q}, \omega)[1 - \bar{U}^s \chi^0(\mathbf{q}, \omega)]^{-1}\}_{\ell_1\ell_2\ell_3\ell_4}, \quad (4-5)$$

$$\chi_{0,\ell_1\ell_2\ell_3\ell_4}^{\text{RPA}}(\mathbf{q}, \omega) = \{\chi^0(\mathbf{q}, \omega)[1 + \bar{U}^c \chi^0(\mathbf{q}, \omega)]^{-1}\}_{\ell_1\ell_2\ell_3\ell_4}, \quad (4-6)$$

such that the RPA-enhanced spin susceptibility is then given by the sum

$$\chi_s(\mathbf{q}, \omega) = \frac{1}{2} \sum_{\ell_1 \ell_2} \chi_{1, \ell_1 \ell_1 \ell_2 \ell_2}^{\text{RPA}}(\mathbf{q}, \omega). \quad (4-7)$$

The interaction matrices  $\bar{U}^s$  and  $\bar{U}^c$  in orbital space have matrix elements consisting of linear combinations of the interaction parameters, and their explicit forms are given, e.g., in Ref. [77].

Next, we define the singlet pairing vertex in band space,

$$\Gamma_{ij}(\mathbf{k}, \mathbf{k}') = \text{Re} \sum_{\ell_1 \ell_2 \ell_3 \ell_4} a_{\nu_i}^{\ell_1, *}(\mathbf{k}) a_{\nu_i}^{\ell_4, *}(-\mathbf{k}) \times [\Gamma_{\ell_1 \ell_2 \ell_3 \ell_4}(\mathbf{k}, \mathbf{k}', \omega = 0)] a_{\nu_j}^{\ell_2}(\mathbf{k}') a_{\nu_j}^{\ell_3}(-\mathbf{k}'), \quad (4-8)$$

where  $\mathbf{k} \in C_i$  and  $\mathbf{k}' \in C_j$  are quasiparticle momenta restricted to the electron or hole Fermi-surface sheets  $C_i$  and  $C_j$  and  $\nu_i$  and  $\nu_j$  are the band indices of these Fermi-surface sheets. The vertex function in orbital space  $\Gamma_{\ell_1 \ell_2 \ell_3 \ell_4}$  describes the particle scattering of electrons in orbitals  $\ell_2, \ell_3$  into  $\ell_1, \ell_4$  which is given by the RPA in the fluctuation exchange formalism [186] as

$$\Gamma_{\ell_1 \ell_2 \ell_3 \ell_4}(\mathbf{k}, \mathbf{k}', \omega) = \left[ \frac{3}{2} \bar{U}^s \chi_1^{\text{RPA}}(\mathbf{k} - \mathbf{k}', \omega) \bar{U}^s + \frac{1}{2} \bar{U}^s - \frac{1}{2} \bar{U}^c \chi_0^{\text{RPA}}(\mathbf{k} - \mathbf{k}', \omega) \bar{U}^c + \frac{1}{2} \bar{U}^c \right]_{\ell_1 \ell_2 \ell_3 \ell_4}. \quad (4-9)$$

The superconducting gap can be factorized into an amplitude  $\Delta(T)$  and a normalized symmetry function  $g(\mathbf{k})$ . Near  $T_c$ , the pairing symmetry function  $g(\mathbf{k})$  is the stable solution maximizing the dimensionless pairing strength functional [131]  $\lambda[g(\mathbf{k})]$ , which determines  $T_c$ . Via the variational method, this is equivalent to solving an eigenvalue problem of the form

$$-\frac{1}{V_G} \sum_j \oint_{C_j} \frac{dS'}{|\mathbf{v}_{F_j}(\mathbf{k}')|} \Gamma_{ij}(\mathbf{k}, \mathbf{k}') g_\mu(\mathbf{k}') = \lambda_\mu g_\mu(\mathbf{k}), \quad (4-10)$$

where  $V_G$  is the volume of 1Fe-BZ,  $\mathbf{v}_{F_j}(\mathbf{k}) = \nabla_{\mathbf{k}} E_j(\mathbf{k})$  is the Fermi velocity on a given Fermi sheet and  $dS$  is the area element of the Fermi sheet. The eigenfunction  $g_\mu(\mathbf{k})$  corresponds to the  $\mu$ th eigenvalue  $\lambda_\mu$  and gives the structure of the gap at the transition.

Defining  $\mathbf{k}_\perp = (k_\perp, \phi, 0)$  in the cylindrical coordinates  $\mathbf{k} = (k_\perp, \phi, k_z)$  and using  $\frac{dS}{|v_F(\mathbf{k})|} = \frac{k_\perp^2}{|k_\perp \cdot v_F(\mathbf{k})|} d\phi dk_z$  is convenient for discretizing the Fermi sheet in parameter form  $k_\perp = k_\perp(\phi, k_z)$  into small patches [187]. A dense  $(24 \times 12)$ -point mesh in parameter space  $\{\phi\} \otimes \{k_z\}$  is used for each Fermi pocket in numerical calculations, implying altogether  $n_k \sim 2500$   $\mathbf{k}$  points distributed on all Fermi pockets. After choosing the lattice constant  $a$  as the length unit, eV as the energy unit, and  $aeV/\hbar$  as the velocity unit, the eigenvalue problem Eq. (4–10) reads

$$-\frac{1}{16\pi^3} \sum_j \oint_{C_j} \Gamma_{ij}(\mathbf{k}, \mathbf{k}') \frac{k_\perp'^2 d\phi' dk_z'}{|k_\perp' \cdot v_F(\mathbf{k}')|} g_\mu(\mathbf{k}') = \lambda_\mu g_\mu(\mathbf{k}), \quad (4-11)$$

where the normalized<sup>2</sup> eigenfunctions  $g_\mu(\mathbf{k})$  are solved numerically by transforming the integration kernel (for all Fermi sheets  $C_i$ ) into an  $n_k \times n_k$  matrix. Here, we have used the symmetric pairing vertex  $\Gamma_{ij} \equiv \frac{1}{2}[\Gamma_{ij}(\mathbf{k}, \mathbf{k}') + \Gamma_{ij}(\mathbf{k}, -\mathbf{k}')]$  for a spin-singlet pairing state since we want to first examine whether the unconventional superconducting state of the LiFeAs compound and other Fe-based superconductors is universal and can be explained in the same antiferromagnetic spin-fluctuation theory before any consideration of triplet pairing or other approaches.

## 4.4 Results for the Pairing State

### 4.4.1 Results for the ARPES-Derived Fermi Surface

We now present our solutions to Eq. (4–11) for the leading pairing eigenvectors (gap functions). For this work we fix Hubbard-Hund parameters  $U = 0.75$  eV and  $J = 0.37U$  and assume spin-rotational invariance to determine  $U'$  and  $J'$ . These parameters are relatively standard in the literature making use of the RPA approach to the pairing vertex, and we found that changing them within a limited range does not change the qualitative aspects of our results for the superconducting state. The RPA

---

<sup>2</sup> The normalization is chosen so that  $\frac{1}{V_G} \sum_j \oint_{C_j} \frac{dS'}{|v_{Fj}(\mathbf{k}')|} [g_\mu(\mathbf{k}')]^2 = 1$ .

susceptibility then shows an enhanced incommensurate peak around  $\mathbf{q} = \pi(1, 0.075, q_z)$  [Fig. 4-3 (c)] or  $\mathbf{q} = \pi(1, 0.175, q_z)$  [Fig. 4-3 (g)],<sup>3</sup> and the peak decreases weakly from  $q_z = 0$  to  $q_z = \pi$ . The most important result as shown in Figs. 4-3(b) and 4-3(f) and in another representation in Figs. 4-3(d) and 4-3(h) is that, using the ARPES-based band structure for both fillings considered, we find an  $s_{\pm}$ -wave state with anisotropic but full gaps on the electron (negative gap) and hole (positive gap) pockets. The other leading eigenvalue corresponds in both cases to a  $d_{xy}$ -wave state which is closely competing [131] but is inconsistent with experiments, such that we do not investigate it further here.

If we now consider the gap functions found on the various pockets in detail, we notice a number of striking similarities to the experimental results sketched in Fig. 4-2. The full details of the  $s_{\pm}$  gap functions obtained are shown in Figs. 4-3(b) and 4-3(f) and 4-3(d) and 4-3(h), but for the reader wishing a more concise summary, we have shown in Fig. 4-5 a schematic comparison of the calculated gaps of the  $s_{\pm}$  states found at  $k_z = \pi$  versus the experimental data, using the angle convention defined in Fig. 4-2. Taking first the large  $\beta$  and  $\gamma$  pockets, we see from Fig. 4-5 that the average gap magnitude is larger on the  $\beta$  pockets by a factor of 2 or so compared to  $\gamma$ , and the average gap on the inner  $\beta$  pocket is about 20% larger than that on the outer  $\beta$  pocket, as in experiment. The gaps on  $\gamma$  and  $\beta$  pockets exhibit significant anisotropy. The minima and maxima on the  $\gamma$  pocket are at the same angular positions as in experiment, and are similar to those from the DFT-based model discussed in the Appendix A.1. These gap minima are particularly important as they will determine the momenta of the quasiparticles which dominate low-temperature measurements *if*, as seen in ARPES, the gap on  $\gamma$  is the smallest for this system. Their location along the

---

<sup>3</sup> In Fig. 4-3(g) for filling  $n = 5.90$ , another peak in the total magnetic susceptibility is at  $\mathbf{q} = \pi(0.8, 0, q_z)$ .

Fe-Fe bond direction (or the equivalent plane in  $\mathbf{k}$  space) is consistent with ARPES measurements [123, 124] as well as with the quasiparticle interference [126] and scanning tunneling microscopy experiments [127], according to the interpretation of the latter provided in Ref. [182]. The gap oscillations on the  $\beta$  pockets are in good agreement with experiment on the  $d_{xy}$ -orbital-dominated inner sheets but are apparently  $180^\circ$  out of phase with experimental results on the outer electron sheets. We comment on the origin of this discrepancy below.

We now discuss the gaps on the  $\alpha$  hole pockets. ARPES [123] sees only one band crossing the Fermi level very close to  $Z$ , with a large gap of order 6 meV, which we assign to  $\alpha_2$ . In our current tight-binding band, which obeys the symmetries of the nonrelativistic DFT approach, we have always two  $\alpha$  pockets or none, as mentioned above. It may therefore be roughly appropriate to speak of an average gap on the  $\alpha_{1,2}$  pockets in the first analysis. Within our calculation with the ARPES-derived band structure, the largest discrepancy with experiment is seen for our  $n = 6.00$  calculation, where the  $\alpha$  gap is found to be the smallest of all the gaps in the problem. In the hole-doped case  $n = 5.90$ , the size of the gap on  $\alpha_1$  increases significantly, becoming comparable to experiment, but the gap on  $\alpha_2$  remains small. It is interesting to note that the DFT calculation (Appendix A.2), while disagreeing with ARPES on the existence of a  $\Gamma$ -centered hole pocket, produces a large gap on both  $\alpha_1$  and  $\alpha_2$ .

#### 4.4.2 Analysis of Gap Sizes in Terms of Pairing Vertex

To analyze the origin of the remaining discrepancies with experiment, we investigate the structure of the effective pairing vertex by presenting in Fig. 4-6 a graphical representation of the pairing vertex  $\Gamma_{ij}(\mathbf{k}, \mathbf{k}')$  matrix. Each block  $(i, j)$  in the image represents a matrix  $(\mathbf{k}, \mathbf{k}')$  consisting of entries which correspond to the vertex  $\Gamma_{ij}(\mathbf{k}, \mathbf{k}')$  with  $\mathbf{k} \in C_i$  and  $\mathbf{k}' \in C_j$ . The majority orbital characters along the Fermi surfaces  $C_i$  are also indicated in the Fig. 4-6. In the tables below the plots, the densities of states

summed over 3D pockets and scattering vertex components averaged over  $(\mathbf{k}, \mathbf{k}')$  on the  $k_z$  cut are also shown.

For both dopings shown, the brightest set of blocks is that representing scattering processes among the three largest pockets,  $\gamma, \beta_{\text{in,out}}$ . On average, it is clear visually in Fig. 4-6 and also from the integrated intensities that the dominant scattering processes within this set of pockets occur for  $\gamma$ - $\beta_{\text{in}}$  and  $\gamma$ - $\gamma$  and, to a lesser extent,  $\gamma$ - $\beta_{\text{out}}$ .

There are several interesting conclusions to be drawn from this simple observation. First, one of the crucial differences between LiFeAs and the “canonical” 1111 systems which were originally used to deduce general principles about pairing in the Fe-based superconductors is the existence of a pocket ( $\gamma$ ) with very large density of states (Fig. 4-6) of dominant  $d_{xy}$  character. This pocket nests very poorly with the  $\beta$  pockets, as pointed out in Ref. [119], but nevertheless produces the primary pairing interaction leading to superconductivity in part due to the unusually large  $d_{xy}$  content of the  $\beta$  pockets in the ARPES-derived bandstructure. This is entirely consistent with the suggestion that while long-range magnetism is suppressed by the lack of nesting (although this effect need not rely exclusively on states exactly at the Fermi level), strong magnetic fluctuations remain and are available for pairing, which is of  $s_{\pm}$  character because the  $\gamma$ - $\beta$  interactions are repulsive. It is interesting to note that while the pair scattering processes connecting the  $\gamma$  pockets to the rest of the Fermi surface are large, the gap on the  $\gamma$  pocket itself is not. This is a consequence, within the theory of multiband superconductivity, of the large density of states on the  $\gamma$  pocket, as discussed in Chapter 4.4.3.

Second, we note that the intraband scattering  $\gamma$ - $\gamma$  is also quite strong. These are small- $\mathbf{q}$  processes which may be responsible for the tendency to ferromagnetism seen in these systems.<sup>4</sup> Although we do not see enhancement of the *total* magnetic

---

<sup>4</sup> B. Büchner (unpublished).

susceptibility near  $\mathbf{q} = 0$  (Fig. 4-3), there are evidently intraorbital susceptibilities including  $\chi_{xy,xy,xy,xy}$  which are large at small  $\mathbf{q}$ , and the partial density of states  $N_\gamma(0)$  is the largest among all pockets.

Finally, we note that the strong angular dependence of the vertex is induced by the variation of the orbital content in general, and the  $d_{xz}/d_{yz}$  content in particular. As discussed in Refs. [188] and [77], there is a strong tendency for pair scattering between like orbitals to be enhanced, other effects being equal, accounting for the large  $\gamma$ - $\beta_{in}$  scattering. But even in this case subdominant  $xz/yz$  orbitals are present on the  $\beta_{in}$  sheets which lead to the observed modulation via the matrix elements which occur in Eq. (4-8).

To understand the angular oscillations within a phenomenological picture, Maiti *et al.* [189] fitted the gaps on the electron pockets measured by Umezawa *et al.* [124] with the angle dependence

$$\Delta_{inner}(\theta) = \Delta_0(1 + r_2|\cos 2\theta| + r_4 \cos 4\theta), \quad (4-12)$$

$$\Delta_{outer}(\theta) = \Delta_0(1 - r_2|\cos 2\theta| + r_4 \cos 4\theta), \quad (4-13)$$

where  $\theta$  is defined in the caption of Fig. 4-2 (measured from dashed-line direction), and they found (i)  $r_2 > 0$  and (ii)  $r_4 > \frac{1}{4}r_2$ . Point (i) is equivalent to  $\Delta_{inner} > \Delta_{outer}$ , which is measured by both ARPES experiments, and our results from both tight-binding models also agree with point (i). Point (ii) is related to the in-phase feature and the orientation of gap maxima on both pockets because, first, at  $\theta = 0$ ,  $d\Delta_{inner}/d\theta = 0$  and  $d\Delta_{outer}/d\theta = 0$  and, second,  $d^2\Delta_{inner}/d\theta^2 = -4(r_2 + 4r_4)$  and  $d^2\Delta_{outer}/d\theta^2 = 4(r_2 - 4r_4)$ .  $r_4 > \frac{1}{4}r_2$  means both inner and outer pockets have maxima at  $\theta = 0$ , and hence they are in phase. Considering  $r_2 > 0$  and the gap on the outer pocket oscillates stronger than the inner pocket (larger curvature at  $\theta = 0$ ) in our results, a reasonable range for  $r_4$  at all  $k_z$  is  $r_4 \sim -\frac{1}{4}r_2$ . The sign of  $r_2$  is determined by the angle dependence of the pairing interaction and is positive in the case where the interaction between electron and hole

pockets is dominant [189]. Our numerical results suggest the same conclusion as the ARPES experiments. The discrepancy in the phase of the oscillations on the outer  $\beta$  pocket is attributable to the “wrong” sign of the more sensitive parameter [189]  $r_4$  obtained within our calculations.

We now turn to the more delicate issue of the pairing-vertex components connecting the  $\alpha$  pockets to the rest of the Fermi surface. It is clear from both the plots and table corresponding to Figs. 4-6(a) and 4-6(b) that these are negligible in the compensated case  $n = 6.00$ , in Fig. 4-6(a) simply because  $H_0^{\text{ARPES}}$  contains no  $\alpha$  pockets at  $k_z = 0$ , and in Fig. 4-6(b) because the densities of states on these closed 3D pockets are extremely small. In 2D models, where densities of states tend to be weakly dependent on pocket size, these effects are suppressed. We discuss the connection of the small gap on the  $\alpha$  pockets to the corresponding components of the vertex below. For the moment, we note simply that the effect of hole doping to  $n = 5.90$  shown in Figs. 4-6(c) and 4-6(d) clearly enhances the scattering of pairs on the  $\alpha$  pockets to the  $\beta$  pockets, particularly to  $\beta_{\text{in}}$ . As seen in Figs. 4-3(a) and 4-3(e), hole doping by a small amount (5% Fe) transforms the small  $Z$ -centered  $\alpha$  pockets into two narrow concentric tubes and thereby enhances the DOS on the  $\alpha$  pockets. While the  $n = 5.90$  case is nominally inconsistent with the ARPES observation of no  $\alpha$ -type Fermi surfaces at  $k_z = 0$ , it is clear that the determination of the hole dispersion near  $\Gamma$ - $Z$  becomes quite challenging when the bands are grazing the Fermi level. It is significant that the results for the DFT analysis given in Appendix A.2 also give large gaps on the  $\alpha$  pockets, although the Fermi surface of the hole pockets disagrees qualitatively with ARPES. Taken together, these results suggest that the  $\alpha$ - $\beta$  interaction is enhanced and the gap on the  $\alpha$  pocket is large only if states near  $\Gamma$  of  $xz/yz$  character contribute strongly to pairing. This occurs when the Fermi surface includes an open (cylindrical)  $\alpha_1$  pocket and also when the range of pairing is expanded to include states away from the Fermi level, as discussed below.

### 4.4.3 Discussion: Toy Model for Gap Sizes

To understand the relative sizes of the gaps on the various Fermi surface sheets, one needs to combine knowledge of the pairing vertex function discussed above with the densities of states on each sheet. Here, a simplified picture can help us understand why certain gaps are large and others are small. We neglect for this discussion the momentum dependence of the gap eigenfunctions, densities of states, and vertices over the individual Fermi surface sheets. If we are primarily interested in gap *sizes*, a good approximation to the gap equation (4–11) is then given by

$$\lambda g_i \approx \sum_j -g_j N_j \Gamma_{ij}, \quad (4-14)$$

where  $g_i$  now denotes the gap and  $N_i$  the density of states at the Fermi level in the  $i$ th band. We begin by discussing the question of how the gap on tiny  $Z$ -centered (or  $\Gamma$ -centered) hole pockets can become large, as seen by ARPES [123]. Were intraband scattering processes dominant, the tiny DOS on the  $\alpha$  pockets would generically create an extremely small gap. Since interband scattering is more important, in the situation where the DOS on the  $\alpha$  pockets is small, the gap on  $\alpha$  will be determined by scattering from the other major bands, in particular  $\gamma$  and  $\beta_{\text{in,out}}$  as seen in Fig. 4-6.

In such a situation, we have approximately

$$\lambda g_\alpha \approx -g_\gamma N_\gamma \Gamma_{\alpha\gamma} - \sum_\nu g_{\beta_\nu} N_{\beta_\nu} \Gamma_{\alpha\beta_\nu}, \quad (4-15)$$

where  $\nu$  sums over both inner and outer  $\beta$  pockets. Since the state is an  $s_\pm$  state driven by repulsive interband interactions, the first and second terms tend to cancel each other. Large gaps can then be obtained if parameters are chosen such that the contribution from the  $\gamma$  pocket is minimized. As we have seen above, however, in the current ARPES-derived model, while the scattering of  $\alpha$  states to the  $\beta$  pockets is much stronger, the  $\gamma$  density of states is significantly larger, such that the two terms in Eq. (4–15) are comparable and therefore mostly cancel each other. As can be seen by

comparing the hole-doped case with the compensated case with the tables for  $\Gamma_{\mu\nu}$  in Fig. 4-6, the main effect of the hole doping on the balance of the two terms in Eq. (4-15) is due to the enhancement of  $\Gamma_{\alpha,\beta_{in}}$  by a factor of 2.

## 4.5 Conclusions

We have performed 3D calculations of the superconducting pair state in the LiFeAs compound, one of the few materials where ARPES experiments indicate significant gap anisotropy, possibly due to reduced diffuse scattering from the very clean, nonpolar surface. Since the inner hole pockets of the Fermi surface of this material are thought to be strongly renormalized by interactions, we used as the input a tight-binding model fit to ARPES data reproducing both the band structure and orbital polarization measurements at the Fermi surface. Our calculations find a gap structure which changes sign between the hole and electron pockets and reproduce semiquantitatively the relative gap sizes on the three largest pockets, along with the oscillatory behavior seen. We performed a careful analysis of the structure of the pair-scattering vertex to understand the structure of these pair states. The gap function observed by ARPES on the main pockets can then be understood entirely in terms of the repulsive interband interactions within the spin-fluctuation approach. On the outer electron pocket, a difference in the sign of the oscillations with respect to experiment can be traced to a term in the phenomenology of Maiti *et al.* [189] which depends very sensitively on the balance between intra- and interpocket interactions.

Our results differ from experiment in one important respect, namely the small size of the gap on the inner hole ( $\alpha$ ) pockets we find, in contrast to the large gap observed in Ref. [123]. We have discussed here, and in Appendices A and B, various model Fermi surfaces which tend towards giving significantly larger  $\alpha$  gaps and deduced that inclusion of the  $xz/yz$  states in the pairing near the  $\Gamma$  point of the Brillouin zone appears to be essential. While these models do not appear to be fully consistent with the Fermi surface found by ARPES, they point the way towards identifying missing ingredients in

the theory. In particular, since the  $\alpha$  pockets in this material are tiny and very close to a Lifschitz transition, it may be necessary in this system to account for states slightly away from the Fermi level in order to reproduce the overall gap structure.

Due to the remarkable agreement of the robust part of the gap structure on the main pockets, we conclude that the pairing in LiFeAs has essentially the same origin as in other Fe-based superconductors, despite the fact that there is no nesting apparent at the Fermi surface. We point out that the main difference between LiFeAs and the paradigmatic 1111 systems is the predominance of the scattering between the hole  $\gamma$  Fermi pocket and the electron  $\beta$  pockets, all of which have substantial  $xy$  orbital character; pure  $xz/yz$  scattering is subdominant. A strong  $d_{xy}$  intrapocket interaction may explain the ferromagnetic correlations observed in experiment, despite the lack of a  $\mathbf{q} = 0$  peak in the total magnetic susceptibility.

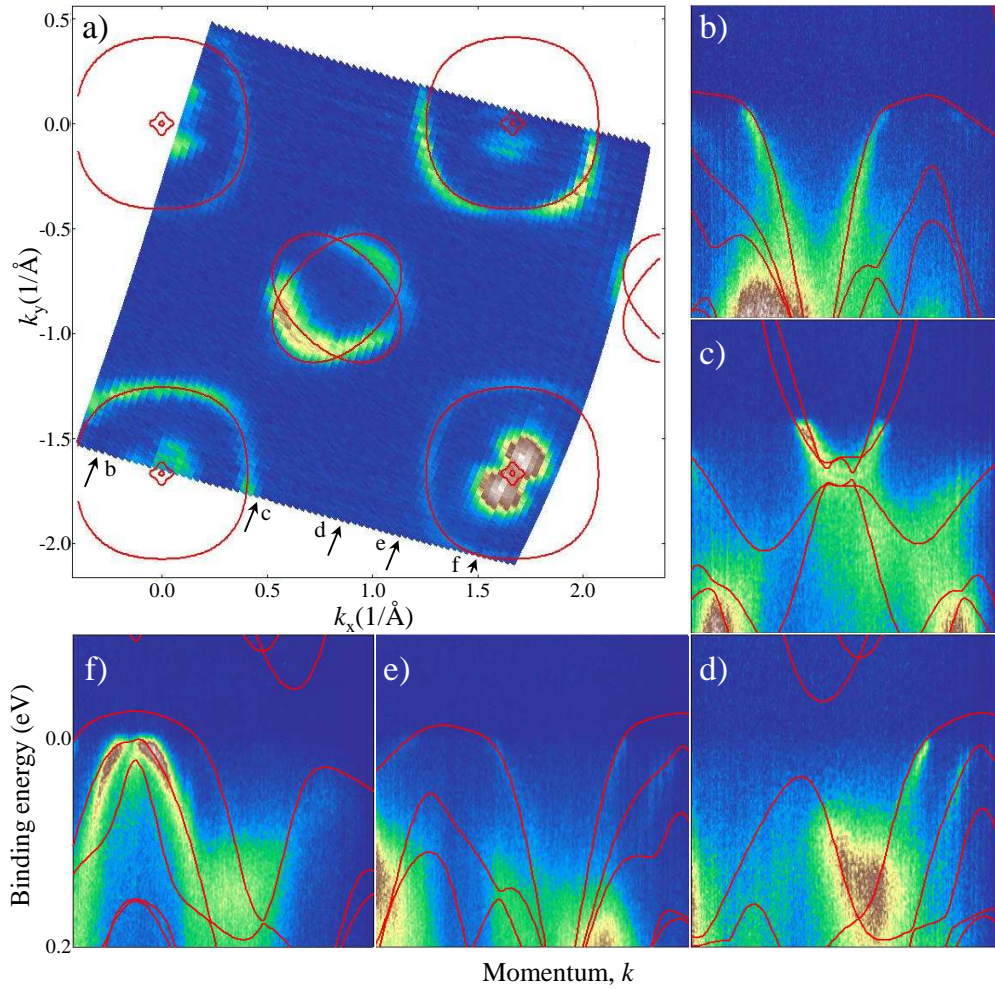


Figure 4-1. Comparison of the tight-binding bands and ARPES data both (a) at the Fermi surface and (b)–(f) in energy–momentum cuts for  $k_z = \pi/2$ . The black arrows in (a) denote the positions of several representative energy momentum cuts. For demonstration purposes Borisenko *et al.* [125] used one of the high-quality Fermi-surface maps from Ref. [123], although to recover additional information on  $k_z$  dispersion more data with various  $h\nu$  were used. For further details see Appendix B.

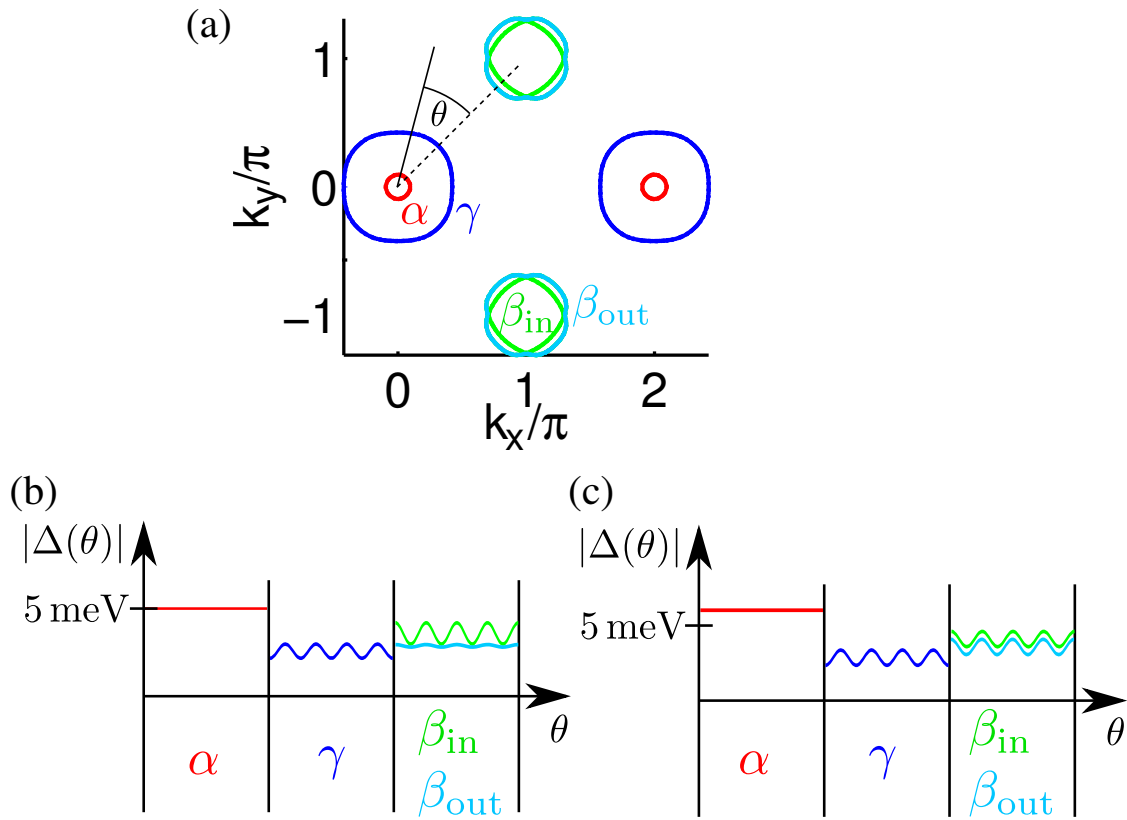


Figure 4-2. (a) The cut of the Fermi surface of the ARPES-derived tight-binding model (filling  $n = 6.00$ ) at  $k_z = \pi$  to show the definition of the various pockets and the angle  $\theta$  that parametrizes the surface points. Sketch of the results of the gap  $|\Delta(\theta)|$  as seen in recent ARPES experiments compiled from the fits provided in (b) Ref. [124] and (c) Ref. [123].

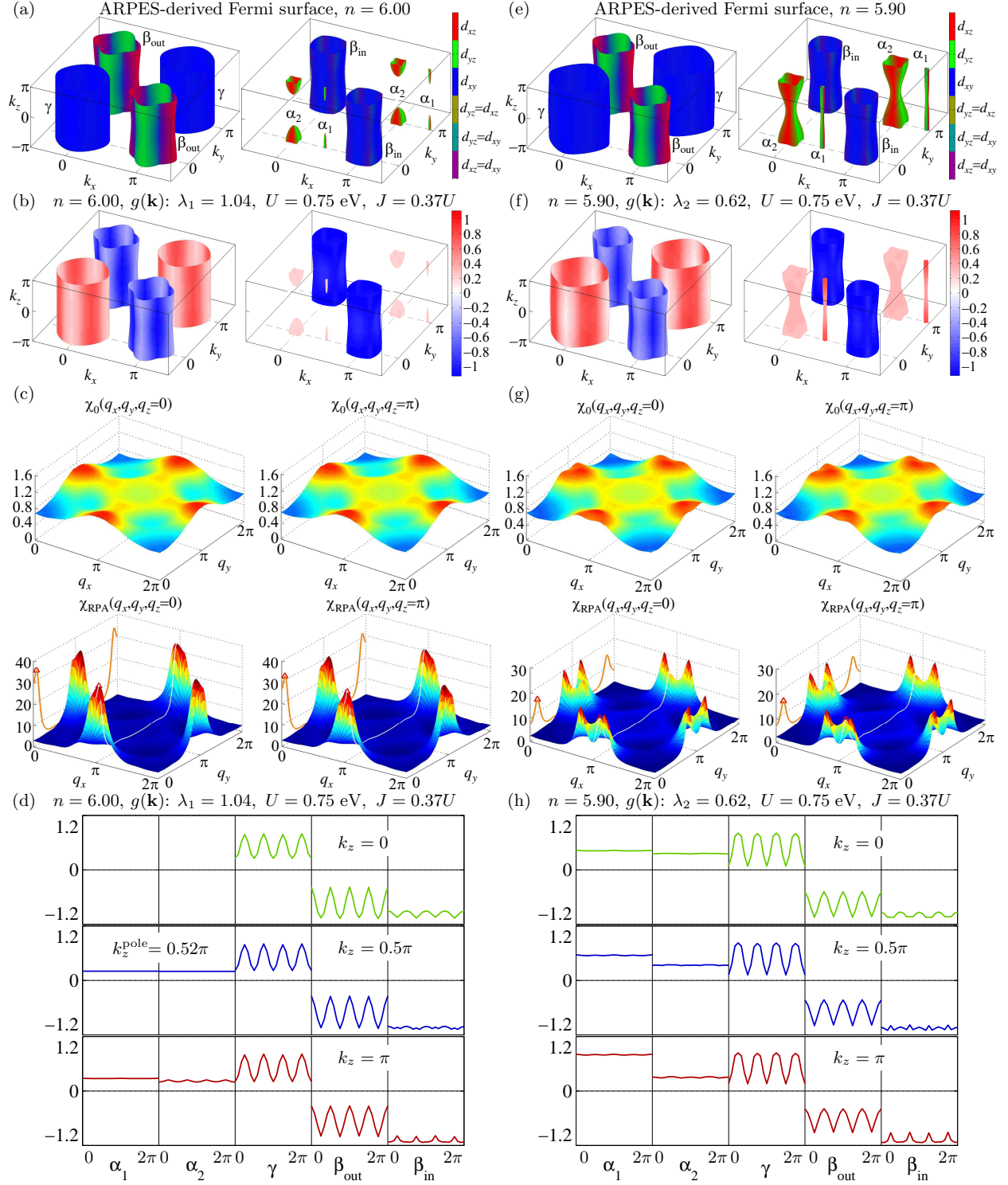


Figure 4-3. Fermi surface of LiFeAs from  $H_0^{\text{ARPES}}$  at (a) filling  $n = 6.00$  and (e)  $n = 5.90$  plotted in the coordinates of the one-Fe Brillouin zone as two sets, outer (left) and inner (right) pockets. Majority orbital weights are labeled by colors, as shown. Note the small innermost, hole pocket  $\alpha_1$  with rotation axis  $\Gamma$ - $Z$  ( $M$ - $A$ ) has been artificially displaced from its position along the  $k_x$  axis for better viewing in (a) and (e). (b) and (f) are the gap symmetry functions  $g(\mathbf{k})$  corresponding to the leading eigenvalues ( $s_{\pm}$  wave) and interaction parameters shown in the figure. (c) and (g) are the corresponding noninteracting spin susceptibility and RPA spin susceptibility at  $q_z = 0, \pi$ . In the RPA susceptibility plot, a thin white line is plotted along the path  $(\pi, q_y, q_z = 0)$  or  $(\pi, q_y, q_z = \pi)$ , its projection on the  $q_y$ - $\chi_s$  plane is plotted as a thick orange line, and the red triangle indicates the peak position. (d) and (h) are the angle dependence of  $g(\mathbf{k})$  on the pockets indicated at  $k_z = 0, 0.5\pi, \pi$ . In (d) the gap value on  $\alpha$  pockets at the pole is plotted since these pockets do not extend to  $k_z = 0.5\pi$ .

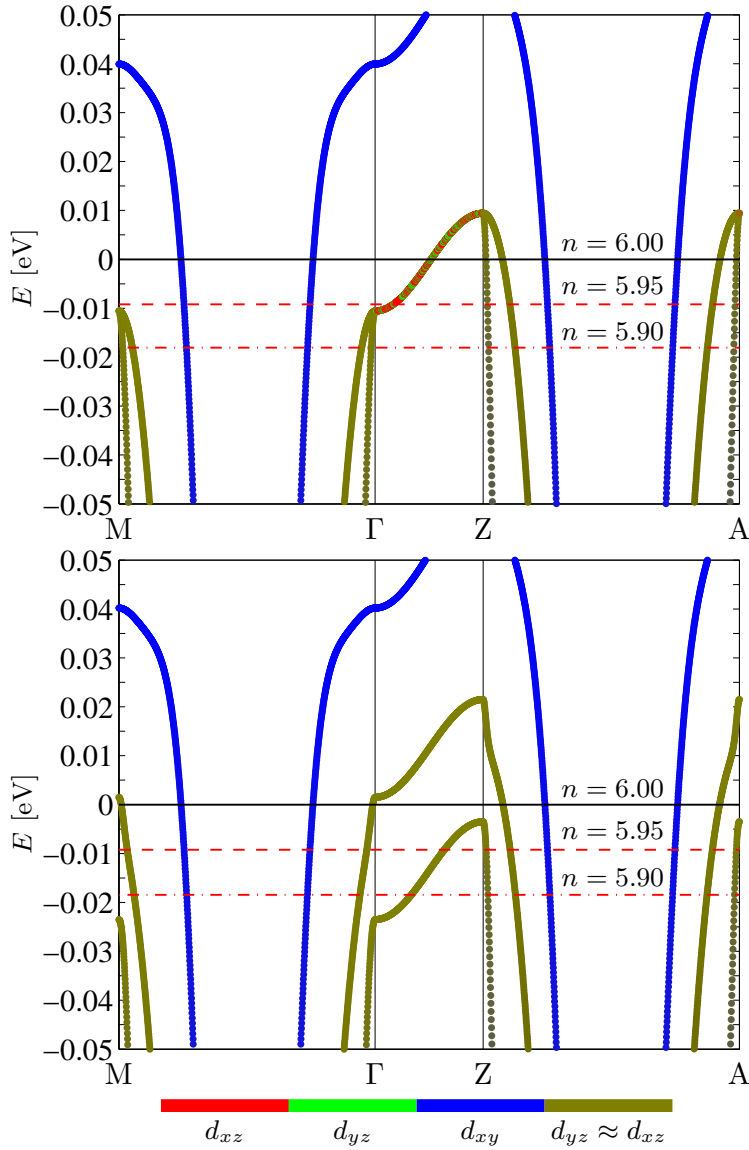


Figure 4-4. The band structures along the  $M-\Gamma-Z-A$  path in the one-Fe Brillouin zone for (top) the ARPES-derived model and (bottom) the same model with the approximate spin-orbit coupling term [190]  $\lambda_{\text{Fe}}^{3d} \sum_i L_i^z S_i^z$ , with  $\lambda_{\text{Fe}}^{3d} = 0.025$  eV. The color encodes the major orbital characters, as indicated by the horizontal color bar. The dashed lines mark the corresponding Fermi energy at filling  $n = 6.00$ ,  $5.95$ , and  $5.90$ .

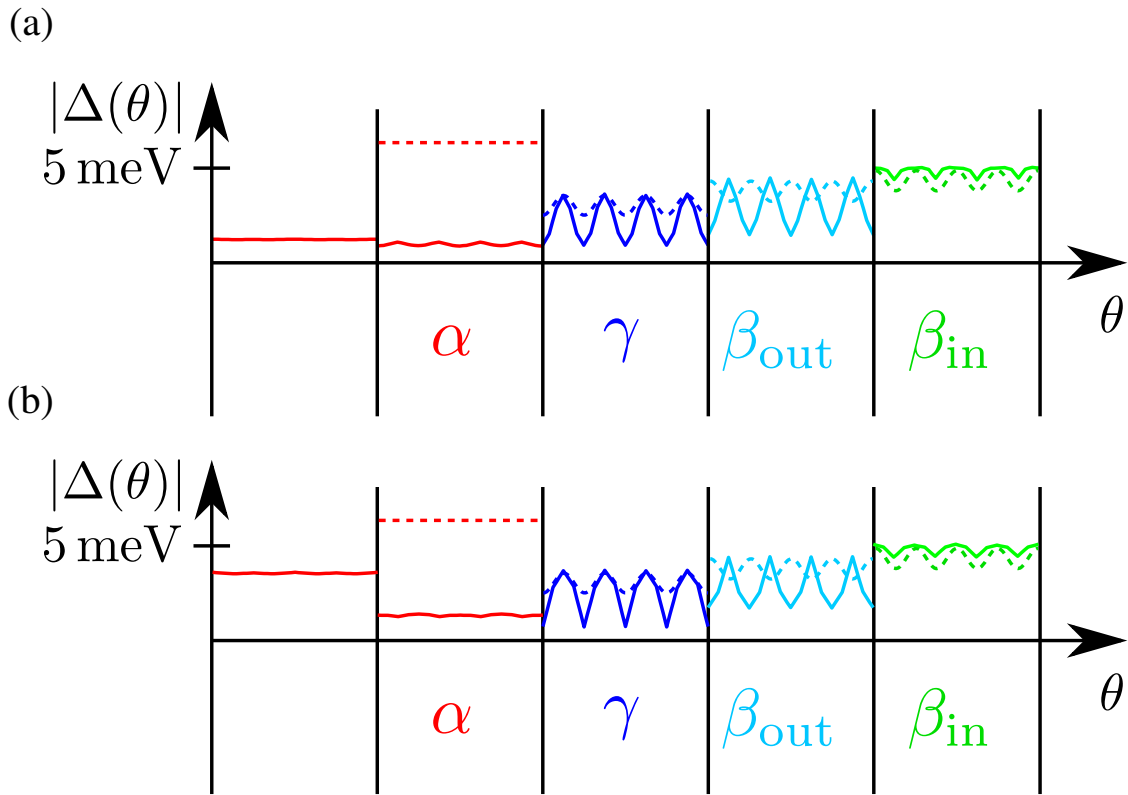


Figure 4-5. Comparison between the gap function predicted in the present work (solid lines) at  $k_z = \pi$  and the experimental findings of  $|\Delta(\theta)|$  from Ref. [123] (dashed lines). Result of the ARPES-derived model at (a) filling  $n = 6.00$  and (b) at filling  $n = 5.90$ .

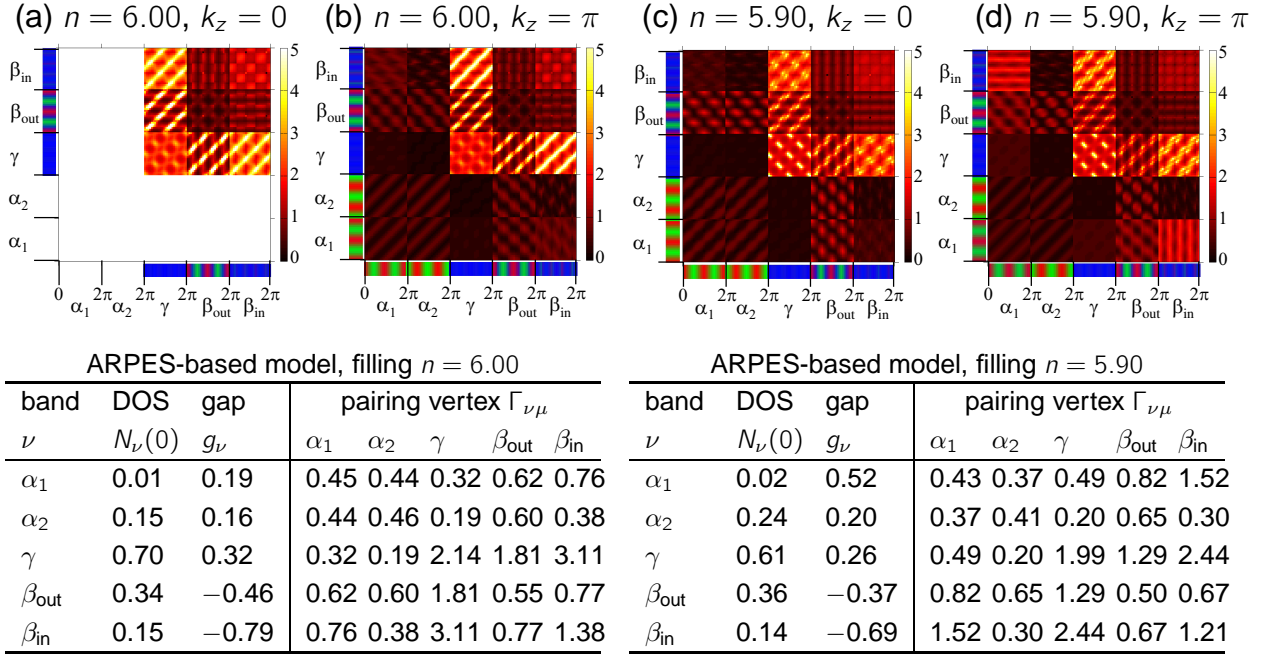


Figure 4-6. Components of the pairing vertex  $\Gamma_{ij}(\mathbf{k}, \mathbf{k}')$  matrix resulting in the pairing function plotted in Fig. 4-3, from ARPES-based model at (a) and (b) filling  $n = 6.00$  and (c) and (d) filling  $n = 5.90$ , where the value is proportional to the brightness of the color. The rows and columns of the tiles of (a)–(d) correspond to Fermi points  $\mathbf{k} \in C_i$  and  $\mathbf{k}' \in C_j$  where  $C_{i,j}$  are the  $k_z$  cuts of Fermi sheets  $\alpha_{1,2}, \gamma$  at  $\Gamma$  and  $\beta_{\text{out}}, \beta_{\text{in}}$  at the  $X$  point. Here  $k_z = k'_z = 0$  for (a) and (c) and  $k_z = k'_z = \pi$  for (b) and (d). The angular dependence of the major orbital characters of these Fermi points are labeled by color as  $d_{xz}$  (red),  $d_{yz}$  (green), and  $d_{xy}$  (blue), as shown in the horizontal and vertical color bars attached to each panel. The tables show the density of states summed over three dimensions (3D DOS), the angular averaged pairing vertex  $\Gamma_{\nu\mu} \equiv \sum_{\mathbf{k}, \mathbf{k}'} \Gamma(\mathbf{k}, \mathbf{k}') / n_{\mathbf{k}} / n_{\mathbf{k}'}$  at  $k_z = \pi$  (where  $n_{\mathbf{k}}$  is the number of  $\mathbf{k}$  points in the sum), and the approximated model gap solved from linearized gap equations using the 3D DOS and angular averaged pairing vertex at  $k_z = \pi$ .

## CHAPTER 5 FINAL CONCLUSIONS

In this work we have explored the gap symmetry and gap structure in Fe-based superconductors by theoretical calculations that account for different experiments. We have considered the low energy excitations in a superconducting state including the possibility of gap nodes (Volovik effect in the magnetic field dependence of the specific heat coefficient of optimally doped  $\text{BaFe}_2(\text{As}_{1-x}\text{P}_x)_2$ ), the relation between the gap structure and extended low energy “bound” states near a single vortex core (scanning tunneling spectroscopy (STS) on  $\text{LiFeAs}$ ), the pointlike impurity effects on the superconducting transition temperature and low energy density of states ( $T_c$  suppression rate on the electron irradiated  $\text{BaFe}_2\text{As}_2$ ), and the superconducting gap magnitudes by angle-resolved photoemission (ARPES) (spin-fluctuation calculation of the gap symmetry function of  $\text{LiFeAs}$  comparing with ARPES measurements). These experiments and calculations consistently assert that the gap in Fe-based superconductors has nontrivial structure in momentum space, the fingerprint of unconventional and high temperature superconductors where “a conventional notion that the  $s$ -wave gap is nodeless, the  $d$ -wave has four nodes, etc.,” doesn’t apply [9] (see the discussion below). The antiferromagnetic spin-fluctuation pairing theory predicts anisotropic  $s_{\pm}$  gap [46] based on the nesting between the holelike and electronlike pockets connecting by  $(\pi, 0)$  wave-vector with or without nodes depending on the doping and the resulting nesting condition. Our spin-fluctuation calculation on  $\text{LiFeAs}$  [125] further affirms that the same pairing mechanism works despite a lack of good Fermi surface nesting, giving a leading  $s_{\pm}$ -wave pairing instability. However, the superconductivity in the alkali metal iron selenide family (e.g.,  $\text{K}_x\text{Fe}_{2-y}\text{Se}_2$ ; see Ref. [191] for a recent review) does stimulate more fierce debates on this pairing mechanism based on the Fermi surface nesting since there is no hole pocket at the Brillouin zone center  $\Gamma$  point [192], although a hole pocket at  $Z$  point with a nodeless

gap is found by ARPES [193]. Spin-fluctuation and functional renormalization group calculations in two dimensions predicted a nodeless  $d$ -wave gap [130, 194, 195], but later it was shown that the different crystal symmetry of the 122 compound also enforces horizontal or vertical nodal lines [196, 197] in the  $d$ -wave state, and the spin-fluctuation calculation in three dimensions [190] has found such a  $d$ -wave state is the leading instability and the nodal lines are so narrow on the Fermi surface that it may cause difficulty to measure them in experiment (for example, the aforementioned ARPES [193] found a nodeless gap on the hole pocket suggesting an  $s$ -wave state). Mazin [196] also proposed another  $s$ -wave state for antiferromagnetic spin-fluctuation pairing with only electron pockets, the bonding-antibonding  $s$ -wave state with sign change between inner and outer electron pockets in the two-Fe zone, which is explored in Refs. [190, 197] as a competing state with  $d$  wave with respect to the strength of the hybridization parameter depending on the out-plane hopping, spin-orbit coupling, etc. Finally single sign  $s_{++}$  state is another possibility when the orbital fluctuations are included as well [198]. The complexity of nodal structure in these compounds with only electron pockets requires more careful experiments to tell whether the gap is  $s$  wave or  $d$  wave or whether there exists a transition from  $s$  wave to  $d$  wave, that is, a transition from  $A_{1g}$  to  $B_{1g}$  symmetry, upon electron doping, and the experiment results will surely test the theory of the pairing mechanism.

The superconductivity in the monolayer FeSe film on SrTiO<sub>3</sub> substrate deserves further attention since it has the simplest structure while setting the record of the highest  $T_c$  of Fe-based superconductors, around 65 K observed by STS [199] and ARPES [200–202] (the *ex situ* transport measurements found  $T_c \approx 40$  K in a monolayer FeSe film covered by non-superconducting FeTe layers for protection [203]). Such a high  $T_c$  in the monolayer FeSe/SrTiO<sub>3</sub> is remarkable since the bulk FeSe has a much lower  $T_c \approx 8$  K at ambient pressure [76]. Similar to  $K_x\text{Fe}_{2-y}\text{Se}_2$ , the superconducting monolayer FeSe film has only electron pockets at the zone corner as shown by the

aforementioned ARPES experiments. The  $T_c$  defined by ARPES gap closing can be refined up to 75 K using different substrates [204, 205]. Recent ARPES experiment [206] identified in monolayer FeSe/SrTiO<sub>3</sub> the evolution of a Mott insulating parent compound to a superconductor with the increasing doping caused by different annealing sequences in vacuum, which established a closer link to cuprates. This suggests some common physics for superconductivity in cuprates and Fe-based superconductors.

To sum up, AFe<sub>2</sub>Se<sub>2</sub> and monolayer FeSe indicate the existence of more *terrae incognitae* in Fe-based superconductors. By the principle of William of Ockham, it is reasonable to believe there is a common (essential or qualitative) mechanism for different families of Fe-based superconductors which also applies to cuprates. The gap structure and gap symmetry is the fingerprint for such a mechanism while predicting new superconductors is the real touchstone for the theory of such a mechanism.

## APPENDIX A SPIN-FLUCTUATION CALCULATION FOR DFT-DERIVED FERMI SURFACE

### A.1 Electronic Structure of LiFeAs from Density Functional Theory

The band structure from DFT for the LiFeAs parent compound is calculated using the quantum ESPRESSO package. The experimentally determined lattice parameters used in the calculation are taken from Table I in Ref. [207], including lattice constants  $a = 3.7914 \text{ \AA}$ ,  $c = 6.3639 \text{ \AA}$  and the internal coordinates for the Li atoms  $z_{\text{Li}} = 0.8459$  and the As atoms  $z_{\text{As}} = 0.2635$ . Next we obtain the DFT derived ten-orbital tight-binding Hamiltonian model  $H_0^{\text{DFT}}$  by projecting the bands near the Fermi energy on the ten  $3d$ -orbitals of the two Fe atoms in the primitive cell of the LiFeAs crystal using maximally localized Wannier functions computed using the WANNIER90 package. The Fermi surface from this model is shown in Fig. A-1(a), where the colors encode the orbital character. The Fermi surface sheets of the ten-orbital model are plotted using a *repeated-zone* scheme of the two-Fe Brillouin zone (2Fe-BZ) in the coordinates  $(k_x, k_y, k_z)$  of the 1Fe-BZ, and the cube in  $\mathbf{k}$  space in Fig. A-1(a) encloses the volume of the 1Fe-BZ. This representation is convenient for later calculation since the susceptibility is only a periodic function in the 1Fe-BZ. For the convenience of later discussion, we denote the two hole pockets at the  $\Gamma(0, 0, 0)$  [or  $M(\pi, \pi, 0)$ ] point as  $\alpha_1/\alpha_2$  and two electron pockets at the  $X$  (or  $Y$ ) point as  $\beta_{\text{out}}/\beta_{\text{in}}$ . The DOS at the Fermi level is shown in Table A-1, in comparison with that of ARPES-derived model.

### A.2 Pairing State for DFT-Derived Fermi Surface

Although the Fermi surface predicted by DFT differs in some essential respects from that found in ARPES, it is nevertheless useful to calculate the gap functions which arise within the spin-fluctuation theory for this electronic structure to get a sense of how much the gap varies for small changes in the electronic structure and to compare with earlier 2D theoretical calculations using a DFT-derived Fermi surface [184]. As shown in Fig. A-1, for  $U = 0.88 \text{ eV}$  and  $J = 0.25U$ , we find an  $s_{\pm}$ -wave state ( $\lambda_1 =$

Table A-1. LiFeAs density of states (two Fe atoms, two spins) at the Fermi level from (a) the ten-orbital DFT-based model  $H_0^{\text{DFT}}$  and (b) the ARPES-based model  $H_0^{\text{ARPES}}$  along with (c) the density of states in (b) scaled by a factor  $r = 0.5$ .

|     | $\alpha_1$ | $\alpha_2$ | $\gamma$ | $\beta_{\text{out}}$ | $\beta_{\text{in}}$ | total |
|-----|------------|------------|----------|----------------------|---------------------|-------|
| (a) | 0.040      | 0.554      | 0.660    | 0.610                | 0.377               | 2.241 |
| (b) | 0.038      | 0.592      | 2.782    | 1.377                | 0.594               | 5.383 |
| (c) | 0.019      | 0.296      | 1.391    | 0.689                | 0.297               | 2.692 |

0.237) with anisotropic full gaps on the electron (negative gap) and hole (positive gap) pockets, as shown in Figs. A-1(b) and A-1(d). (The second eigenvalue  $\lambda_2 = 0.1006$  is a  $d_{x^2-y^2}$ -wave state.) The  $s_{\pm}$ -wave state is driven by the enhanced *commensurate* peak at  $\mathbf{q} = (\pi, 0, q_z)$  in the RPA susceptibility, see Fig. A-1(c). This peak value has a moderate  $q_z$  dependence and becomes smaller at  $q_z = \pi$ , which means the gap structure will not change too much along  $k_z$ .

The gaps on the hole pockets  $\alpha_2$  and  $\gamma$  exhibit moderate  $k_z$  dependence. The gap minima on the  $\gamma$  pocket are in the  $k_x, k_y$  or Fe-Fe directions. The gap on the closed  $\alpha_1$  pocket is among the largest ones, although the DOS of the  $\alpha_1$  pocket is the smallest, and this gap shows strong  $k_z$  dependence near the pole of the pocket. Next, the gaps on the inner  $\beta_{\text{in}}$  and outer  $\beta_{\text{out}}$  pockets seem to be intertwined and correlated: near  $k_z = 0$ , the gap on the inner pocket is smaller than the gap on the outer pocket, while near  $k_z = \pi$  the order is flipped [see Fig. A-1(d) for gaps at  $k_z = 0, \pi$ ], but they coincide at the points where two Fermi pockets touch each other. Last, while the gap magnitudes from our full 3D calculation are substantially similar to those obtained using 2D functional renormalization group calculations by Platt *et al.* [184] at  $k_z = 0$ , at  $k_z = \pi$  we find qualitatively different hole pocket gaps, indicating the importance of 3D pair-scattering processes.

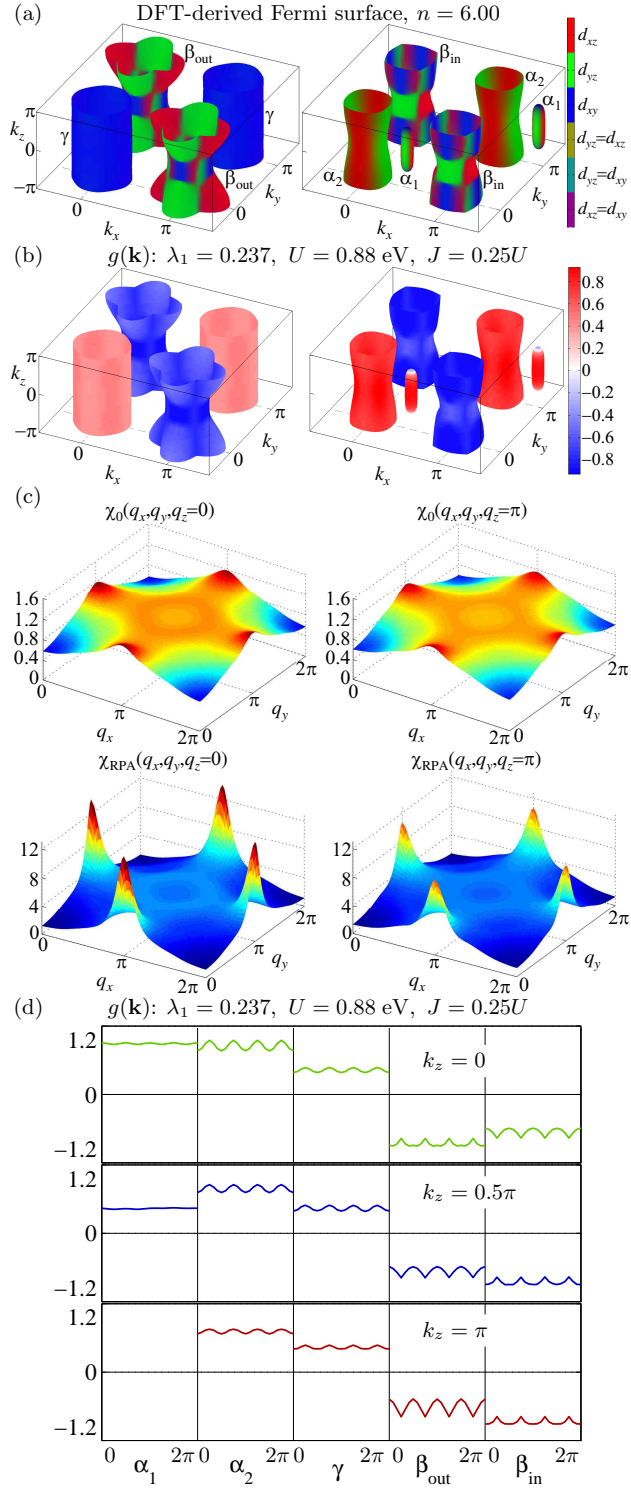


Figure A-1. (a) Fermi surface of LiFeAs from  $H_0^{\text{DFT}}$  plotted in the coordinates of the one-Fe Brillouin zone as two sets, outer (left) and inner (right) pockets. Majority orbital weights are labeled by colors as shown. Note the small innermost, hole pocket  $\alpha_1$  with the rotation axis  $\Gamma$ -Z (or  $M$ -A) has been artificially displaced from its position along the  $k_x$  axis for better viewing. (b) The gap symmetry functions  $g(\mathbf{k})$  corresponding to the leading eigenvalues ( $s_{\pm}$  wave) with interaction parameters shown in the figure. (c) The corresponding noninteracting spin susceptibility and RPA spin susceptibility at  $q_z = 0, \pi$ . (d) The angle dependence of  $g(\mathbf{k})$  on the pockets indicated at  $k_z = 0, 0.5\pi, \pi$ .

APPENDIX B  
FITTING PARAMETERS FOR TEN-ORBITAL TIGHT-BINDING MODEL  $H_0^{\text{ARPES}}$

In the following, we give the Hamiltonian matrix of the tight-binding model  $H_0^{\text{ARPES}}$  from Ref. [183] (with corrections and minor changes) and the hopping parameters  $t_{\ell\ell'}^{rst}$  which are obtained by fitting the ARPES measured band structure for LiFeAs using that tight-binding model. The hopping parameters were tuned to optimally reproduce a vast set of experimental data measured along high symmetry directions as well as complete Fermi surface maps, cutting the band structure at arbitrary angles to crystallographic axes. One such map is shown in Fig. 4-1. To pin down  $k_z$  dispersions, high symmetry cuts measured with different excitation energies were used. Here  $\ell, \ell'$  are orbital indices with  $1 = d_{xy}, 2 = d_{x^2-y^2}, 3 = id_{xz}, 4 = id_{yz}, 5 = d_{z^2}$  for the first Fe within the unit cell and  $6 = d_{xy}, 7 = d_{x^2-y^2}, 8 = -id_{xz}, 9 = -id_{yz}, 10 = d_{z^2}$  for the second Fe.  $r, s, t$  are integers denoting a hopping distance  $r\mathbf{T}_x + s\mathbf{T}_y + t\mathbf{R}_3$  where  $\mathbf{R}_1, \mathbf{R}_2, \mathbf{R}_3$  are lattice basis vectors and  $\mathbf{T}_x, \mathbf{T}_y$  are basis vectors for the one-Fe unit cell. Specifically, we have  $\mathbf{T}_x = \frac{1}{2}(\mathbf{R}_1 - \mathbf{R}_2), \mathbf{T}_y = \frac{1}{2}(\mathbf{R}_1 + \mathbf{R}_2)$ , and accordingly in the reciprocal space, we have  $k_1 = k_x + k_y, k_2 = -k_x + k_y, k_3 = k_z$ , where the wave-number components are scaled by choosing the lattice constant  $a = 1$ . The entire calculation is done with  $k_{1,2,3}$  (in 2Fe-BZ) and then plotted with  $k_{x,y,z}$  (in 1Fe-BZ using a repeated-zone scheme), such as, for example, in Fig. 4-3(a).  $H_0^{\text{ARPES}}$  is given in the block matrix form as follows:

$$H_0^{\text{ARPES}} = \begin{pmatrix} H^{++} & H^{+-} \\ H^{+-*} & H^{++*} \end{pmatrix}. \quad (\text{B-1})$$

Here an asterisk (\*) means complex conjugate. Each element of  $H^{++}, H^{+-}$  is given in two parts: the 2D part and the 3D part.

For the 2D part of the Hamiltonian,

$$H_{11}^{++} = \epsilon_1 + 2t_{11}^{11}(\cos k_1 + \cos k_2) + 2t_{11}^{20}(\cos 2k_x + \cos 2k_y),$$

$$H_{12}^{++} = 0,$$

$$\begin{aligned}
H_{13}^{++} &= 2it_{13}^{11}(\sin k_1 - \sin k_2), \\
H_{14}^{++} &= 2it_{13}^{11}(\sin k_1 + \sin k_2), \\
H_{15}^{++} &= 2t_{15}^{11}(\cos k_1 - \cos k_2), \\
H_{22}^{++} &= \epsilon_2 + 2t_{22}^{11}(\cos k_1 + \cos k_2), \\
H_{23}^{++} &= 2it_{23}^{11}(\sin k_1 + \sin k_2), \\
H_{24}^{++} &= 2it_{23}^{11}(-\sin k_1 + \sin k_2), \\
H_{25}^{++} &= 0, \\
H_{33}^{++} &= \epsilon_3 + 2t_{33}^{11}(\cos k_1 + \cos k_2) + 2t_{33}^{20} \cos 2k_x \\
&\quad + 2t_{33}^{02} \cos 2k_y + 4t_{33}^{22} \cos 2k_x \cos 2k_y, \\
H_{34}^{++} &= 2t_{34}^{11}(\cos k_1 - \cos k_2), \\
H_{35}^{++} &= 2it_{35}^{11}(\sin k_1 + \sin k_2), \\
H_{44}^{++} &= \epsilon_3 + 2t_{33}^{11}(\cos k_1 + \cos k_2) + 2t_{33}^{02} \cos 2k_x \\
&\quad + 2t_{33}^{20} \cos 2k_y + 4t_{33}^{22} \cos 2k_x \cos 2k_y, \\
H_{45}^{++} &= 2it_{35}^{11}(\sin k_1 - \sin k_2), \\
H_{55}^{++} &= \epsilon_5, \\
H_{ji}^{++} &= (H_{ij}^{++})^*. \\
H_{16}^{+-} &= 2t_{16}^{10}(\cos k_x + \cos k_y) \\
&\quad + 2t_{16}^{21}[(\cos k_1 + \cos k_2)(\cos k_x + \cos k_y) \\
&\quad - \sin k_1(\sin k_x + \sin k_y) + \sin k_2(\sin k_x - \sin k_y)], \\
H_{17}^{+-} &= 0, \\
H_{18}^{+-} &= 2it_{18}^{10} \sin k_x, \\
H_{19}^{+-} &= 2it_{18}^{10} \sin k_y, \\
H_{1,10}^{+-} &= 0, \\
H_{27}^{+-} &= 2t_{27}^{10}(\cos k_x + \cos k_y),
\end{aligned}$$

$$H_{28}^{+-} = -2it_{29}^{10} \sin k_y,$$

$$H_{29}^{+-} = 2it_{29}^{10} \sin k_x,$$

$$H_{2,10}^{+-} = 2t_{2,10}^{10} (\cos k_x - \cos k_y),$$

$$\begin{aligned} H_{38}^{+-} &= 2t_{38}^{10} \cos k_x + 2t_{49}^{10} \cos k_y \\ &+ 2t_{38}^{21} [(\cos k_1 + \cos k_2) \cos k_x - (\sin k_1 - \sin k_2) \sin k_x] \\ &+ 2t_{49}^{21} [(\cos k_1 + \cos k_2) \cos k_y - (\sin k_1 + \sin k_2) \sin k_y], \end{aligned}$$

$$H_{39}^{+-} = 0,$$

$$H_{3,10}^{+-} = 2it_{4,10}^{10} \sin k_y,$$

$$\begin{aligned} H_{49}^{+-} &= 2t_{49}^{10} \cos k_x + 2t_{38}^{10} \cos k_y \\ &+ 2t_{49}^{21} [(\cos k_1 + \cos k_2) \cos k_x - (\sin k_1 - \sin k_2) \sin k_x] \\ &+ 2t_{38}^{21} [(\cos k_1 + \cos k_2) \cos k_y - (\sin k_1 + \sin k_2) \sin k_y], \end{aligned}$$

$$H_{4,10}^{+-} = 2it_{4,10}^{10} \sin k_x,$$

$$H_{5,10}^{+-} = 0.$$

(B-2)

For the 3D part of the Hamiltonian,

$$\begin{aligned} H_{11}^{++} &= H_{11}^{++} + [2t_{11}^{001} + 4t_{11}^{111} (\cos k_1 + \cos k_2) \\ &+ 4t_{11}^{201} (\cos 2k_x + \cos 2k_y)] \cos k_z, \end{aligned}$$

$$H_{13}^{++} = H_{13}^{++} - 4t_{14}^{201} \sin 2k_y \sin k_z,$$

$$H_{14}^{++} = H_{14}^{++} - 4t_{14}^{201} \sin 2k_x \sin k_z,$$

$$H_{33}^{++} = H_{33}^{++} + [2t_{33}^{001} + 4t_{33}^{201} \cos 2k_x + 4t_{33}^{021} \cos 2k_y] \cos k_z,$$

$$H_{44}^{++} = H_{44}^{++} + [2t_{33}^{001} + 4t_{33}^{021} \cos 2k_x + 4t_{33}^{201} \cos 2k_y] \cos k_z,$$

$$\begin{aligned} H_{16}^{+-} &= H_{16}^{+-} + 4t_{16}^{101} (\cos k_x + \cos k_y) \cos k_z \\ &+ 2t_{16}^{121} \{ [\cos(k_1 + k_y) + \cos(k_1 + k_x)] \exp(ik_z) \\ &+ [\cos(k_2 + k_y) + \cos(k_2 - k_x)] \exp(-ik_z) \}, \end{aligned}$$

$$\begin{aligned}
H_{18}^{+-} &= H_{18}^{+-} + 4it_{18}^{101} \sin k_x \cos k_z - 4t_{19}^{101} \sin k_y \sin k_z \\
&\quad + 2it_{19}^{211} [\sin(k_1 + k_y) \exp(ik_z) - \sin(k_2 + k_y) \exp(-ik_z)], \\
H_{19}^{+-} &= H_{19}^{+-} + 4it_{18}^{101} \sin k_y \cos k_z - 4t_{19}^{101} \sin k_x \sin k_z \\
&\quad + 2it_{19}^{211} [\sin(k_1 + k_x) \exp(ik_z) + \sin(k_2 - k_x) \exp(-ik_z)], \\
H_{38}^{+-} &= H_{38}^{+-} + 4(t_{38}^{101} \cos k_x + t_{49}^{101} \cos k_y) \cos k_z \\
&\quad + 2t_{38}^{121} [\cos(k_1 + k_x) \exp(ik_z) + \cos(k_2 - k_x) \exp(-ik_z)] \\
&\quad + 2t_{49}^{121} [\cos(k_1 + k_y) \exp(ik_z) + \cos(k_2 + k_y) \exp(-ik_z)], \\
H_{39}^{+-} &= H_{39}^{+-} + 4it_{39}^{101} (\cos k_x + \cos k_y) \sin k_z, \\
H_{49}^{+-} &= H_{49}^{+-} + 4(t_{49}^{101} \cos k_x + t_{38}^{101} \cos k_y) \cos k_z \\
&\quad + 2t_{49}^{121} [\cos(k_1 + k_x) \exp(ik_z) + \cos(k_2 - k_x) \exp(-ik_z)] \\
&\quad + 2t_{38}^{121} [\cos(k_1 + k_y) \exp(ik_z) + \cos(k_2 + k_y) \exp(-ik_z)]. \tag{B-3}
\end{aligned}$$

The numerical values for hopping parameters in units of eV are as follows. For the 2D part,

$$\begin{aligned}
\epsilon_1 &= 0.020, \quad \epsilon_2 = -0.2605, \quad \epsilon_3 = -0.0075, \\
\epsilon_5 &= -0.3045, \quad t_{11}^{11} = 0.030, \quad t_{16}^{10} = -0.0185, \\
t_{11}^{20} &= -0.010, \quad t_{16}^{21} = 0.0035, \quad t_{13}^{11} = -0.0635i, \\
t_{18}^{10} &= 0.155i, \quad t_{15}^{11} = -0.090, \quad t_{27}^{10} = -0.2225, \\
t_{22}^{11} &= 0.070, \quad t_{29}^{10} = -0.1925i, \quad t_{23}^{11} = -0.010i, \\
t_{2,10}^{10} &= 0.1615, \quad t_{33}^{11} = 0.152, \quad t_{38}^{10} = 0.050, \\
t_{33}^{20} &= -0.004, \quad t_{38}^{21} = 0.040, \quad t_{33}^{02} = -0.051, \\
t_{49}^{10} &= 0.210, \quad t_{33}^{22} = -0.005, \quad t_{49}^{21} = -0.053, \\
t_{34}^{11} &= 0.090, \quad t_{4,10}^{10} = 0.0995i, \quad t_{35}^{11} = 0.1005i.
\end{aligned}$$

For the 3D part,

$$t_{16}^{101} = -0.004, \quad t_{11}^{001} = 0.0105, \quad t_{11}^{111} = 0,$$

$$t_{11}^{201} = 0, \quad t_{14}^{201} = 0, \quad t_{33}^{001} = -0.003,$$

$$t_{33}^{201} = 0, \quad t_{33}^{021} = 0.0105, \quad t_{16}^{121} = 0,$$

$$t_{18}^{101} = 0, \quad t_{19}^{101} = 0, \quad t_{19}^{211} = 0,$$

$$t_{38}^{101} = 0.0115, \quad t_{38}^{121} = 0, \quad t_{39}^{101} = 0,$$

$$t_{49}^{101} = 0, \quad t_{49}^{121} = 0.$$

Some hopping parameters  $t_{\ell\ell'}^{rst}$  are purely imaginary numbers because the  $d_{xz}$  and  $d_{yz}$  orbitals are multiplied by the imaginary unit factor to get the real Hamiltonian matrix. However, if one were interested in orbital resolved susceptibility or pairing vertex function, real orbitals are more meaningful [77], so we can introduce a gauge transformation to real orbitals by the matrix  $S = \text{diag}(1, 1, i, i, 1, 1, 1, -i, -i, 1)$ , and the transformed Hamiltonian is  $\tilde{H}_0^{\text{ARPES}} = S^{-1} H_0^{\text{ARPES}} S$ .

## REFERENCES

- [1] K. Bennemann and J. Ketterson, in *Superconductivity*, edited by K. Bennemann and J. Ketterson (Springer Berlin Heidelberg, 2008) pp. 3–26.
- [2] C. W. Chu, in *BCS: 50 Years*, edited by L. N. Cooper and D. Feldman (World Scientific, 2010) Chap. 16, pp. 391–438.
- [3] E. Abrahams, in *BCS: 50 Years*, edited by L. N. Cooper and D. Feldman (World Scientific, 2010) Chap. 17, pp. 439–469.
- [4] D. C. Johnston, *Adv. Phys.* **59**, 803 (2010).
- [5] J. Paglione and R. L. Greene, *Nat. Phys.* **6**, 645 (2010).
- [6] G. R. Stewart, *Rev. Mod. Phys.* **83**, 1589 (2011).
- [7] H.-H. Wen and S. Li, *Annu. Rev. Condens. Matter Phys.* **2**, 121 (2011).
- [8] P. J. Hirschfeld, M. M. Korshunov, and I. I. Mazin, *Rep. Prog. Phys.* **74**, 124508 (2011).
- [9] A. Chubukov, *Annu. Rev. Condens. Matter Phys.* **3**, 57 (2012).
- [10] D. J. Scalapino, *Rev. Mod. Phys.* **84**, 1383 (2012).
- [11] D. van Delft and P. Kes, *Phys. Today* **63**, 38 (2010).
- [12] W. Meissner and R. Ochsenfeld, *Naturwissenschaften* **21**, 787 (1933).
- [13] A. Geim, *Phys. Today* **51**, 36 (1998).
- [14] E. H. Brandt, *Am. J. Phys.* **58**, 43 (1990).
- [15] F. London and H. London, *Proc. R. Soc. Lond. A* **149**, 71 (1935).
- [16] A. B. Pippard, *Proc. R. Soc. Lond. A* **216**, 547 (1953).
- [17] C. A. Reynolds, B. Serin, W. H. Wright, and L. B. Nesbitt, *Phys. Rev.* **78**, 487 (1950).
- [18] E. Maxwell, *Phys. Rev.* **78**, 477 (1950).
- [19] V. L. Ginzburg and L. D. Landau, *Zh. Eksp. Teor. Fiz.* **20**, 1064 (1950).
- [20] J. Bardeen, L. N. Cooper, and J. R. Schrieffer, *Phys. Rev.* **108**, 1175 (1957).
- [21] L. P. Gor'kov, *Sov. Phys. JETP* **9**, 1364 (1959).
- [22] L. N. Cooper, *Phys. Rev.* **104**, 1189 (1956).

- [23] A. Abrikosov, L. Gor'kov, and I. Dzyaloshinski, *Methods of Quantum Field Theory in Statistical Physics* (Prentice-Hall, 1963).
- [24] J. R. Schrieffer, *Theory Of Superconductivity* (Westview Press, 1983).
- [25] T. H. Geballe, B. T. Matthias, G. W. Hull, and E. Corenzwit, *Phys. Rev. Lett.* **6**, 275 (1961).
- [26] A. Migdal, *Sov. Phys. JETP* **7**, 996 (1958).
- [27] P. W. Anderson, in *BCS: 50 Years*, edited by L. N. Cooper and D. Feldman (World Scientific, 2010) Chap. 8, pp. 127–142.
- [28] W. L. McMillan, *Phys. Rev.* **167**, 331 (1968).
- [29] M. L. Cohen and P. W. Anderson, *AIP Conf. Proc.* **4**, 17 (1972).
- [30] P. B. Allen and R. C. Dynes, *Phys. Rev. B* **12**, 905 (1975).
- [31] J. Nagamatsu, *et al.*, *Nature* **410**, 63 (2001).
- [32] S. L. Bud'ko, *et al.*, *Phys. Rev. Lett.* **86**, 1877 (2001).
- [33] D. D. Osheroff, R. C. Richardson, and D. M. Lee, *Phys. Rev. Lett.* **28**, 885 (1972).
- [34] D. Vollhardt and P. Wölfle, *The Superfluid Phases of Helium 3* (Taylor & Francis, 1990).
- [35] D. Lee and A. Leggett, *J. Low Temp. Phys.* **164**, 140 (2011).
- [36] F. Steglich, *et al.*, *Phys. Rev. Lett.* **43**, 1892 (1979).
- [37] C. Pfleiderer, *Rev. Mod. Phys.* **81**, 1551 (2009).
- [38] Y. Kamihara, *et al.*, *J. Am. Chem. Soc.* **128**, 10012 (2006).
- [39] Y. Kamihara, T. Watanabe, M. Hirano, and H. Hosono, *J. Am. Chem. Soc.* **130**, 3296 (2008).
- [40] I. I. Mazin, *Nature* **464**, 183 (2010).
- [41] P. W. Anderson, *Science* **235**, 1196 (1987).
- [42] J. Hubbard, *Proc. R. Soc. Lond. A* **276**, 238 (1963).
- [43] E. Dagotto, *Rev. Mod. Phys.* **66**, 763 (1994).
- [44] S. Raghu, S. A. Kivelson, and D. J. Scalapino, *Phys. Rev. B* **81**, 224505 (2010).
- [45] C. C. Tsuei, *et al.*, *Phys. Rev. Lett.* **73**, 593 (1994).

- [46] I. I. Mazin, D. J. Singh, M. D. Johannes, and M. H. Du, Phys. Rev. Lett. **101**, 057003 (2008).
- [47] D. Scalapino, Phys. Rep. **250**, 329 (1995).
- [48] H. Kontani and S. Onari, Phys. Rev. Lett. **104**, 157001 (2010).
- [49] M. Sigrist and K. Ueda, Rev. Mod. Phys. **63**, 239 (1991).
- [50] V. Cvetkovic and O. Vafek, Phys. Rev. B **88**, 134510 (2013).
- [51] J. Hu, Phys. Rev. X **3**, 031004 (2013).
- [52] M. D. Lumsden, *et al.*, Phys. Rev. Lett. **102**, 107005 (2009).
- [53] A. D. Christianson, *et al.*, Phys. Rev. Lett. **103**, 087002 (2009).
- [54] D. Inosov, *et al.*, Nat. Phys. **6**, 178 (2010).
- [55] J. T. Park, *et al.*, Phys. Rev. B **82**, 134503 (2010).
- [56] D. N. Argyriou, *et al.*, Phys. Rev. B **81**, 220503 (2010).
- [57] J.-P. Castellan, *et al.*, Phys. Rev. Lett. **107**, 177003 (2011).
- [58] T. Hanaguri, S. Niitaka, K. Kuroki, and H. Takagi, Science **328**, 474 (2010).
- [59] C.-T. Chen, *et al.*, Nat. Phys. **6**, 260 (2010).
- [60] P. Choubey, *et al.*, arXiv:1401.7732 (2014).
- [61] G. Eilenberger, Zeitschrift für Physik **214**, 195 (1968).
- [62] A. I. Larkin and Y. N. Ovchinnikov, Sov. Phys. JETP **28**, 1200 (1969).
- [63] J. Serene and D. Rainer, Phys. Rep. **101**, 221 (1983).
- [64] G. Volovik, JETP Lett. **58**, 469 (1993).
- [65] K. A. Moler, *et al.*, Phys. Rev. B **55**, 3954 (1997).
- [66] Y. Wang, B. Revaz, A. Erb, and A. Junod, Phys. Rev. B **63**, 094508 (2001).
- [67] M. Ichioka, N. Hayashi, N. Enomoto, and K. Machida, Phys. Rev. B **53**, 15316 (1996).
- [68] N. Schopohl and K. Maki, Phys. Rev. B **52**, 490 (1995).
- [69] M. Ichioka, N. Hayashi, and K. Machida, Phys. Rev. B **55**, 6565 (1997).
- [70] M. Ichioka, A. Hasegawa, and K. Machida, Phys. Rev. B **59**, 184 (1999).
- [71] M. Franz and Z. Tešanović, Phys. Rev. Lett. **84**, 554 (2000).

- [72] I. Vekhter and A. Vorontsov, *Physica B: Condensed Matter* **403**, 958 (2008).
- [73] Y. Bang, *Phys. Rev. Lett.* **104**, 217001 (2010).
- [74] T. Dahm, S. Graser, C. Iniotakis, and N. Schopohl, *Phys. Rev. B* **66**, 144515 (2002).
- [75] N. Schopohl, cond-mat/9804064 (unpublished)(1998).
- [76] F.-C. Hsu, *et al.*, *Proc. Natl. Acad. Sci.* **105**, 14262 (2008).
- [77] A. F. Kemper, *et al.*, *New J. Phys.* **12**, 073030 (2010).
- [78] S. Kasahara, *et al.*, *Phys. Rev. B* **81**, 184519 (2010).
- [79] S. Jiang, *et al.*, *J. Phys.: Condens. Matter* **21**, 382203 (2009).
- [80] H. Shishido, *et al.*, *Phys. Rev. Lett.* **104**, 057008 (2010).
- [81] K. Hashimoto, *et al.*, *Phys. Rev. B* **81**, 220501 (2010).
- [82] Y. Nakai, *et al.*, *Phys. Rev. B* **81**, 020503 (2010).
- [83] M. Yamashita, *et al.*, *Phys. Rev. B* **84**, 060507 (2011).
- [84] J. S. Kim, *et al.*, *Phys. Rev. B* **81**, 214507 (2010).
- [85] Y. Wang, *et al.*, *Phys. Rev. B* **84**, 184524 (2011).
- [86] J. S. Kim, *et al.*, *Phys. Rev. B* **86**, 014513 (2012).
- [87] V. G. Kogan and J. Schmalian, *Phys. Rev. B* **83**, 054515 (2011).
- [88] J. S. Kim, E. G. Kim, and G. R. Stewart, *J. Phys.: Condens. Matter* **21**, 252201 (2009).
- [89] K. Suzuki, H. Usui, and K. Kuroki, *J. Phys. Soc. Jpn.* **80**, 013710 (2011).
- [90] T. Shimojima, *et al.*, *Science* **332**, 564 (2011).
- [91] V. Mishra, *et al.*, *Phys. Rev. B* **79**, 094512 (2009).
- [92] V. Mishra, S. Graser, and P. J. Hirschfeld, *Phys. Rev. B* **84**, 014524 (2011).
- [93] T. Yoshida, *et al.*, *Phys. Rev. Lett.* **106**, 117001 (2011).
- [94] L. Kramer and W. Pesch, *Zeitschrift für Physik* **269**, 59 (1974).
- [95] W. Pesch and L. Kramer, *J. Low Temp. Phys.* **15**, 367 (1974).
- [96] U. Brandt, W. Pesch, and L. Tewordt, *Zeitschrift für Physik* **201**, 209 (1967).
- [97] W. Pesch, *Z. Phys. B* **21**, 263 (1975).

- [98] M. Zhitomirsky and V.-H. Dao, Phys. Rev. B **69**, 054508 (2004).
- [99] P. Klimesch and W. Pesch, J. Low Temp. Phys. **32**, 869 (1978).
- [100] Y. Matsuda, K. Izawa, and I. Vekhter, J. Phys.: Condens. Matter **18**, R705 (2006).
- [101] S. Graser, *et al.*, Phys. Rev. B **77**, 180514 (2008).
- [102] B. Zeng, *et al.*, Nat. Commun. **1**, 112 (2010).
- [103] A. B. Vorontsov and I. Vekhter, Phys. Rev. Lett. **105**, 187004 (2010).
- [104] A. V. Chubukov and I. Eremin, Phys. Rev. B **82**, 060504 (2010).
- [105] J. M. Byers, M. E. Flatté, and D. J. Scalapino, Phys. Rev. Lett. **71**, 3363 (1993).
- [106] A. V. Balatsky, I. Vekhter, and J.-X. Zhu, Rev. Mod. Phys. **78**, 373 (2006).
- [107] M. Franz and Z. Tešanović, Phys. Rev. Lett. **80**, 4763 (1998).
- [108] I. Maggio-Aprile, *et al.*, Phys. Rev. Lett. **75**, 2754 (1995).
- [109] G. Levy, *et al.*, Phys. Rev. Lett. **95**, 257005 (2005).
- [110] Ø. Fischer, *et al.*, Rev. Mod. Phys. **79**, 353 (2007).
- [111] J.-X. Zhu and C. S. Ting, Phys. Rev. Lett. **87**, 147002 (2001).
- [112] H. F. Hess, R. B. Robinson, and J. V. Waszczak, Phys. Rev. Lett. **64**, 2711 (1990).
- [113] N. Hayashi, M. Ichioka, and K. Machida, Phys. Rev. Lett. **77**, 4074 (1996).
- [114] X. Hu, C. S. Ting, and J.-X. Zhu, Phys. Rev. B **80**, 014523 (2009).
- [115] D. Wang, J. Xu, Y.-Y. Xiang, and Q.-H. Wang, Phys. Rev. B **82**, 184519 (2010).
- [116] Y. Yin, *et al.*, Phys. Rev. Lett. **102**, 097002 (2009).
- [117] L. Shan, *et al.*, Nat. Phys. **7**, 325 (2011).
- [118] D. J. Singh, Phys. Rev. B **78**, 094511 (2008).
- [119] S. V. Borisenko, *et al.*, Phys. Rev. Lett. **105**, 067002 (2010).
- [120] C. Putzke, *et al.*, Phys. Rev. Lett. **108**, 047002 (2012).
- [121] H. Kim, *et al.*, Phys. Rev. B **83**, 100502 (2011).
- [122] F. Wei, *et al.*, Phys. Rev. B **81**, 134527 (2010).
- [123] S. V. Borisenko, *et al.*, Symmetry **4**, 251 (2012).
- [124] K. Umezawa, *et al.*, Phys. Rev. Lett. **108**, 037002 (2012).

- [125] Y. Wang, *et al.*, Phys. Rev. B **88**, 174516 (2013).
- [126] M. P. Allan, *et al.*, Science **336**, 563 (2012).
- [127] T. Hanaguri, *et al.*, Phys. Rev. B **85**, 214505 (2012).
- [128] P. Giannozzi, *et al.*, J. Phys.: Condens. Matter **21**, 395502 (2009).
- [129] S. Graser, *et al.*, Phys. Rev. B **81**, 214503 (2010).
- [130] S. Maiti, *et al.*, Phys. Rev. Lett. **107**, 147002 (2011).
- [131] S. Graser, T. A. Maier, P. J. Hirschfeld, and D. J. Scalapino, New J. Phys. **11**, 025016 (2009).
- [132] Y. Senga and H. Kontani, J. Phys. Soc. Jpn. **77**, 113710 (2008).
- [133] Y. Senga and H. Kontani, New J. Phys. **11**, 035005 (2009).
- [134] S. Onari and H. Kontani, Phys. Rev. Lett. **103**, 177001 (2009).
- [135] J. Li, *et al.*, Phys. Rev. B **85**, 214509 (2012).
- [136] K. Kirshenbaum, *et al.*, Phys. Rev. B **86**, 140505 (2012).
- [137] Y. Li, *et al.*, New J. Phys. **12**, 083008 (2010).
- [138] Y. Nakajima, *et al.*, Phys. Rev. B **82**, 220504 (2010).
- [139] M. Tropeano, *et al.*, Phys. Rev. B **81**, 184504 (2010).
- [140] P. Anderson, J. Phys. Chem. Solids **11**, 26 (1959).
- [141] A. Abrikosov and L. Gor'kov, Sov. Phys. JETP **12**, 1243 (1961).
- [142] G. Preosti and P. Muzikar, Phys. Rev. B **54**, 3489 (1996).
- [143] A. A. Golubov and I. I. Mazin, Phys. Rev. B **55**, 15146 (1997).
- [144] A. Golubov and I. Mazin, Physica C: Superconductivity **243**, 153 (1995).
- [145] D. Parker, *et al.*, Phys. Rev. B **78**, 134524 (2008).
- [146] A. V. Chubukov, D. V. Efremov, and I. Eremin, Phys. Rev. B **78**, 134512 (2008).
- [147] Y. Bang, H.-Y. Choi, and H. Won, Phys. Rev. B **79**, 054529 (2009).
- [148] A. A. Golubov, *et al.*, Phys. Rev. B **66**, 054524 (2002).
- [149] V. G. Kogan, C. Martin, and R. Prozorov, Phys. Rev. B **80**, 014507 (2009).
- [150] M. L. Kulić and O. V. Dolgov, Phys. Rev. B **60**, 13062 (1999).

- [151] Y. Ohashi, *Physica C: Superconductivity* **412–414, Part 1**, 41 (2004).
- [152] D. V. Efremov, *et al.*, *Phys. Rev. B* **84**, 180512 (2011).
- [153] A. F. Kemper, C. Cao, P. J. Hirschfeld, and H.-P. Cheng, *Phys. Rev. B* **80**, 104511 (2009).
- [154] A. F. Kemper, C. Cao, P. J. Hirschfeld, and H.-P. Cheng, *Phys. Rev. B* **81**, 229902 (2010).
- [155] K. Nakamura, R. Arita, and H. Ikeda, *Phys. Rev. B* **83**, 144512 (2011).
- [156] S. Graser, P. J. Hirschfeld, L.-Y. Zhu, and T. Dahm, *Phys. Rev. B* **76**, 054516 (2007).
- [157] L. Zhu, P. J. Hirschfeld, and D. J. Scalapino, *Phys. Rev. B* **70**, 214503 (2004).
- [158] D. V. Evtushinsky, *et al.*, *New J. Phys.* **11**, 055069 (2009).
- [159] H. Ding, *et al.*, *J. Phys.: Condens. Matter* **23**, 135701 (2011).
- [160] V. Brouet, *et al.*, *Phys. Rev. B* **80**, 165115 (2009).
- [161] F. Gross, *et al.*, *Z. Phys. B* **64**, 175 (1986).
- [162] L. Gor'kov and P. Kalugin, *JETP Lett.* **41**, 253 (1985).
- [163] K. Ueda and T. Rice, in *Theory of Heavy Fermions and Valence Fluctuations*, Springer Series in Solid-State Sciences, Vol. 62, edited by T. Kasuya and T. Saso (Springer Berlin Heidelberg, 1985) pp. 267–276.
- [164] P. J. Hirschfeld and N. Goldenfeld, *Phys. Rev. B* **48**, 4219 (1993).
- [165] L. S. Borkowski and P. J. Hirschfeld, *Phys. Rev. B* **49**, 15404 (1994).
- [166] A. Lankau, *et al.*, *Phys. Rev. B* **82**, 184518 (2010).
- [167] T. Hajiri, *et al.*, *Phys. Rev. B* **85**, 094509 (2012).
- [168] I. A. Nekrasov, Z. V. Pchelkina, and M. V. Sadovskii, *JETP Lett.* **88**, 543 (2008).
- [169] Z. P. Yin, K. Haule, and G. Kotliar, *Nat. Mater.* **10**, 932 (2011).
- [170] J. Ferber, K. Foyevtsova, R. Valentí, and H. O. Jeschke, *Phys. Rev. B* **85**, 094505 (2012).
- [171] G. Lee, *et al.*, *Phys. Rev. Lett.* **109**, 177001 (2012).
- [172] B. Zeng, *et al.*, *Phys. Rev. B* **88**, 144518 (2013).
- [173] Z. Li, *et al.*, *J. Phys. Soc. Jpn.* **79**, 083702 (2010).

- [174] S.-H. Baek, *et al.*, Eur. Phys. J. B **85**, 1 (2012).
- [175] P. M. R. Brydon, M. Daghofer, C. Timm, and J. van den Brink, Phys. Rev. B **83**, 060501 (2011).
- [176] A. E. Taylor, *et al.*, Phys. Rev. B **83**, 220514 (2011).
- [177] D. K. Morr, P. F. Trautman, and M. J. Graf, Phys. Rev. Lett. **86**, 5978 (2001).
- [178] M. A. Tanatar, *et al.*, Phys. Rev. B **84**, 054507 (2011).
- [179] K. Hashimoto, *et al.*, Phys. Rev. Lett. **108**, 047003 (2012).
- [180] K. Okazaki, *et al.*, Science **337**, 1314 (2012).
- [181] K. Okazaki, *et al.*, Phys. Rev. Lett. **109**, 237011 (2012).
- [182] Y. Wang, P. J. Hirschfeld, and I. Vekhter, Phys. Rev. B **85**, 020506 (2012).
- [183] H. Eschrig and K. Koepf, Phys. Rev. B **80**, 104503 (2009).
- [184] C. Platt, R. Thomale, and W. Hanke, Phys. Rev. B **84**, 235121 (2011).
- [185] K. Kuroki, *et al.*, Phys. Rev. Lett. **101**, 087004 (2008).
- [186] T. Takimoto, T. Hotta, and K. Ueda, Phys. Rev. B **69**, 104504 (2004).
- [187] G. W. Crabtree, *et al.*, Phys. Rev. B **35**, 1728 (1987).
- [188] T. A. Maier, S. Graser, D. J. Scalapino, and P. J. Hirschfeld, Phys. Rev. B **79**, 224510 (2009).
- [189] S. Maiti, M. M. Korshunov, and A. V. Chubukov, Phys. Rev. B **85**, 014511 (2012).
- [190] A. Kreisel, *et al.*, Phys. Rev. B **88**, 094522 (2013).
- [191] E. Dagotto, Rev. Mod. Phys. **85**, 849 (2013).
- [192] T. Qian, *et al.*, Phys. Rev. Lett. **106**, 187001 (2011).
- [193] M. Xu, *et al.*, Phys. Rev. B **85**, 220504 (2012).
- [194] T. A. Maier, S. Graser, P. J. Hirschfeld, and D. J. Scalapino, Phys. Rev. B **83**, 100515 (2011).
- [195] F. Wang, *et al.*, Europhys. Lett. **93**, 57003 (2011).
- [196] I. I. Mazin, Phys. Rev. B **84**, 024529 (2011).
- [197] M. Khodas and A. V. Chubukov, Phys. Rev. Lett. **108**, 247003 (2012).
- [198] T. Saito, S. Onari, and H. Kontani, Phys. Rev. B **83**, 140512 (2011).

- [199] Q.-Y. Wang, *et al.*, Chin. Phys. Lett. **29**, 037402 (2012).
- [200] D. Liu, *et al.*, Nat. Commun. **3**, 931 (2012).
- [201] S. He, *et al.*, Nat. Mater. **12**, 605 (2013).
- [202] S. Tan, *et al.*, Nat. Mater. **12**, 634 (2013).
- [203] W.-H. Zhang, *et al.*, Chin. Phys. Lett. **31**, 017401 (2014).
- [204] R. Peng, *et al.*, arXiv:1310.3060 (2013).
- [205] R. Peng, *et al.*, arXiv:1402.1357 (2014).
- [206] J. He, *et al.*, arXiv:1401.7115 (2014).
- [207] J. H. Tapp, *et al.*, Phys. Rev. B **78**, 060505 (2008).

## BIOGRAPHICAL SKETCH

Yan Wang was born in Jiangsu, China in 1985. He obtained his Bachelor of Science degree in physics from Fudan University in Shanghai, China in 2008. In the same year, he enrolled in the graduate school at University of Florida, Gainesville, United States. He received his Doctor of Philosophy degree in physics in the spring of 2014. He has experienced and enjoyed the cultural clash and harmony while pursuing the rigorous knowledge in science. He values the years of study and doctoral research training most as an education in methodology of conducting scientific research.